# Plate Motions

# 2

**Abstract**

Plate kinematics represents a fundamental sub-discipline of plate tectonics. In this chapter, I describe the geometry of plate motions independently from the geodynamic factors (forces, torques, stresses) that drive the movement or changes in the state of motion of a tectonic plate. At this stage, the focus is on modelling, in particular on plate reconstructions, thereby the general description proceeds assuming that kinematic data are already available.

## 2.1 The Continuum Mechanics Representation

Earth's crust and mantle are deformable solids, composed by a large number of closely spaced microscopic mineral grains of arbitrary shape and size. At macroscopic scale, a rigorous quantitative description of the geodynamic evolution of a rock system starts from the introduction of infinitesimal quantities, the *volume elements* $dV$, which represent the smallest chemically and physically homogeneous parts in which a rock assemblage can be divided. It is usually assumed that a volume element fills a continuous region of the three-dimensional space, namely a closed subset $\mathbf{R} \subset \Re^3$, and has regular shape, for example a parallelepiped $dV = dxdydz$. In practice, the computational techniques employed in plate tectonics often require a definition of volume elements having dimensions up to several km, depending on the scale of the problem, yet being small in relation to the total volume of the rock system.

In the continuum mechanics representation of solid Earth systems, any geophysical entity (for example, a subducting slab) is formed by a continuous distribution of small volume elements, $dV$, whose locations are described by position vectors $\boldsymbol{r}$ in the selected reference frame. In this representation, the *intensive variables* (also known as *bulk properties*) are quantities describing *local* physical properties of the volume elements, for example their temperature, velocity, etc. It is assumed that these quantities vary smoothly across the region $\mathbf{R}$, so that they can be represented mathematically by continuous functions of position vectors $\boldsymbol{r} \in \mathbf{R}$. Often the intensive variables are associated with scalar fields (see Appendix 1), $\phi = \phi(\boldsymbol{r})$, having appropriate continuity properties. Typical examples are the local temperature, $T = T(\boldsymbol{r})$, and pressure, $p = p(\boldsymbol{r})$, of rocks. However, not all of the intensive variables can be represented by scalar fields. For instance, the displacement of a point $\boldsymbol{r}$ during deformation must be described by a vector quantity, $\boldsymbol{u} = \boldsymbol{u}(\boldsymbol{r})$, which varies from point to point in $\mathbf{R}$. Therefore, intensive variables

A. Schettino, *Quantitative Plate Tectonics*, DOI 10.1007/978-3-319-09135-8_2,

are sometimes associated with vector or even tensor fields (see Appendix 1).

The continuum mechanics representation of Earth systems also includes *extensive variables*. These quantities are *global* physical properties, which depend from the total volume $V$ of a system through integral expressions involving *density* functions. A classic example is the total mass of a rock body. Let $dV$ be a volume element centered at position $\boldsymbol{r}$ in the region $\mathbf{R}$. The approach of continuum mechanics is to consider the mass contained in $dV$ as the analog of a point mass, so that the classic equations of elementary physics can be easily generalized to the new framework. To this purpose, we can introduce a new intensive quantity, the *density of mass*, $\rho = \rho(\boldsymbol{r})$, such that the infinitesimal mass contained in the volume $dV$ will be given by: $dm = \rho(\boldsymbol{r})dV$. In this instance, the total mass of a body is an extensive property that can be computed by evaluating the following integral expression:

$$M = \int_{\mathbf{R}} \rho\,(\boldsymbol{r})\, dV \tag{2.1}$$

Similar expressions can be written for the total electric charge, magnetization, etc. introducing appropriate density functions. If a continuous rock system is subject to an external action-at-a-distance force field, such as a gravity or magnetic field, this force operates on each volume element in $\mathbf{R}$. Therefore, we can introduce a *body force density* (force per unit volume), $\boldsymbol{f} = \boldsymbol{f}(\boldsymbol{r})$, such that the infinitesimal force exerted on a volume element $dV$ will be given by: $d\boldsymbol{F} = \boldsymbol{f}(\boldsymbol{r})dV$. Using this definition, the total force, $\boldsymbol{F}$, and the torque, $\boldsymbol{N}$, exerted on the whole body are extensive variables given respectively by:

$$\boldsymbol{F} = \int_{\mathbf{R}} \boldsymbol{f}\,(\boldsymbol{r})\, dV \tag{2.2}$$

$$\boldsymbol{N} = \int_{\mathbf{R}} \boldsymbol{r} \times \boldsymbol{f}\,(\boldsymbol{r})\, dV \tag{2.3}$$

An important kinematic parameter of a point mass distribution is the *center of mass*, which is a position vector representing the location of the entire system. In elementary mechanics, this vector is obtained by taking the weighted average of the individual position vectors, and using the mass of each particle as a weighting parameter. The continuum mechanics analogue of this quantity is another extensive variable, which can be calculated by substituting the sum appearing in the elementary definition by an integral expression.

Therefore, the center of mass of a continuous distribution is defined as follows:

$$\boldsymbol{R} = \frac{1}{M} \int_{\mathbf{R}} \rho\,(\boldsymbol{r})\, \boldsymbol{r}\, dV \tag{2.4}$$

where $M$ is the total mass. The last extensive variable considered here is the *angular momentum* of the system, which measures the rotational component of motion with respect to an arbitrary reference point. This quantity is usually calculated with respect to the origin of the reference frame or, alternatively, with respect to the center of mass depending on the problem under consideration. In the former case, the angular momentum is given by the following integral expression, which is an obvious extension of the elementary definition:

$$\boldsymbol{L} = \int_{\mathbf{R}} \boldsymbol{r} \times \rho\,(\boldsymbol{r})\, \boldsymbol{v}\,(\boldsymbol{r})\, dV \tag{2.5}$$

In this expression, the vector field $\boldsymbol{v} = \boldsymbol{v}(\boldsymbol{r})$ represents the velocity of the mass element at position $\boldsymbol{r}$. In the next section, we shall consider a special form of expression (2.5), which is particularly useful in plate kinematics, where mass distributions represent rigid tectonic plates.

## 2.2 Euler's Theorem and Rigid Rotations

Plate dynamics and kinematics, in short plate tectonics, cannot be described using a unique mathematical apparatus and a single physical theory, because the various interacting subsystems of the solid Earth (plates, slabs, asthenosphere, etc.) conform to different physical laws, depending on the time scale of observation (seconds, years,

thousands or million years). Even when considered at a common temporal scale, these subsystems display distinct mechanical behaviors. For example, the motion of tectonic plates during the geological time (intervals of Myrs) can be described in terms of rigid body's kinematics, whereas the asthenosphere behaves as a fluid at the same temporal scale. However, both can be considered as elastic bodies if we are studying earthquakes and propagation of seismic waves in the solid Earth. In summary, the sole unifying framework of plate tectonics is the continuum mechanics representation illustrated in the previous section, while both the kinematic description of the processes and the geodynamic laws that link forces to kinematics will be different depending on the subsystem and the temporal scale of observation.

Observation suggests that tectonic plates can be considered as *rigid* bodies at first approximation. Consequently, the volume elements that fill a region $\mathbf{R} \subset \Re^3$, representative of a tectonic plate, are also rigid entities, and the distance between any pair of volume elements in $\mathbf{R}$ is an invariant. This is equivalent to say that the electromagnetic interaction between adjacent volume elements is so strong that any external force is overcome, so that deformation is negligible. In this instance, an important theorem, due to Leonhard Euler (1775), can be used as a starting point for the mathematical description of plate kinematics. The statement of Euler's theorem is very simple:

**Euler's Theorem**
*If a sphere S is moved about its center, O, it is always possible to find a diameter, D, of fixed points.*

*Proof* Let $\boldsymbol{r}_1$, $\boldsymbol{r}_2$, $\boldsymbol{r}_3$ be three position vectors pointing to arbitrary points, $P_1$, $P_2$, and $P_3$ in the original sphere. After an arbitrary change of orientation of the sphere about its center, these points are moved to new locations, say: $P_1^{'}$, $P_2^{'}$, and $P_3^{'}$, represented by the position vectors: $\boldsymbol{r}_1^{'}$, $\boldsymbol{r}_2^{'}$, $\boldsymbol{r}_3^{'}$. Let $\boldsymbol{T}$ and $\boldsymbol{T}'$ be the $3 \times 3$ matrices formed with the components of these vectors:

$$\boldsymbol{T} = \begin{bmatrix} x_1 & x_2 & x_3 \\ y_1 & y_2 & y_3 \\ z_1 & z_2 & z_3 \end{bmatrix}; \boldsymbol{T'} = \begin{bmatrix} x_1' & x_2' & x_3' \\ y_1' & y_2' & y_3' \\ z_1' & z_2' & z_3' \end{bmatrix}$$

Now let us define a new $3 \times 3$ matrix:

$$\boldsymbol{A} = \boldsymbol{T'}\boldsymbol{T}^{-1} \tag{2.6}$$

The matrix $\boldsymbol{A}$ has the property to transform the original matrix $\boldsymbol{T}$ into the new matrix $\boldsymbol{T}'$:

$$\boldsymbol{A}\,\boldsymbol{T} = \boldsymbol{T'} \tag{2.7}$$

This equation implies, in turn, that $\boldsymbol{A}$ transforms each vector $\boldsymbol{r}_i$ into the corresponding rotated vector $\boldsymbol{r}_i^{'}$:

$$\boldsymbol{A}\,\boldsymbol{r}_i = \boldsymbol{r}_i' \tag{2.8}$$

In general, for any position vector, $\boldsymbol{r}$, the transformation $\boldsymbol{A}$ preserves the distance of the transformed point from the origin, because the sphere is assumed to be rigid:

$$\|\boldsymbol{A}\,\boldsymbol{r}\| = \|\boldsymbol{r}\| \tag{2.9}$$

Squaring this equation gives:

$$\boldsymbol{r}^{\boldsymbol{T}}\boldsymbol{A}^{T}\boldsymbol{A}\boldsymbol{r} = \boldsymbol{r}^{\boldsymbol{T}}\boldsymbol{r} \tag{2.10}$$

thereby $\boldsymbol{A}^T\boldsymbol{A} = \boldsymbol{I}$, where $\boldsymbol{I}$ is the $3 \times 3$ identity matrix, and $\boldsymbol{A}$ is orthogonal. Now let us take the determinant of $\boldsymbol{A}^T\boldsymbol{A}$. It results:

$$\det\left(\boldsymbol{A}^{\boldsymbol{T}}\boldsymbol{A}\right) = [\det(\boldsymbol{A})]^2 = 1 \tag{2.11}$$

Therefore, $\det(\boldsymbol{A}) = \pm 1$. If we consider a null rotation of the sphere from its initial position, then $\boldsymbol{A} = \boldsymbol{I}$ and $\det(\boldsymbol{A}) = \det(\boldsymbol{I}) = +1$. By continuity, any subsequent infinitesimal rotation or sequence of rotations must give $\det(\boldsymbol{A}) = +1$. Furthermore, by the orthogonality of $\boldsymbol{A}$ we have:

$$\boldsymbol{A}^{\boldsymbol{T}}\boldsymbol{A} - \boldsymbol{A} = \left(\boldsymbol{A}^{\boldsymbol{T}} - \boldsymbol{I}\right)\boldsymbol{A} = \boldsymbol{I} - \boldsymbol{A} \tag{2.12}$$

$$\det\left(\boldsymbol{A}^{\boldsymbol{T}} - \boldsymbol{I}\right) = \det\left((\boldsymbol{A} - \boldsymbol{I})^{T}\right) = \det(\boldsymbol{A} - \boldsymbol{I}) \tag{2.13}$$

Therefore, taking the determinant of Eq. (2.12) gives:

$$\det\left(\left(\boldsymbol{A}^T-\boldsymbol{I}\right)\boldsymbol{A}\right)=\det\left(\boldsymbol{A}^T-\boldsymbol{I}\right)\det\left(\boldsymbol{A}\right)$$
$$=\det\left(\boldsymbol{A}^T-\boldsymbol{I}\right)=\det\left(\boldsymbol{A}-\boldsymbol{I}\right)=\det\left(\boldsymbol{I}-\boldsymbol{A}\right) \tag{2.14}$$

Now we take into account that for any $3\times 3$ matrix $\boldsymbol{R}$: $\det(-\boldsymbol{R})=(-1)^3\boldsymbol{R}=-\boldsymbol{R}$. In the case of Eq. (2.14), it results:

$$\det\left(\boldsymbol{A}-\boldsymbol{I}\right)=\det\left(\boldsymbol{I}-\boldsymbol{A}\right)=-\det\left(\boldsymbol{A}-\boldsymbol{I}\right)$$
$$\Longleftrightarrow\quad \det\left(\boldsymbol{A}-\boldsymbol{I}\right)=0 \tag{2.15}$$

Therefore, a vector $\boldsymbol{n}\neq\boldsymbol{0}$ exists such that:

$$\left(\boldsymbol{A}-\boldsymbol{I}\right)\boldsymbol{n}=0 \tag{2.16}$$

Equation (2.16) is a particular eigenvalue equation, where $\boldsymbol{A}$ has eigenvalue $\lambda=+1$ and $\boldsymbol{n}$ is the corresponding eigenvector. This means that $\boldsymbol{n}$ is invariant under transformation $\boldsymbol{A}$. Therefore, a diameter aligned with the direction of $\boldsymbol{n}$ will remain unchanged after the transformation. This proves Euler's theorem. ■

The importance of Euler's theorem for the mathematical formulation of plate kinematics is not immediately evident, despite almost all books and articles about this subject emphasize its fundamental role. If we assume a spherical Earth, tectonic plates can be considered as rigid *spherical caps*, which are constrained to move about its centre. Their instantaneous motion is always represented by an infinitesimal rotation about an axis, as illustrated in Fig. 2.1, and this statement holds independently from Euler's theorem, despite it could be inferred from it. In these rotations, an arbitrary point $P$ lying on a tectonic plate, **R**, is moved along a *small circle arc* about the rotation axis with a velocity $\boldsymbol{v}$ whose magnitude depends from the distance of $P$ from the axis. However, the rigidity of **R** ensures that different points will travel the same *angular* distance $d\alpha$ in a small time interval $dt$, so that a unique angular velocity $\omega=d\alpha/dt$, which is independent from the point, characterizes the instantaneous

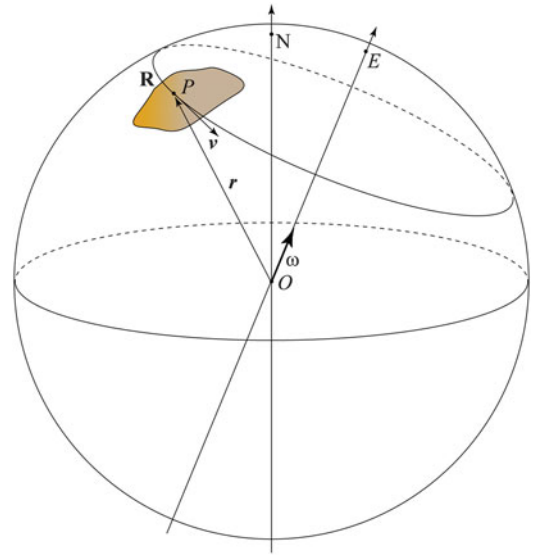


**Fig. 2.1** Geometry of the instantaneous motion of a tectonic plate **R**. $E$ is the Euler pole, $N$ is the North Pole. $P$ is a representative point on **R**, whose instantaneous linear velocity is $\boldsymbol{v}$. $\boldsymbol{\omega}$ is the Euler vector of **R**

rotation. We can easily build a vector, which contains all the information associated with an instantaneous rotation. Such a vector is called an *Euler vector* and has magnitude $\omega$ and direction coinciding with the direction of the rotation axis (Fig. 2.1). In order to assign a unique versor, $\boldsymbol{n}$, to an Euler vector, we conform to the common practice of assuming that all rotations are counterclockwise rotations.

In this instance, the linear velocity of a point $P$ can be calculated by the following formula:

$$\boldsymbol{v}=\boldsymbol{\omega}\times\boldsymbol{r} \tag{2.17}$$

where $\boldsymbol{\omega}=\omega\boldsymbol{n}$ is the Euler vector of the instantaneous rotation. In general, the motion of a tectonic plate proceeds through a sequence of infinitesimal rotations about continuously changing Euler axes. Thus, in principle, reconstructing its position at a given time in the geologic past would require a backtracking procedure, based upon a complete knowledge of the sequence of instantaneous rotations. However, the standard approach adopted in plate kinematic modelling

follows an opposite pathway, which starts from a specification of the orientations of tectonic plates at some ages in the geologic past, *before* any determination of the sequence of instantaneous rotations that carried them to the present day location. The reason is that in most cases the only information available in advance, through the analysis of magnetic or structural data, is represented by the relative positions of the tectonic plates at some ages in the geologic past. These relative positions link the orientation of a tectonic plate at any time $t$ directly to its present day position, regardless of the specific trajectory followed by the plate. The importance of Euler's theorem is just to ensure the existence of a unique invariant axis associated with such transformation from the present day position to the orientation at any time $t$. This means that we can always find a rotation axis $\boldsymbol{n}$ and a *finite* angular displacement, $\Omega$, such that a present day tectonic plate can be moved to the location that it occupied at time $t$, even before knowing the details of the complex sequence of instantaneous rotations that link the past position to the present day location.

Euler's theorem implies that rotations can be composed to furnish other rotations. Therefore, two transformation matrices $\boldsymbol{A}$ and $\boldsymbol{B}$ can be multiplied to give a new rotation matrix $\boldsymbol{C} = \boldsymbol{AB}$ and this operation is not commutative ($\boldsymbol{AB} \neq \boldsymbol{BA}$). The set of all transformation matrices associated with the rigid rotations of a sphere forms a group known as the SO(3) group (special orthogonal group in $\Re^3$). It can be shown that the orthogonal matrix associated with a finite rotation by an angle $\Omega$ about an axis represented by the unit vector $\boldsymbol{n}$, is given by:

$$\boldsymbol{R}(\boldsymbol{n}, \Omega) = \begin{bmatrix} n_x^2(1-\cos\Omega)+\cos\Omega & n_x n_y(1-\cos\Omega)-n_z\sin\Omega & n_x n_z(1-\cos\Omega)+n_y\sin\Omega \\ n_x n_y(1-\cos\Omega)+n_z\sin\Omega & n_y^2(1-\cos\Omega)+\cos\Omega & n_y n_z(1-\cos\Omega)-n_x\sin\Omega \\ n_x n_z(1-\cos\Omega)-n_y\sin\Omega & n_y n_z(1-\cos\Omega)+n_x\sin\Omega & n_z^2(1-\cos\Omega)+\cos\Omega \end{bmatrix} \tag{2.18}$$

The unit vector $\boldsymbol{n}$ has only two independent components, thereby three independent parameters are sufficient to describe a rigid rotation. The point where a positive rotation axis intersects the Earth's surface is called *Euler pole* (Fig. 2.1), its antipodal is called the *antipole*. An Euler pole, expressed through its geographic coordinates (latitude and longitude), and a rotation angle, are the three parameters generally used in plate kinematics to indicate a finite rotation. In Sect. 2.7 we shall learn how to use these finite rotations to describe the kinematics of tectonic plates through the geological time.

Now let us consider again the instantaneous kinematics of a tectonic plate $\mathbf{R}$. Using the expression (2.17), the continuum mechanics analogue of the kinetic energy, $K$, will be given by:

$$K = \frac{1}{2}\int_{\mathbf{R}} \rho(\boldsymbol{r})\, v^2(\boldsymbol{r})\, dV = \frac{1}{2}\int_{\mathbf{R}} \rho(\boldsymbol{r})\, \omega^2 r^2 \sin^2\theta(\boldsymbol{r})\, dV = \frac{1}{2}\omega^2 \int_{\mathbf{R}} \rho(\boldsymbol{r}) \left[r^2 - r^2\cos^2\theta(\boldsymbol{r})\right] dV = \\ = \frac{1}{2}\omega^2 \int_{\mathbf{R}} \rho(\boldsymbol{r}) \left[r^2 - (\boldsymbol{n}\cdot\boldsymbol{r})^2\right] dV \equiv \frac{1}{2} I(\boldsymbol{n})\, \omega^2 \tag{2.19}$$

where $\theta(\boldsymbol{r})$ is the angle between $\boldsymbol{n}$ and $\boldsymbol{r}$ and the quantity $I(\boldsymbol{n})$, which depends from plate geometry, mass distribution, and the rotation axis, is the *momentum of inertia* about the axis $\boldsymbol{n}$:

$$I(\boldsymbol{n}) \equiv \int_{\mathbf{R}} \rho(\boldsymbol{r}) \left[r^2 - (\boldsymbol{n}\cdot\boldsymbol{r})^2\right] dV \tag{2.20}$$

This quantity is a measure of the inertial resistance that a rigid plate opposes to variations of its angular velocity about a rotation axis. Another quantity that can be expressed in terms of Euler vectors is the angular momentum, $\boldsymbol{L}$. Starting from expression (2.5), we can write:

$$\begin{aligned}\boldsymbol{L} &= \int_{\mathbf{R}} \rho(\boldsymbol{r})\, \boldsymbol{r} \times \boldsymbol{v}(\boldsymbol{r})\, dV \\ &= \int_{\mathbf{R}} \rho(\boldsymbol{r})\, \boldsymbol{r} \times (\boldsymbol{\omega} \times \boldsymbol{r})\, dV \\ &= \int_{\mathbf{R}} \rho(\boldsymbol{r}) \left[r^2 \boldsymbol{\omega} - (\boldsymbol{\omega} \cdot \boldsymbol{r})\, \boldsymbol{r}\right] dV \end{aligned} \tag{2.21}$$

A more compact expression can be determined introducing the index notation (see Appendix 1), $x_1 \equiv x$, $x_2 \equiv y$, $x_3 \equiv z$, and Einstein's summation convention. With this notation, it is easy to prove that the angular momentum has the following simple expression in terms of Euler vectors:

$$L_i = I_{ij}\omega_j \tag{2.22}$$

where the quantities $I_{ij}$ form a rank 2 symmetric tensor, which is known as *inertial tensor*:

$$I_{ij} = \int_{\mathbf{R}} \rho(\boldsymbol{r}) \left(r^2 \delta_{ij} - x_i x_j\right) dV; i, j = 1, 2, 3 \tag{2.23}$$

In this expression, the quantity $\delta_{ij}$ represents the *Kronecker delta* ($\delta_{ij} = 1$ if $i = j$, zero otherwise). The components of the inertial tensor depend from the mass distribution and the plate geometry, just like the moments of inertia (Eq. 2.20). Therefore, we expect that a relation exists between these quantities. It is quite evident from (2.23) that the diagonal components of $\boldsymbol{I}$ coincide with the moments of inertia about the three coordinate axes:

$$I_{ii} \equiv I_i = \int_{\mathbf{R}} \rho(\boldsymbol{r}) \left(r^2 - x_i^2\right) dV = I(\boldsymbol{e}_i); \quad i = 1, 2, 3 \tag{2.24}$$

where $\boldsymbol{e}_i$ ($i = 1,2,3$) are the base versors of the coordinate system. In general, it is possible to show that the momentum of inertia of a tectonic plate about an arbitrary rotation axis $\boldsymbol{n}$ can be expressed as a linear combination of the components of the inertial tensor, thereby this tensor contains all the relevant information for the determination of the moment of inertia about any rotation axis. In fact, using Eqs. (2.20) and (2.21) we see that the component of the angular momentum in the direction of $\boldsymbol{n}$ is given by:

$$\boldsymbol{L} \cdot \boldsymbol{n} = \int_{\mathbf{R}} \rho(\boldsymbol{r}) \left[r^2 \omega - (\boldsymbol{n} \cdot \boldsymbol{r})^2 \omega\right] dV = \omega I(\boldsymbol{n}) \tag{2.25}$$

Using Eq. (2.22), and taking into account that $\omega_j = \omega n_j$, we can also write:

$$\boldsymbol{L} \cdot \boldsymbol{n} = L_i n_i = n_i I_{ij} \omega_j = \omega n_i I_{ij} n_j$$

Therefore, a comparison with Eq. (2.25) furnishes:

$$I(\boldsymbol{n}) = n_i I_{ij} n_j \tag{2.26}$$

This expression proves our statement. The previous equations represent the basic framework for the description of the instantaneous kinematics of any rotating rigid plate, independently from the choice of a reference frame. In the next section, we shall consider the specific frames of reference used in plate tectonics.

## 2.3 Reference Frames

Two broad classes of reference frames are used in plate tectonics. *Geocentric reference frames* are *global* frames that are built assuming that the Earth's centre of mass, $\boldsymbol{R}$, coincides with the origin of a Cartesian system of coordinates, so that $\boldsymbol{R} = \boldsymbol{0}$. The best known of these reference frames is the usual *geographic coordinate system*, in which the $z$ axis coincides with the Earth's spin axis, and the $x$ and $y$ axes are in the Equatorial plane and point, respectively, to the Greenwich

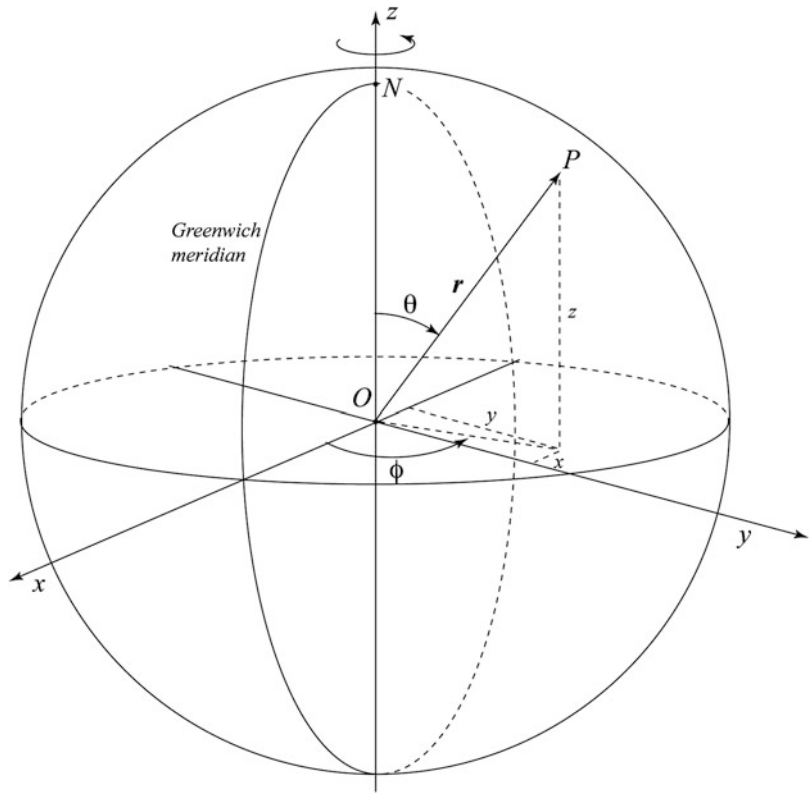


**Fig. 2.2** Cartesian $(x,y,z)$ and spherical $(r,\theta,\phi)$ coordinates of a point $P$ in the geographic reference frame

meridian and 90°E. Clearly, a point in the city of London, on the Eurasian plate, has constant longitude $\phi = 0$ in this reference frame (Fig. 2.2).

In plate kinematics, the Earth is assumed to have a spherical shape, so that the Cartesian coordinates $(x,y,z)$ of a point at distance $r$ from the Earth's centre are related to the geographic coordinates $(\theta,\phi)$, colatitude and longitude, by the following equations:

$$\begin{cases} x = r \sin\theta \cos\phi \\ y = r \sin\theta \sin\phi \\ z = r \cos\theta \end{cases} \tag{2.27}$$

Figure 2.2 illustrates the relation between Cartesian and geographic (spherical) coordinates of a point. Equations 2.27 can be easily inverted to get an expression of the spherical coordinates as a function of the Cartesian components:

$$\begin{cases} \phi = \arctan(y/x) \\ \theta = \arccos(z/r) \\ r = \sqrt{x^2 + y^2 + z^2} \end{cases} \tag{2.28}$$

Another useful geocentric reference frame is the *geomagnetic coordinate system* (e.g., Campbell 2003). This frame is built on the basis of the observation that the present day Earth's magnetic field can be approximated as the field generated by a magnetic dipole placed at the Earth's centre, as we shall see in Chap. 4. Such a dipole has not fixed direction, but precedes irregularly about the North Pole according to the so-called *secular variation* of the core field. It is mathematically represented by a magnetic moment vector, $\boldsymbol{m}$, which currently (December 31st 2013) points to a location placed in the southern hemisphere, at about (80.24°S, 107.46°E). This location is called the *geomagnetic South Pole*, and its antipodal point at (80.24°N, 72.54 W) is known as the *geomagnetic North Pole*. The axis passing through these two points defines the $z$-axis of the geomagnetic reference frame. The $x$-axis of this coordinate system is chosen in such a way that the prime meridian passes through the geographic South Pole. Finally, the $y$-axis will be also placed in the geomagnetic dipole equator, 90° from the $x$-axis.

In a *paleomagnetic reference frame,* the $z$-axis always coincides with the apparent directions of the Earth's spin axis as determined by a sequence of *paleomagnetic* poles (Chap. 6). In these frames, the longitude of a point is relative to an arbitrarily selected location on a reference continent. For example, if the central African craton is chosen to be the reference continent, then we could select a reference site in central Africa and assign to this location a fixed longitude coinciding with the present day value. This approach can be found in Besse and Courtillot (1988). Other more complex techniques assign a changing longitude (in the paleomagnetic reference frame) to the reference site according to specific algorithms (e.g., Schettino and Scotese 2005), but in any case the longitude of any other point is referred to this site and not to the Greenwich meridian.

The second broad class of reference frames is represented by *local coordinate systems*, which have the following common features: (*a*) the origin is an observation point at the Earth's surface (seismic station, magnetic field measurement point, etc.); (*b*) the $z$-axis is aligned with the vertical to the observation point (plumb line), so that the $xy$ plane is a tangent plane to the Earth's surface. These reference frames are usually employed to represent the geometry of faults, focal mechanisms of earthquakes, and magnetic field measurements, but they can be used to characterize any local vector or tensor quantity of geophysical interest (Cox and Hart 1986). Figure 2.3 illustrates the conventions used in geomagnetism, where the $z$-axis is directed downwards, the $x$-axis is directed northwards, and the $y$-axis is directed eastwards. In this instance, the Earth's core field vector, $\boldsymbol{F}$, can be represented by three Cartesian components ($X$,$Y$,$Z$) or, alternatively by its *declination*, $D$, by an *inclination*, $I$, and a magnitude, $F$.

From Fig. 2.3, we see that the equations of transformation from ($F$,$D$,$I$) to ($X$,$Y$,$Z$) are:

$$\begin{cases} X = F\cos I\cos D \\ Y = F\cos I\sin D \\ Z = F\sin I \end{cases} \tag{2.29}$$

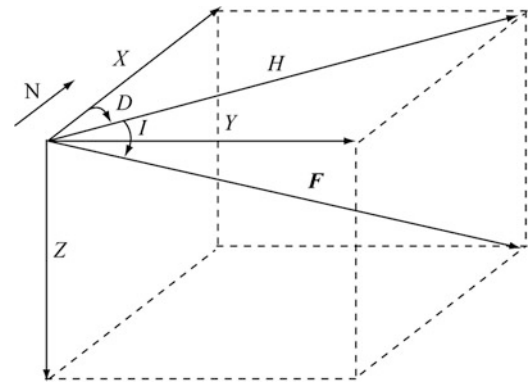


**Fig. 2.3** Local Cartesian components of the Earth's main field, $\boldsymbol{F} = (X,Y,Z)$ and horizontal component, $H$. The declination, $D$, is the azimuth of $H$, while the inclination, $I$ is the angle between $\boldsymbol{F}$ and $H$, positive downward

The inverse transformation can be easily obtained from these expressions. It follows that:

$$\begin{cases} D = \arctan(Y/X) \\ I = \arcsin(Z/F) \\ F = \sqrt{X^2+Y^2+Z^2} \end{cases} \tag{2.30}$$

Finally, form the definition of horizontal component, $H = \sqrt{X^2+Y^2}$, it follows that the inclination can be also expressed as a function of $Z$ and $H$:

$$I = \arctan(Z/H) \tag{2.31}$$

We emphasize that although these equations refer to the specific case of the geomagnetic field, they can be used to express the components of any other vector quantity in a local coordinate system at the Earth's surface.

## 2.4 Plate Boundaries

Three fundamental kinds of plate boundaries can be observed in the oceanic domain, which have three counterparts in continental areas. In the oceans, we find mid-ocean ridges, trenches, and strike-slip faults. The continental analogues of these tectonic structures are, respectively, rifts, collision zones, and transcurrent faults. Now we

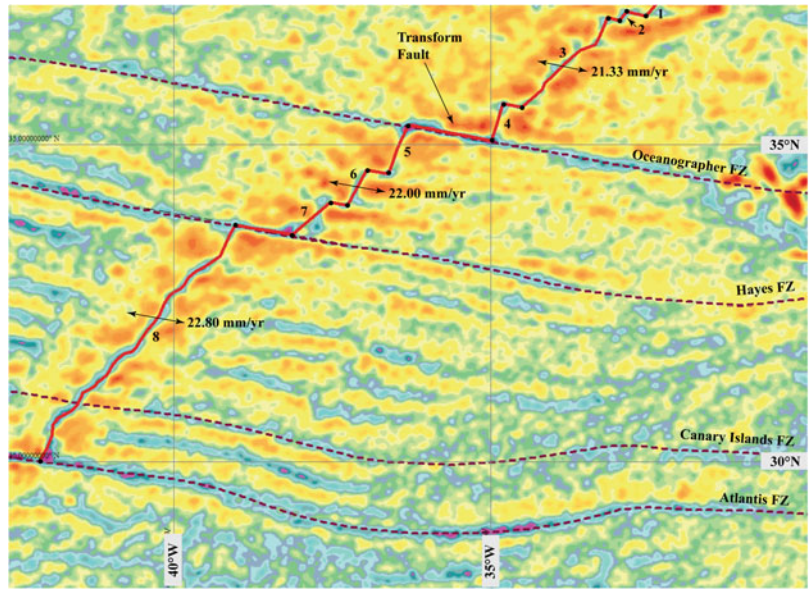


**Fig. 2.4** Geometry of the Mid-Atlantic ridge in the central Atlantic area (*red line*). *Dashed lines* are major fracture zones. *Black dots* bound transform faults and spreading segments along the ridge. Numbers label the eight segments identified along this tract of the ridge. *Double arrows* indicate directions of spreading. Also shown is the full spreading rate. The background image, showing free-air gravity anomalies (Sandwell and Smith 1997), enhances the location of the axial zone of the ridge and the track of the fracture zones (*FZ*)

are going to consider all these faults and systems of faults from the point of view of plate kinematics. Mid-ocean ridges are extensional boundaries in the oceanic domain. We have seen in Chap. 1 that these features are spreading centers, where new oceanic crust is passively accreted as a consequence of divergent motion between two tectonic plates. These boundaries are formed by sequences of ridge segments that are linked together by transform faults, as illustrated in Fig. 2.4.

Transform faults are faults with a pure strike-slip kinematics and a strike that reflects the local direction of instantaneous motion between two plates. Therefore, these faults are always parallel to velocity vectors of relative motion. This relative motion is clearly left-lateral strike-slip in the case of dextral offset of the spreading segments and vice versa. For example, all the transform faults shown in Fig. 2.4 imply left-lateral strike-slip motion. The adjective "transform" that is attributed to these tectonic features arises from the fact that they generate active bathymetric discontinuities, as far as the two plates move apart. Such discontinuities are called fracture zones and represent linear features that apparently pursue the transform faults toward the continental margins (Fig. 2.4). Therefore, the latter seem to be "converted" into a different

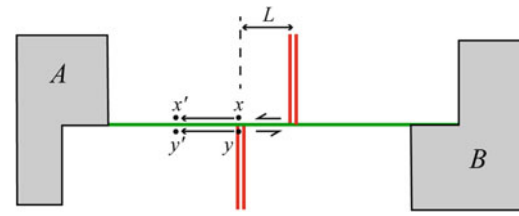


**Fig. 2.5** Age discontinuities across fracture zones. Two points, $x$ and $y$, on plate $A$, having very different ages, are at contact through a transform fault. When the two points are moved to locations $x'$ and $y'$, their difference of age, $\Delta T$, is conserved

class of faults, characterized by vertical slip. The explanation of this phenomenon is quite simple.

Let $v$ and $L$ be, respectively, the relative velocity along a transform fault and its length, and consider a point $x$ close to one of the ends of the fault (Fig. 2.5). The age of formation of the crust at $x$ is $T(x) = 2L/v$, because the velocity of accretion on both sides of the ridge is on average $v/2$. This point is clearly at contact with another point, say $y$, which is close to the ridge and has age $T(y) = 0$. Therefore, the difference of age between $x$ and $y$ is $\Delta T = 2L/v$. At any successive time $t$, these two points will be displaced away from the ridge by the same offset, to two close locations $x'$ and $y'$, independently from any change of $v$ with time. Therefore, they

will remain neighbor points. Thus, the motion of points $x$ and $y$ away from the ridge will leave a linear track of age discontinuities, $\Delta T$, which crosses the whole oceanic part of the plate and reaches the continental margin, as illustrated in Fig. 2.5.

Furthermore, a specular trace will form on the conjugate plate, reaching the opposite continental margin. Generally, fracture zone tracks are easily identified on bathymetric or gravity anomaly maps (Fig. 2.4), because age discontinuities are always associated with bathymetric gaps. In Chap. 12, we shall prove that the depth to the sea floor increases with the crustal age, so that an age discontinuity always implies a bathymetric gap. Despite the invariance of the age discontinuity, $\Delta T$, along a fracture zone track, the difference of depth across the two sides changes with time, because the rate of sea floor subsidence is not a linear function of time, especially during the first ~100 Myrs. This implies a lateral discontinuity in the amount of subsidence, so that fracture zones can be assimilated to vertical faults characterized by vertical slip. Therefore, as suggested by their name, transform faults are converted to a different class of faults, fracture zones, which are not associated with horizontal slip and do not represent plate boundaries, but simply are active bathymetric gaps associated with discontinuities in the age of the sea floor. Finally, it is necessary to keep in mind that although transform faults and ridge segments are very different tectonic features, they are part of unique plate boundaries, namely the mid-ocean spreading centers. In other words, they cannot be considered as distinct classes of plate boundaries.

Now let us consider the kinematics along mid-ocean spreading ridges. In principle, these features should be orthogonal to the relative velocity field between two plates. However, the example of Fig. 2.4 shows that the azimuth of the segments composing a mid-ocean ridge is not necessarily 90° from the direction of spreading. This phenomenon is called spreading obliquity, and is quantified measuring the angle between the normal to the ridge trend and the direction of a transform fault. Observation suggests that the spreading obliquity is particularly strong in the case of slow-spreading ridges (e.g., Southwest Indian Ridge and North Atlantic Ridge), where it could be as high as ~80° (Whittaker et al. 2008). It is always necessary to take into account of this parameter when interpreting marine magnetic data. In Chap. 5, we shall learn how to deal with oblique spreading. In general, plate kinematics studies require an accurate preliminary mapping of the plate boundaries through GIS software, especially in the case of mid-ocean ridges. In this instance, the location and the geometry of the segments forming a spreading center, as well as the trace of transform faults, can be established by close inspection of the axial valley topography and by the analysis of gravity anomalies (Fig. 2.4). However, in most cases a precise definition of the ridge segments will require a successive refinement, based upon the analysis of marine magnetic anomalies, as we shall see in Chap. 5. The overall geometry of mid-ocean ridges is not constant through the geological time. It is subject to changes, even in absence of variations of relative motion, as a consequence of three basic mechanisms: spreading asymmetry, ridge jumps, and ridge segment reorientations. Figure 2.6 illustrates these three possibilities.

Spreading asymmetry occurs when the rate of accretion of new crust is not uniform across the two sides of a spreading segment (Fig. 2.6a). Let $v$ be the full spreading rate along a ridge segment. This quantity clearly coincides with the local magnitude of the velocity vector of a plate $A$ with respect to another plate $B$.

We can introduce a quantity $-1 < \alpha < +1$, such that the widths of the crust accreted to the right and left sides of a spreading segment in a time interval $\Delta t$ are:

$$\Delta x_R = \frac{1}{2}(1+\alpha)\, v\Delta t;\ \Delta x_L = \frac{1}{2}(1-\alpha)\, v\Delta t \tag{2.32}$$

The quantity $\alpha$ is an expression of the asymmetry of spreading across a mid-ocean ridge segment. In normal conditions ($\alpha = 0$), a spreading segment moves at velocity v/2 with respect to each of the conjugate plates. In the case of spreading asymmetry, the segment will move at a

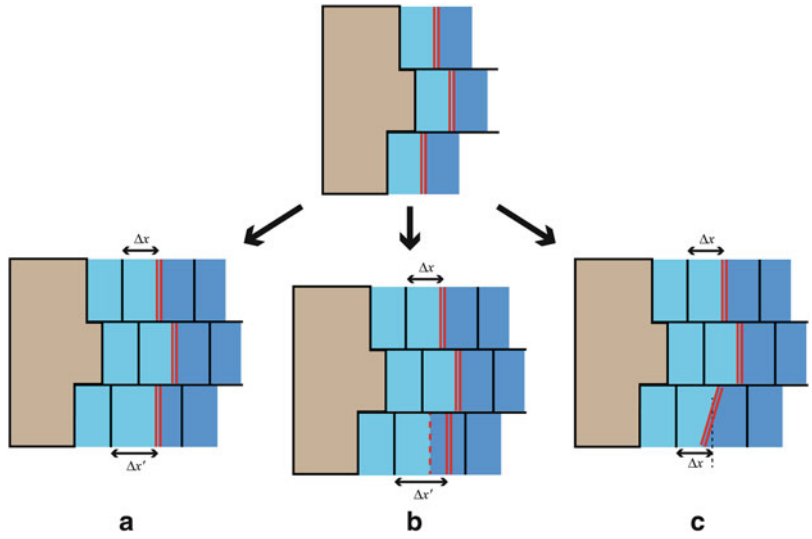


**Fig. 2.6** Mechanisms responsible for the changing geometry of mid-ocean ridges. After a time interval $\Delta t$, a normal ridge segment travels a distance $\Delta x = ½v\Delta t$. In **a** the third segment shows spreading asymmetry, because a larger amount of crust is accreted to the left side. In **b** there is no spreading asymmetry, but after a time interval $\Delta t$ the third segment becomes extinct and a new spreading segment forms at another location, transferring a piece of oceanic lithosphere to the conjugate plate. In **c** the orientation of the third segment changes as a consequence of variations of spreading asymmetry along the same segment

velocity $v' = (1 + \alpha)v/2$ with respect to one plate, and $v'' = (1-\alpha)v/2$ with respect to the conjugate plate. Therefore, any variation of asymmetry between neighbor segments of a mid-ocean ridge will modify the geometry of the plate boundary, as illustrated in Fig. 2.6a. Another mechanism, which is responsible for changing the geometry of the mid-ocean ridges, is represented by the ridge jumps (Fig. 2.6b). In this instance, a spreading segment is abandoned and a new center of spreading forms at a certain distance from the original position. The final effect is apparently similar to that associated with spreading asymmetry. However, in this instance the piece of intervening lithosphere between the old and the new segments will be accreted instantaneously to the conjugate plate, determining a complex pattern of the magnetic lineations and possible errors in the interpretation of the sea floor magnetization pattern. This problem will be considered in detail in Chap. 5. Finally, the analysis of marine magnetic anomalies shows that the geometry of the mid-ocean ridges can be modified by reorientations of the spreading segments. This phenomenon is ultimately a special form of spreading asymmetry, which may linearly change within the same segment, determining a continuous rotation that accommodates the reorientation. The mechanism was originally proposed by Menard and Atwater (1968) to explain the effect of changes of the Euler pole of relative motion, and consequently of the spreading directions, on the mid-ocean ridge geometry. A series of subsequent studies (e.g., Hey 1977; Hey et al. 1988) proposed a much more complex mechanism for the reorientation of the spreading segments, known as ridge propagation. However, the simple process of segment rotation is a still valid model in absence of Euler pole changes.

Apart from the present day system of mid-ocean ridges, the oceanic domain also includes many extinct plate boundaries that in origin were spreading centers. Some of these extinct boundaries were produced by large-scale ridge jumps, which left wide remnant oceanic basins. Important examples are the proto-Atlantic Basin in the central Atlantic (e.g., Schettino and Turco 2009), the Mascarene Basin in the Indian Ocean (Schlich 1974), the Rockall Trough (Smythe 1989) and the Norway Basin (e.g., Gaina et al. 2009) in

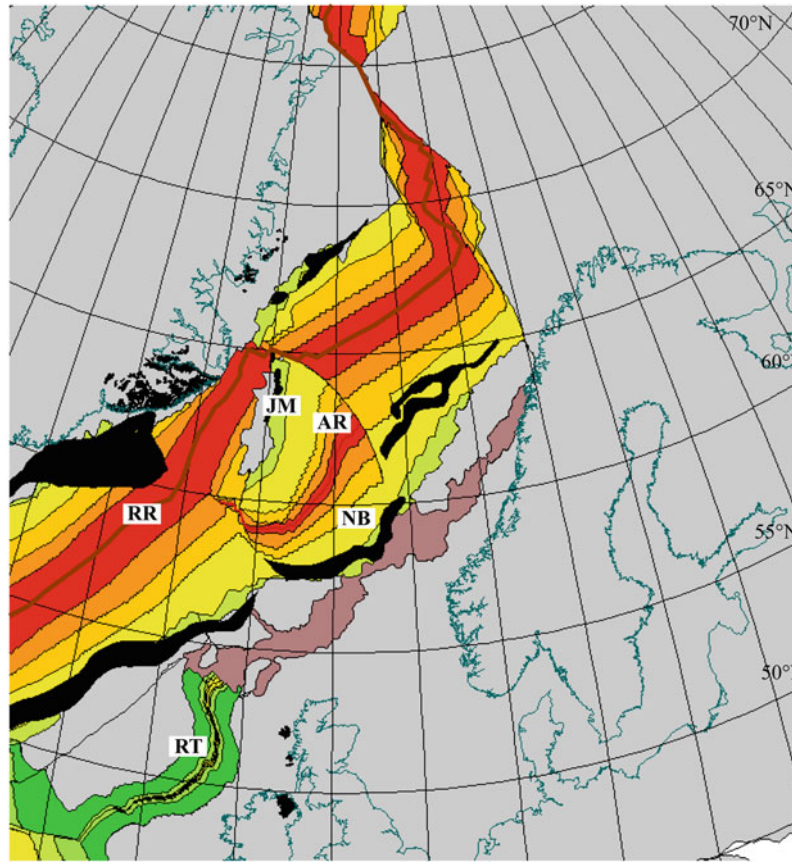


**Fig. 2.7** Reconstruction of the North Atlantic region in the early Burdigalian (∼20 Ma). The continental lithosphere is shown in *grey*. Thinned continental areas are shown in *light brown*. Regions in *black* are LIPs. Present day coastlines are shown for reference. Late Cretaceous oceanic crust is shown by *green* colours, Eocene crust is shown by *yellow* to *orange* colours, Oligocene oceanic crust is shown in *red*. *RR* Reykjanes Ridge, *RT* Rockall Trough, *NB* Norway Basin, *JM* Jan Mayen microcontinent, *AR* Aegir Ridge

the North Atlantic. Figure 2.7 illustrates a plate reconstruction of the North Atlantic region at ∼20 Ma, shortly after a westward ridge jump that determined the extinction of the Aegir Ridge and cessation of extension in the Norway Basin. The newly formed spreading segment rifted the Greenland margin, determining the separation of a continental fragment: the Jan Mayen microplate (Jung and Vogt 1997).

Other extinct plate boundaries formed as a consequence of cessation of divergent motion between the conjugate plates, not because of a reorganization of the boundary. In this instance, a direct causal relation with a nearby onset of spreading is missing, although the final result is the same: a remnant oceanic basin and an extinct ridge testifying the former existence of divergent plate motions. Important examples of remnant oceanic basins associated with ridge extinction are the Jurassic Ligurian Basin in the western Mediterranean (Schettino and Turco 2011), the Labrador Basin (Roest and Srivastava 1989), the South China Sea (Briais et al. 1993), the Somali Basin (e.g., Coffin and Rabinowitz 1987), the Gulf of Mexico (Ross and Scotese 1988), the Amerasian Basin (Rowley and Lottes 1988), and the Tasman Sea (Gaina et al. 1998).

The second kind of oceanic plate boundaries is represented by the trench zones (or subduction zones). These are convergent boundaries, where oceanic lithosphere bends and sinks into the asthenosphere. The structural, stratigraphic, and petrologic features associated with trenches and island arcs have been described extensively in the geologic literature (e.g., Frisch et al. 2011). Here we shall consider only some aspects that are significant for plate kinematics. The geometry of a subduction zone is that of a small circle arc, both if we consider the subducting lithosphere as a flexible-inextensible spherical shell (Frank 1968) or as a body that can be extended or shortened during the passive sinking in the mantle (e.g.,

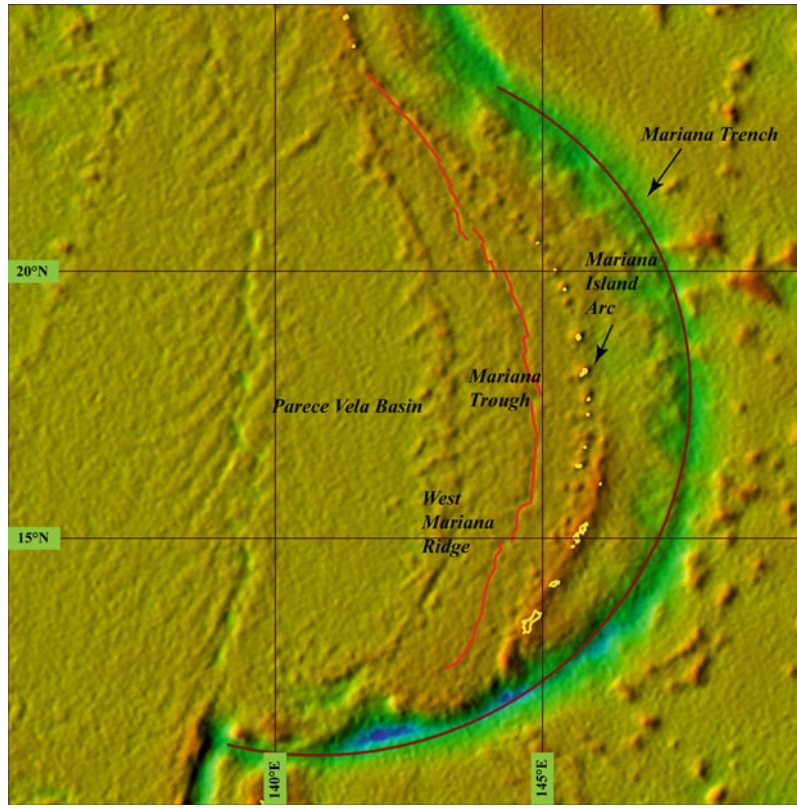


**Fig. 2.8** Geometry of the Mariana subduction zone. The *brown line* represents the best-fit *small circle* to the trench zone, determined using the algorithm of Schettino and Tassi (2012). The background image shows the free-air gravity anomaly field (Sandwell and Smith 1997). The *red line* is the active back-arc spreading center (see text). The West Mariana Ridge is an extinct island arc

Schettino and Tassi 2012). Figure 2.8 shows the example of the Mariana subduction zone in the western Pacific, which forms an almost perfect small circle arc. We have already mentioned that the geometry of tectonic plates can be represented by spherical caps. Therefore, trench zones can be viewed as the surficial hinge lines of bending of spherical caps, associated with the subduction of oceanic lithosphere. Such hinge lines do not have constant curvature, but their geometry generally varies to accommodate changes of the relative velocity field of convergence. For example, Fig. 2.8 shows that the present day Mariana Trench is deforming as a consequence of an extensional process in the back-arc area, accompanied by the formation of new oceanic crust along a back-arc spreading center in the Mariana Trough. This spreading ridge is placed to the East of an extinct island arc, the West Mariana Ridge, which is representative of a previous geometry of subduction. Almost every subduction zone shows evidence of back-arc activity, either currently or sometime in the past. Even in the case of Andean-like trench zones, where the oceanic lithosphere is subducting beneath a continent, we observe back-arc deformation of the continental margin in the geologic past (e.g., Dalziel 1981; Ramos et al. 2002), to the point that the present day western margin of South America has the shape of a sequence of arcuate hinge lines, which can be represented anyway by small circle arcs.

An important aspect of the subduction kinematics is represented by the velocity relations between subducting plate, hinge zone, and upper plate (Fig. 2.9). Hamilton (2002) criticized what he defined a widespread misconception in the Earth Sciences community, consisting in the view that subducting plates roll over stationary hinge lines and slide down fixed slots. In reality, in a reference frame fixed to an unsubducted plate $A$, the hinge line $H$ always moves toward the oceanic foreland with some velocity $v_{HA}$, just as the margin of the overriding plate, $B$, and with equal velocity (because $v_{BH} = 0$). If we consider a reference frame fixed to the top of the transition zone, $O$, then the hinge line and the overriding

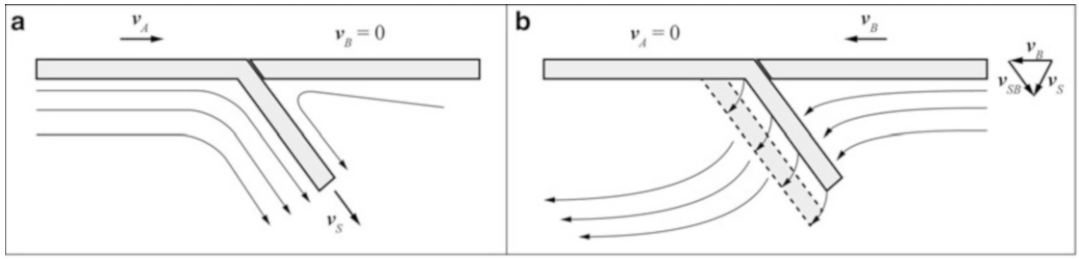


**Fig. 2.9** Cross-sections illustrating the kinematics of a subduction zone. Velocity vectors $\boldsymbol{v}_A$, $\boldsymbol{v}_B$, and $\boldsymbol{v}_S$ are relative to the lower mantle, $\boldsymbol{v}_{SB}$ is the slab velocity relative to plate *B*. *Lines* in the upper mantle represent streamlines, everywhere parallel to mantle velocity vectors (Chap. 13). Two end-member dynamic scenarios are shown. Any other dynamic scenario results from superposition of these two basic configurations

plate will move at a velocity given by:

$$\boldsymbol{v}_H = \boldsymbol{v}_B = \boldsymbol{v}_{HA} + \boldsymbol{v}_A \tag{2.33}$$

If the relative hinge line velocity $v_{HA}$ increases, for any reason, then the overriding plate margin will be subject to back-arc extension, in order to preserve the coupling between margin and hinge line, a phenomenon which is known as *trench retreat*. Conversely, any decrease of $v_{HA}$ will lead to episodes of back-arc compression and shortening. In general, the deformation of active continental margins and island arcs is an expression of both spatial and temporal changes of the relative velocity field between the convergent plates, as well as of variations in the hinge line velocity $v_{HA}$. Regarding the possibility that subducting plates roll over stationary hinge lines, thereby they would slide down fixed slots, this is not a wrong interpretation of the subduction process but one of two end-member geodynamic configurations at a subduction zone, as illustrated in Fig. 2.9a. In fact, when the velocity $v_B = 0$, a subducting plate effectively bends and rolls over a fixed hinge line in the mantle reference frame, dragging the surrounding asthenosphere, as we shall prove in Chap. 13. In these dynamic conditions, the pull exerted by the sinking slab is balanced by the resistive viscous drag and subduction tends to proceed at constant velocity. However, the active drag exerted by the corner asthenospheric flow below the overriding plate *B* pulls this plate trenchward, so that *B* will acquire a small velocity $\boldsymbol{v}_B$ opposite to $\boldsymbol{v}_A$. The velocity $\boldsymbol{v}_B$ increases progressively until the additional frictional resistance that is generated at the trench balances the trenchward asthenospheric drag. If the starting dynamic configuration is that illustrated in Fig. 2.9b, so that the overriding plate velocity $v_B \neq 0$ while $v_A = 0$, the induced oceanic corner flow below *A* drags actively this plate trenchwards, thereby *A* will acquire a small velocity opposite to $\boldsymbol{v}_B$. Therefore, the final equilibrium configuration will be similar to the previous one. Finally, hypothetical scenarios such that the two converging plates move in the same direction but with different velocity (in the upper mantle reference frame) cannot be stable geodynamic configuration. In fact, in this instance the excess hydrodynamic resistance exerted on the slab should be supplied by additional torques other than the known driving forces of plate tectonics (Chap. 12). Subduction roll-back is the geodynamic process determining the progressive oceanward migration of the trench zone in the upper mantle reference frame. In fact, in a reference frame fixed to the subducting plate *A* the hinge line always migrates toward the foreland of *A*.

The third kind of oceanic plate boundary is represented by strike-slip faults, which are characterized by pure or prevalent left-lateral or right-lateral motion. Differently from transform faults, which must be considered in the context of mid-ocean spreading centers, these structures are truly independent plate boundaries, which can be linked to mid-ocean ridges, trenches, or other strike-slip faults. In the present day

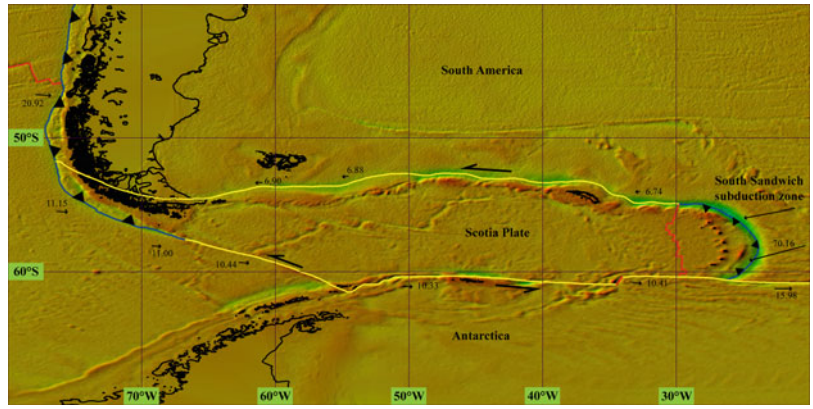


**Fig. 2.10** Strike-slip plate boundaries in the Scotia Sea (*yellow lines*). The *arrows* represent direction and magnitude of the relative velocity field between plates pairs. Numbers are magnitudes of velocity in mm/year

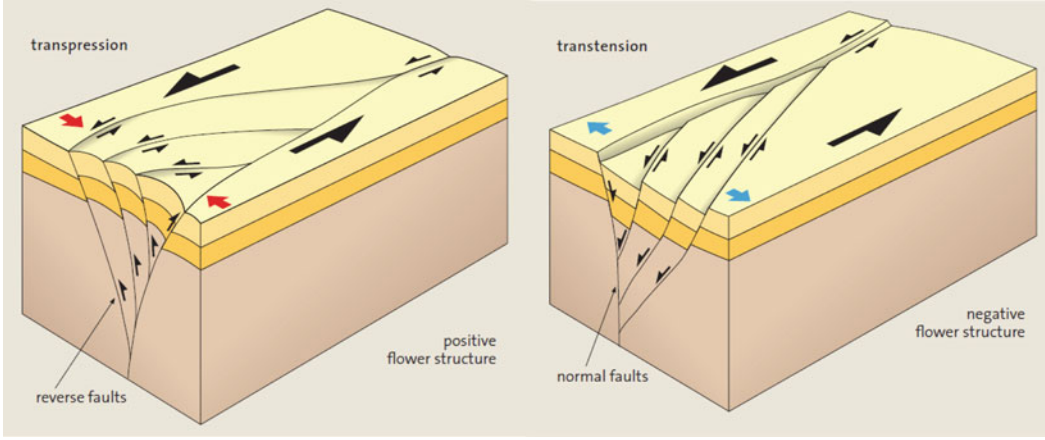


**Fig. 2.11** Flower structures associated with left-lateral transcurrent motion (From Frisch et al. 2011)

oceanic regions, only few examples can be found that belong to this class of boundaries. In the South America – Antarctica – Pacific system, the northern, the southern, and part of the western boundary of the Scotia plate are classic examples of strike-slip plate boundaries (Fig. 2.10). Other important examples are the Owen Fracture Zone in the Arabian Sea (Fournier et al. 2001), the Cayman Trough transform system along the present day North America – Caribbean plate boundary (Pindell et al. 1988), and the McDougall Ridge in the southwest Pacific (Lebrun et al. 2003).

We have mentioned that the continental counterparts of the oceanic plate boundaries are zones of active rifting, collision, or transcurrent motion. It is interesting to note that while the average relative velocity along rifts and orogenic belts is one order of magnitude less than along the oceanic domain analogues, in the case of transcurrent boundaries the opposite is generally true. For example, the magnitude of strike-slip motion along modern transcurrent faults like the San Andreas Fault in western US (Pacific – North America boundary) and the North Anatolian Fault in Turkey (Anatolia – Eurasia boundary) is respectively of ~47 mm $yr^{-1}$ and ~29 mm $yr^{-1}$, while less than 8 mm $yr^{-1}$ and 11 mm $yr^{-1}$ can be observed, respectively along the Owen Fracture Zone and around the Scotia plate. From the structural point of view, transcurrent boundaries are generally associated with characteristic flower structures at the upper crustal level, whose complexity arises from the necessity of accommodating transpressional or transtensional components within a prevalent strike-slip kinematics. Figure 2.11 illustrates the typical structural setting along these boundaries.

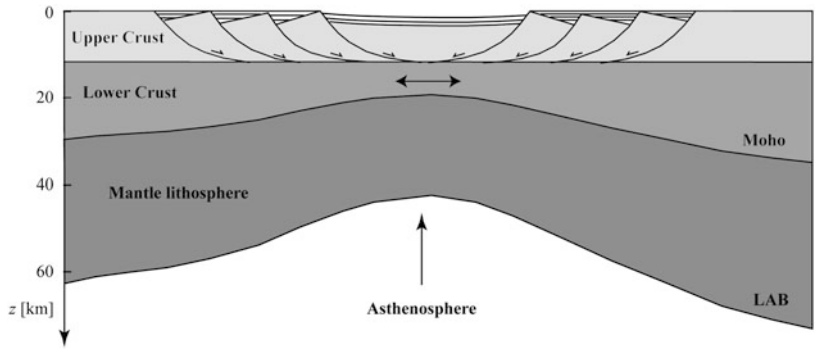


**Fig. 2.12** Uniform stretching in McKenzie's (1978) model of rifting

Important modern examples of transcurrent boundaries are the San Andreas (e.g., Beck 1986) and North Anatolian (Sengör 1979) faults mentioned above, the East Anatolian Fault of southern Turkey (McKenzie 1976), and the Dead Sea Fault Zone in Middle East (e.g., Garfunkel 1981; Butler et al. 1997).

Rift zones are extensional plate boundaries, which usually exhibit complex systems of normal faults, linked together by transfer zones. The basic model of evolution of the basins associated with these fault systems is McKenzie's (1978) model, which assumes that the crustal stretching generated by an extensional force field occurs through a uniform continuous thinning of the ductile lower crust, a process that is known as pure shear. Conversely, extension in the brittle upper crust would be accommodated symmetrically by listric (upward-concave) normal faults, as shown in Fig. 2.12. In the model of McKenzie (1978), rifting events start with rapid stretching of the continental lithosphere, which determines passive upwelling of asthenosphere (Fig. 2.12). This stage is characterized by faulting of the upper crust and tectonic subsidence. Then, on a time scale of 50–100 Myrs conductive cooling of the lithosphere determines an increase of thickness and a phase of slow thermal subsidence that is not accompanied by faulting.

The amount of thinning is measured by the *stretching factor*, β, which is simply given by: $\beta = H_1/H_2$, where $H_1$ and $H_2$ are respectively the average thicknesses of the lithosphere at the beginning and at the end of the phase of tectonic subsidence. Although McKenzie's model furnishes a simple and elegant picture of the thermal evolution of rift basins, many conjugate pairs of continental margins show an asymmetric pattern of faulting and the presence of exhumed lower crust, which cannot be explained by the symmetric model. Wernicke (1985) proposed an alternative asymmetric model of rifting that describes accurately many geological features of these zones (Fig. 2.13).

The key difference of Wernicke's model with respect to McKenzie's model is the recognition of low-angle detachment faults at crustal scale and simple shear (that is, localized, non-distributed shear) as the main mechanisms of lithospheric thinning during rifting. In general, several successive studies (e.g., Buck 1991; Brun 1999; Corti et al. 2003) have shown that the models of McKenzie and Wernicke must be considered as descriptions of distinct modes of rifting. Depending from crustal thickness, heat flow, and rate of extension, we can distinguish two basic modes of rifting: (a) a wide rift mode, characterized by high thinning of the crust and the mantle lithosphere over an area larger than ∼100 km, and (b) a narrow rift mode, in which extension by normal faulting is concentrated in a limited area (less than ∼100 km wide). Classic modern examples of wide and narrow rifts are respectively the Basin and Range region of western US (Hamilton 1987) and the East African Rift (e.g., Jestin et al. 1994). A transitional mode of

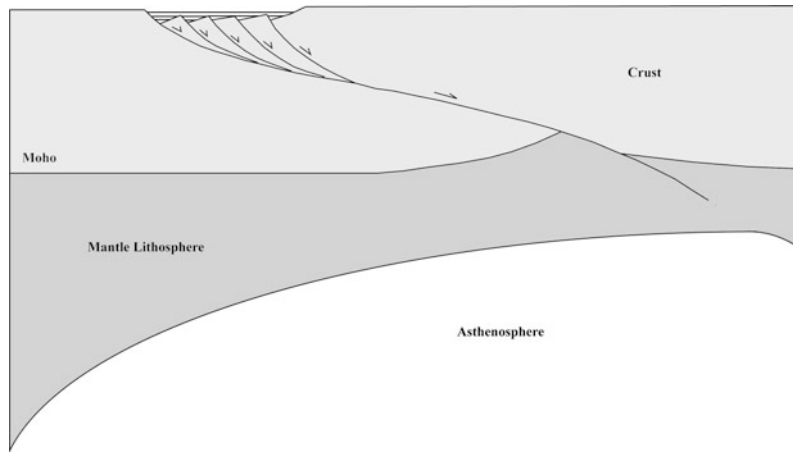


**Fig. 2.13** The simple shear model of rifting of Wernicke (1985)

continental extension is represented by the so-called core complexes, in which high-grade metamorphic rocks from the middle to lower crust are exposed at the surface, surrounded and overlain by low-grade metamorphic rocks. This rifting mode requires high extension rates over narrow zones and an extremely weak, low-viscosity lower crust. In this instance, while extension proceeds, a lower crust inflow from the surrounding region keeps the topography uniform.

Orogenic belts represent the last kind of continental plate boundaries. These are collisional structures that should be distinguished from other kinds of mountain belts, for example from orogens associated with accretionary wedges, like the northern Apennine chain of Italy (Treves 1984), or from Andean-type orogens associated with subduction magmatism and accretion of exotic terranes. Orogenic plate boundaries are the product of continental collisions, which follow the closure of intervening oceans in the context of the Wilson cycle (see Sect. 1.3). The tectonic style of these compressive structures is sometimes called the Alpine style of orogeny (e.g., Frisch et al. 2011), essentially because the spectacular Alpine-Himalayan belt, extending from western Europe to China, is the unique example of active orogenic boundary in the modern Earth. The formation of this mountain belt started after the collision of three continental masses, Africa, Arabia, and India, with the southern Eurasian margin during the Eocene (∼50 Ma). This event followed the closure of the neo-Tethys ocean, a wide oceanic domain that existed between Gondwana and Eurasia since the early Mesozoic (e.g., Schettino and Turco 2011). The collisional structures of this orogenic belt are still active. This is confirmed both by the diffuse seismicity (Fig. 2.14) and by space geodetic observations across the mountain ranges (Kreemer et al. 2003). Figure 2.14 shows the chain of convergent and transpressive boundaries composing the Alpine-Hymalaian belt. In the next section we shall learn how the set plate boundaries that are active at any given time can be linked together to form a plate tectonic configuration.

## 2.5 Triple Junctions

Both the direct observation of modern plates and plate reconstructions show that plate boundaries are joined together in groups of three, at locations that are called *triple junctions*. The lack of higher order junctions is not casual but depends from their instability. For example, it is easy to show that a four-order junction always splits into two triple junctions (e.g., Cox and Hart 1986). McKenzie and Morgan (1969) showed that there are 16 possibilities to form triple junctions by linking three plate boundaries at a point. If we designate by $R$, $T$, and $F$, respectively a mid-ocean ridge, a trench, and a strike-slip fault, then

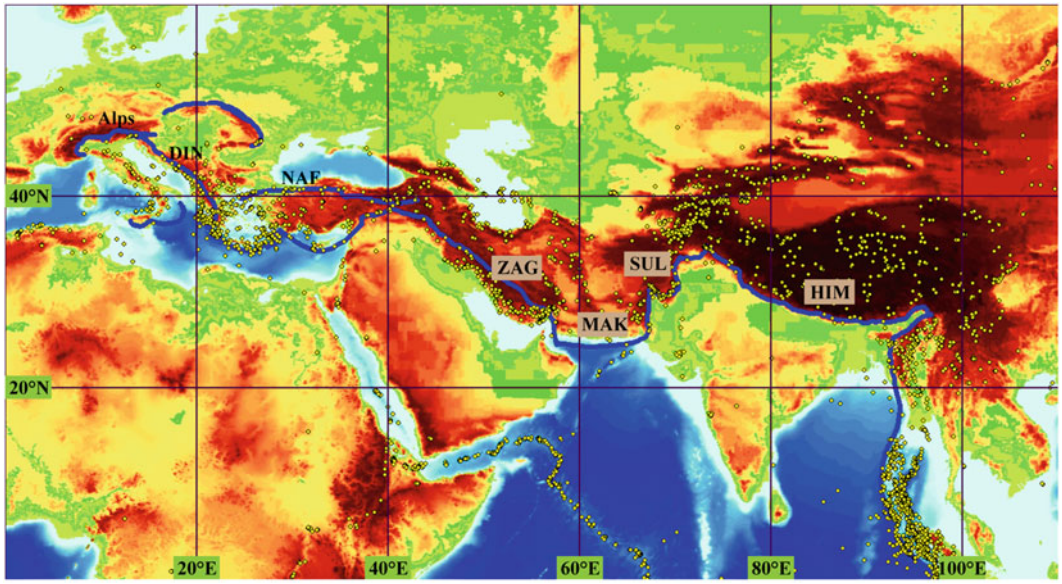


**Fig. 2.14** The Alpine-Himalayan collisional orogen. This belt is composed by several plate boundaries linked together (*blue lines* with labels). From the West, they are: Alps, Dinarides (*DIN*), the North Anatolian Fault (*NAF*), the Makran subduction zone (*MAK*), Sulaiman ranges (*SUL*), and Himalayas (*HIM*). *Yellow dots* are earthquake epicenters in the Harvard CMT catalog

the symbol *RRR* can be used to indicate a triple junction where three spreading ridges meet, *TTR* would indicate a link between two trenches and a ridge, and so on. At any given time, a plate tectonic configuration can be represented by a graph $G(j,b)$ (in the sense of Computer Science, e.g., see Gould 1988 and Appendix 2) having $j$ degree-three nodes and $b$ edges, corresponding respectively to triple junctions and plate boundaries. In this representation, which is useful to investigate the topological properties of the global system of tectonic plates, a plate $P$ is defined by the ordered cyclic sequence $\{J_1,J_2,\ldots,J_n\}$ of triple junctions that tie its boundaries. It should be noted that in this representation the exact geometry of the plate boundaries is unessential, because what we are describing is a system of relations between tectonic plates, their interactions, not the specific geologic details that implement them. If $J$ is an arbitrary node in $G(j,b)$, then $J$ is a vertex belonging simultaneously to three adjacent cyclic sequences. Starting from this node, the sequence of triple junctions defining one of the corresponding tectonic plates is obtained applying the following simple traversal algorithm:

**Algorithm 2.1 (Plate Traversal Algorithm)**

1. Select an arbitrary edge of the starting node $J$;
2. Move to the neighbor node through the selected edge. If this is the starting node $J$, then stop;
3. Now you have two alternative (left and right) edges to leave the current node. Select the left edge;
4. Jump to step #2.

In this algorithm, the choice of one of the three plates associated with $J$ is performed implicitly at step #1 through the selection of a starting edge. The algorithm can be used as a base for the design of more sophisticated computational procedures that investigate the structure of a global plate tectonic configuration.

The theoretical definition of tectonic plates discussed above allows to classify them according to the number of triple junctions that tie the corresponding sequence of plate boundaries. We define the order $N$ of a tectonic plate as the number of triple junctions that are traversed applying algorithm 2.1, as illustrated in Fig. 2.15. Figure 2.16 shows the present day plate tectonic

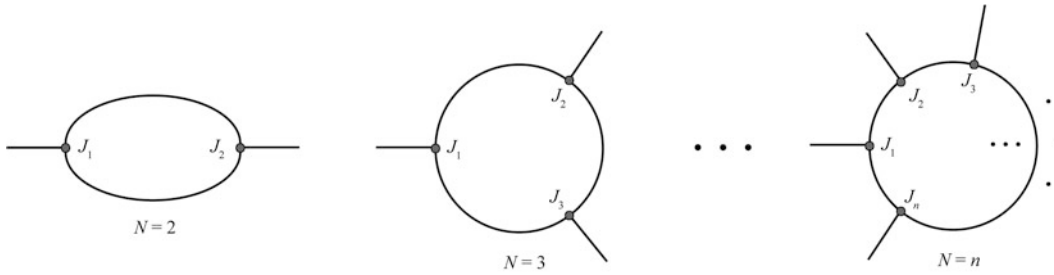


**Fig. 2.15** Definition of the *order N* of a tectonic plate

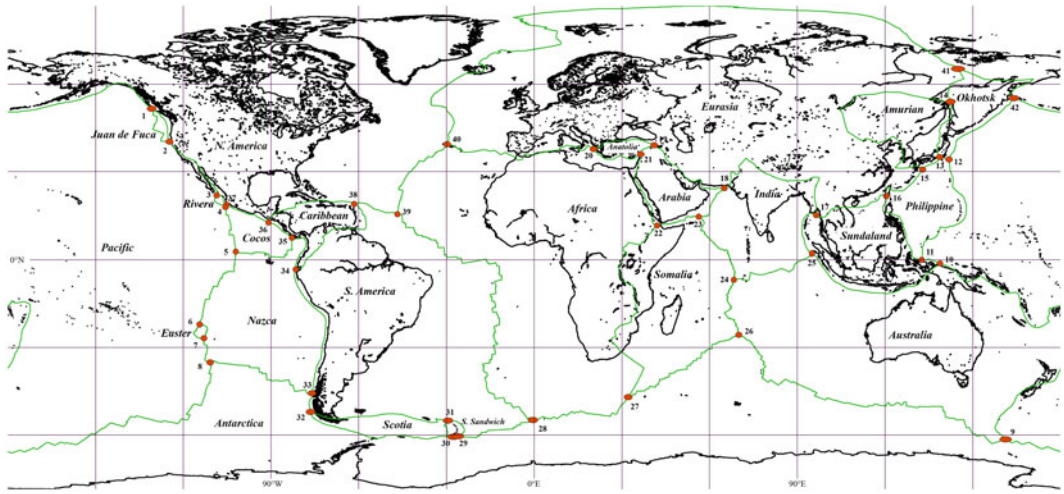


**Fig. 2.16** Modern plate tectonic configuration and triple junctions. Plate boundaries are a slightly modified version of those proposed by Bird (2003). There are 23 major plates, 42 triple junctions (*red circles*), and 63 plate boundaries (*green lines*)

configuration, assuming a simplified version of the plate boundaries proposed by Bird (2003). This configuration does not include plates and microplates whose relative velocity is negligible with respect to adjacent plates, for example Adria in the central Mediterranean, or that are expression of forearc deformation, such as the Burma platelet in Southeast Asia (e.g., Vigny et al. 2003). In addition, it does not include small triple junction microplates such as the Juan Fernandez (e.g., Anderson-Fontana et al. 1986) and Galapagos (e.g., Lonsdale 1988) microplates in the Pacific. It is not difficult to prove that two simple equations allow to express the number of plates $p$ as a function of the number of plate boundaries, $b$, and triple junctions, $j$.

They are:

$$\begin{cases} b = 3\,(p-2) \\ j = 2\,(p-2) \end{cases} \tag{2.34}$$

In fact, if we start from a hypothetical Earth with only three plates ($p = 3$), then it is quite evident that we have $b = 3$ and $j = 2$. In order to generate a new plate, we must split an existing one. This operation requires cutting two edges of the plate through the insertion of two new triple junctions and a new edge connecting them. Therefore, for each new plate we add two triple junctions, thereby $j$ is always even. Regarding the number of plate boundaries, although we add only one new edge, the operation of cutting two

**Table 2.1** Order of modern tectonic plates

| Plate | N | Plate | N | Plate | N | Plate | N |
|---|---|---|---|---|---|---|---|
| Pacific | 13 | Nazca | 7 | Philippine | 5 | Scotia | 3 |
| N. America | 10 | Australia | 5 | Arabia | 5 | Anatolia | 3 |
| Eurasia | 9 | India | 5 | Sundaland | 5 | Amurian | 3 |
| Antarctica | 9 | Somalia | 5 | Caribbean | 4 | J. de Fuca | 2 |
| S. America | 8 | Cocos | 5 | Rivera | 3 | Easter | 2 |
| Africa | 7 | Okhotsk | 5 | S. Sandwich | 3 | | |

existing boundaries determines further increase of the total number of plate boundaries by two units. Therefore, there are three additional boundaries for each new plate. This proves Eq. (2.34).

The present day configuration illustrated in Fig. 2.16 includes 23 plates. Thus, Eq. (2.34) requires that $j = 42$ and $b = 63$. The order $N$ of these plates is listed in Table 2.1. The order of a tectonic plate measures the degree of interaction with the global system, because it coincides with the number of neighbor plates. For example, in the modern Earth's configuration the dynamics and kinematics of the Pacific and N. American plates have the largest impact on the global plate system, because they are interacting with 14 of the remaining 21 tectonic plates.

The classification and the kinematics of triple junctions has been the subject of several studies since the 1960s (McKenzie and Morgan 1969; Patriat and Courtillot 1984; Kleinrock and Phipps Morgan 1988). The basic principle describing the instantaneous kinematics of these important tectonic features is represented by the *closure rule*. In general, if $\boldsymbol{\omega}_{AB}$, $\boldsymbol{\omega}_{BC}$, and $\boldsymbol{\omega}_{CA}$ are respectively the Euler vectors of a plate $A$ with respect to another plate $B$, of $B$ with respect to a third plate $C$, and of $C$ relative to $A$, then the closure rule simply states that:

$$\boldsymbol{\omega}_{AB} + \boldsymbol{\omega}_{BC} + \boldsymbol{\omega}_{CA} = \mathbf{0} \tag{2.35}$$

If this three-plates system is connected through a triple junction $J$, then this point belongs simultaneously to $A$, $B$, and $C$. Therefore, applying Eq. (2.17) we have that in this case the closure rule can be expressed in terms of linear velocities at the triple junction:

$$\boldsymbol{v}_{AB} + \boldsymbol{v}_{BC} + \boldsymbol{v}_{CA} = \mathbf{0} \tag{2.36}$$

The velocity triangle associated with Eq. (2.36) can be used to predict the kinematics of triple junctions. The method is illustrated in Fig. 2.17 through four significant examples. It is useful to assume a reference frame fixed to one of the three plates (for example, $A$). Strike-slip boundaries and trenches must be moved according to the magnitude of the relative velocity vectors. However, *trenches are always displaced with the upper (overriding) plate*, thereby they remain at rest when this coincides with the reference plate. An important geological consequence of this behaviour is represented by the development of strike-slip boundaries at triple junctions where a subduction flip occurs (Fig. 2.17 bottom right). This is a general result, which in principle may be observed along any composite flipping convergent boundary between two plates, as illustrated in Fig. 2.18.

Differently from the other plate boundaries, ridges move at half of the relative velocity $v$ between two conjugate plates (Fig. 2.17 top left). In the case of an *RRR* junction, an extra space of triangular shape is created during the displacement of the three spreading segments, with edges given by: $\boldsymbol{v}_{AB}\Delta t$, $\boldsymbol{v}_{BC}\Delta t$, and $\boldsymbol{v}_{CA}\Delta t$. The new triple junction will be placed within this triangle, but the link to the original segments may be somewhat complicated. It may involve either a simple propagation of the spreading segments toward the new location of the triple junction, or the formation of new spreading segments and even of a small microplate, as it is observed in the East Pacific region (Juan Fernandez and Galapagos microplates). The fact that a ridge moves at half velocity with respect to the reference plate clearly implies that any set of points located near a spreading segment at time $t$ will be displaced

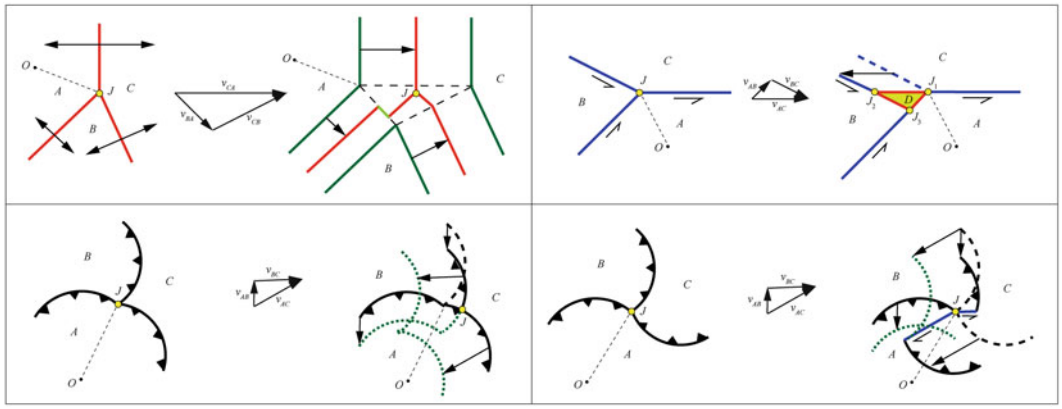

**Fig. 2.17** Evolution of *RRR*, *FFF*, and *TTT* triple junctions. In all panels, a reference frame with origin in *O* is fixed to *A*. *Top left*: An *RRR* junction. *Arrows* are full spreading velocity vectors at the triple junction *J*. The new location of *J* after a small time interval $\Delta t$ can be anywhere in the central *dashed triangle*. The ridges link to this new location of *J* by propagation, development of new transforms, or oblique spreading. *Dark green lines* are points having the same sea floor age (isochrons). *Top right*: An unstable *FFF* triple junction, which collapses into a new triple junction microplate. In this example, three new *RRF* junctions are created that substitute the original junction *J*. *Dashed lines* represent initial locations of plate boundaries. *Bottom*: The two different kinds of *TTT* junctions. *Dotted lines* represent subducted points of lower plate margins. The *left panel* shows a stable situation where *A* is always upper plate, *B* is both upper and lower plate, and *C* is always lower plate. The junction *J* migrates rightward along the *A*−*C* boundary. The *right panel* illustrates a much more complicated configuration, in which *A*, *B*, and *C* are all upper and lower plates at the same time. In this instance, the triple junction is not stable, and new strike-slip boundaries develop (*blue lines*)

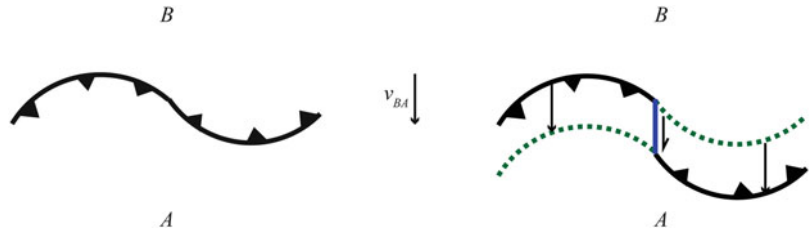


**Fig. 2.18** Development of strike-slip faults along flipping convergent boundaries

away from the ridge, after a time interval $\Delta t$, by a distance $v\Delta t/2$ (Fig. 2.6). If we link all the displaced points of age $t$ from one side of a ridge, and combine these segments with points placed along the fracture zones, we obtain a line that represents the geometry of the mid-ocean ridge at a certain time $t$ in the past. Such a line is called an *isochron*. In Chap. 5, we shall learn the process of construction of *isochron maps*, which describe the pattern of sea-floor spreading through the geological time. For the moment, it is sufficient to note that in the reference frame of a plate *A*, an isochron of the conjugate plate *B* moves at full velocity *v*, just like trenches and strike-slip boundaries, as illustrated in Fig. 2.17.

## 2.6 Tectonic Elements

Computer modelling of plate kinematics has the primary objective of reconstructing sequences of past plate configurations. It requires, at a first step, the specification of the *tectonic elements* that will be included in the reconstructions. On a present day tectonic map, these are defined as *rigid crustal blocks*, bounded by paleo-faults, which have had an independent kinematic history in the geologic past (Ross and Scotese 1988). This quite general definition applies equally well to different scales of modelling (global, regional, or local) and to different structural features, such

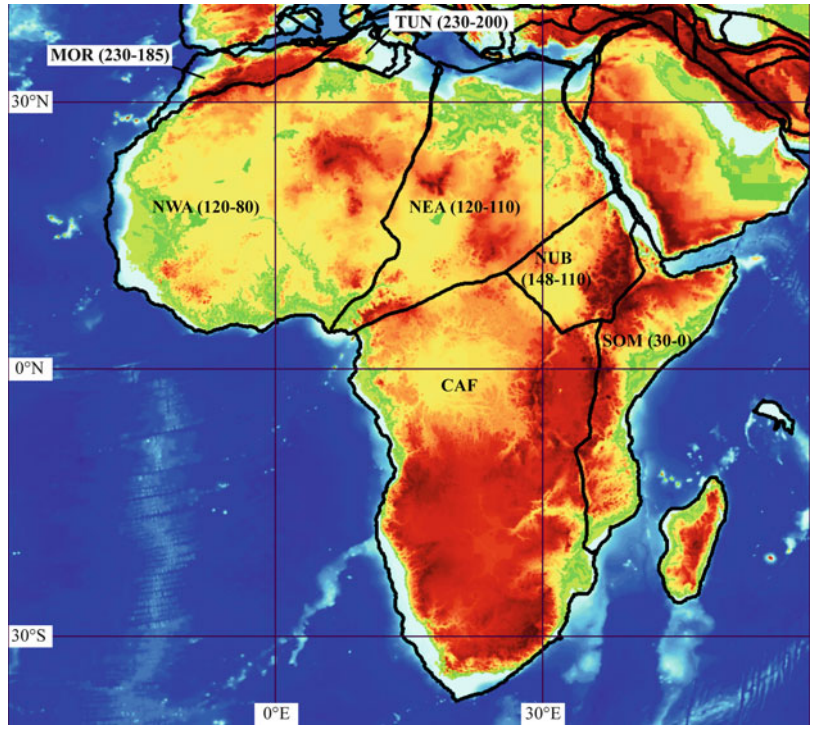


**Fig. 2.19** Major Mesozoic and Cenozoic tectonic elements of Africa. *MOR* Morocco, *NWA* northwest Africa, *CAF* central Africa, *NEA* northeast Africa, *NUB* Nubia, *SOM* Somalia, *TUN* Tunisia. Numbers refer to the temporal range of independent motion

as exotic terranes, thrust sheets, microplates, slivers, continents, blocks of oceanic crust, etc. Usually the boundaries of these tectonic elements are traced using specialized GIS software, such as GlobalMapper™, but some plate tectonic modelling tools allow to draw directly the shape of the crustal blocks as *spherical polygons* (Schettino 1998, 1999a). If we normalize the Earth's radius to unity, then a spherical polygon representing a tectonic element is a cyclic ordered sequence of $n$ unit vectors, $P = \{\boldsymbol{r}_1, \boldsymbol{r}_2 \ldots, \boldsymbol{r}_n\}$, placed along its boundaries. The greater is the number of polygon vertices, $n$, the higher is the detail through which we graphically represent a crustal block. In general, the definition of the tectonic elements is a digitizing procedure, which could also require employing specialized hardware (digitizers) and thematic base maps, such as gravity or magnetic anomaly maps, topography, bathymetry, geologic maps, structural maps, etc. In any case, the tectonic elements have two time attributes that specify the temporal range of activity along their boundaries. These attributes define the time interval of existence of the crustal blocks as independent kinematic entities. For example, Mesozoic plate reconstructions involving Africa require the specification of at least six tectonic elements to account for the deformation of this continent. They are: Morocco, Tunisia, northwest Africa, northeast Africa, central Africa, and Nubia (Fig. 2.19).

Geological field studies performed in Morocco suggest that this block moved with respect to northwest Africa only between ~230 Ma (late Ladinian) and ~185 Ma (Pliensbachian), during the formation of the Atlas Rift (e.g., Laville and Piqué 1991), whereas for the rest of the Mesozoic it remained fixed to northwest Africa (Schettino and Turco 2009). Similarly, northwest Africa moved with respect to central Africa only between ~120 Ma (Aptian) and ~80 Ma (Campanian), during an episode of extension that produced the Benue Trough, a failed arm of the northward propagating South Atlantic rift (e.g., Fairhead 1988). Therefore, it is always necessary, when defining a set of tectonic elements, to start from reliable field data, having strong geochronologic constraints, and use only faults that were active during the time interval under consideration.

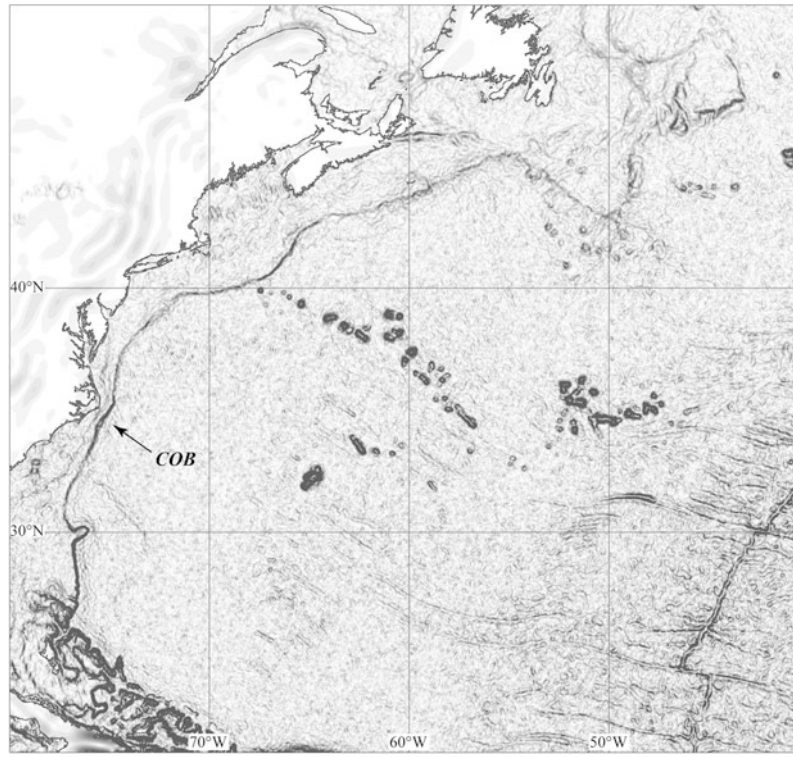


**Fig. 2.20** Eastern North American COB, based on the maximum horizontal gradient of the free-air gravity anomaly field (Sandwell and Smith 1997)

Some tectonic element boundaries are defined on the basis of geophysical constraints. An important example is represented by COBs (see Sect. 1.3). In the first plate reconstructions based on rigorous computational methods, Bullard et al. (1965) matched the conjugate continental margins around the Atlantic on the basis of a fitting algorithm. They applied the method to the 100, 500, 1,000, and 2,000 fm isobaths (1 fathom = 6 ft), then chose the best fitting set of curves (500 fm = 914.4 m) as most representative of the conjugate COBs.

Although this method produced a set of reconstructions that resisted through time and can be considered milestones in the history of plate kinematics modelling, none of the selected isobaths was really representative of the true boundary between continental and oceanic crust. The shape of bathymetry contour lines is strongly affected by the sedimentary cover. For instance, deposits associated with the delta of a great river (such as the Nile or the Ganges) can progressively shift the 1,000 mt isobath seawards by hundreds of kilometers in a few million years. The existence of such processes implies that even though conjugate isobaths may fit well at the beginning of the ocean opening, subsequent sedimentation generally decreases this initial goodness of fit. Therefore, more recent studies have adopted a geophysical definition of the COBs. For example, Schettino and Scotese (2005) assumed that the COBs were associated with the maximum horizontal gradient of the gravity anomaly field. This assumption was based on the observation that marine gravity anomaly maps adequately filter the sediment cover, and that COBs are associated with important lithological discontinuities, which give rise to sharp variations of the gravity anomaly field. In this context, free-air gravity anomaly maps such as those proposed by Sandwell and Smith (1997) represent an invaluable tool for modern plate tectonic modeling. Figure 2.20 shows a map of the horizontal gradient of the gravity anomaly field along the eastern margin of North America. The line of maximum gradient can be easily used to trace the North American COB.

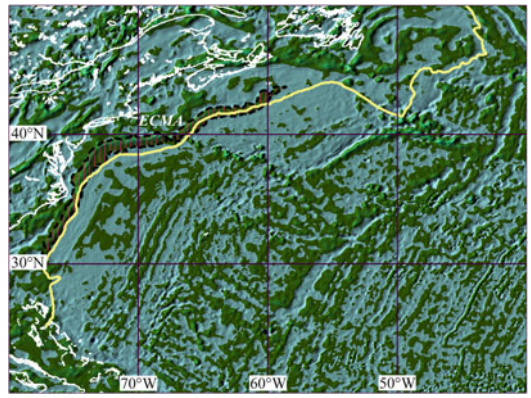


**Fig. 2.21** Pattern of magnetic anomalies along the eastern North American margin and in the western central Atlantic, extracted from the global data set of Korhonen et al. (2007). Positive anomalies are shown in *dark green*. The location of the ECMA (*vertical hatch*) marks a zone of transitional crust (or anomalous oceanic crust) along the volcanic margin. The *yellow line* shows the location of the COB according to the gravity data of Fig. 2.20 (maximum horizontal gradient of the gravity anomalies)

Another class of geophysical markers that are useful to identify COBs is represented by the magnetic anomalies that border volcanic OCTs (see Sect. 1.3). A classic example is represented by the East Coast Magnetic Anomaly (ECMA) of eastern North America (e.g., Schettino and Turco 2009). In this instance, a strong linear magnetic anomaly associated with the extrusives and intrusives of the initial magmatic pulse marks the site of transition from the rifting stage to drifting, hence the location of the COB, as illustrated in the example of Fig. 2.21. However, a comparison between the location (and the geometry) of the ECMA and the COB defined on the basis of gravity anomaly data (Fig. 2.20) shows that the coincidence of these features is only approximate, and that differences of up to 70–80 km exist between the two lineaments. Therefore, even when based on a geophysical approach, the definition of COBs remains to some extent qualitative.

A major problem in the definition of both COBs and tectonic boundaries that are placed along rift zones is represented by the considerable thinning that characterizes the passive margins of the corresponding tectonic elements. If we use one of the geophysical techniques described above to define a conjugate pair of COBs, then a reconstruction based on the fit of the margins will be representative of the onset of sea floor spreading, not of the pre-rift configuration. In fact, tectonic elements whose extensional boundaries are defined using potential field data (either gravity or magnetic data) are *stretched* elements, which should be restored to their original size when the objective is to make a pre-rift reconstruction. There are three approaches to the solution of this problem, which clearly does not affect the reconstruction of the spreading history of oceanic basins. All these methods require an estimation of the amount of stretching that occurred during the rifting stage. This is usually expressed in terms of stretching factor $\beta$ (see Sect. 2.4). A determination of this quantity can be made when a set of crustal profiles along the continental margins, obtained from seismic refraction experiments, is available (e.g., Schettino and Turco 2009). The first step consists into an estimation of the directions of stretching, for example by landward prolongation of the first post-rift directions of sea floor spreading. We shall see that these directions can be easily calculated on the basis of a kinematic model. Then, the seismic cross-sections are projected onto the directions of stretching, to avoid an incorrect determination of the continental margin width. At the next step, the upper and lower boundaries of the stretched crust, the latter coinciding obviously with the Moho, are identified on the cross-sections. Assuming that seismic profiles always start on unstretched crust, then these boundaries are two functions,

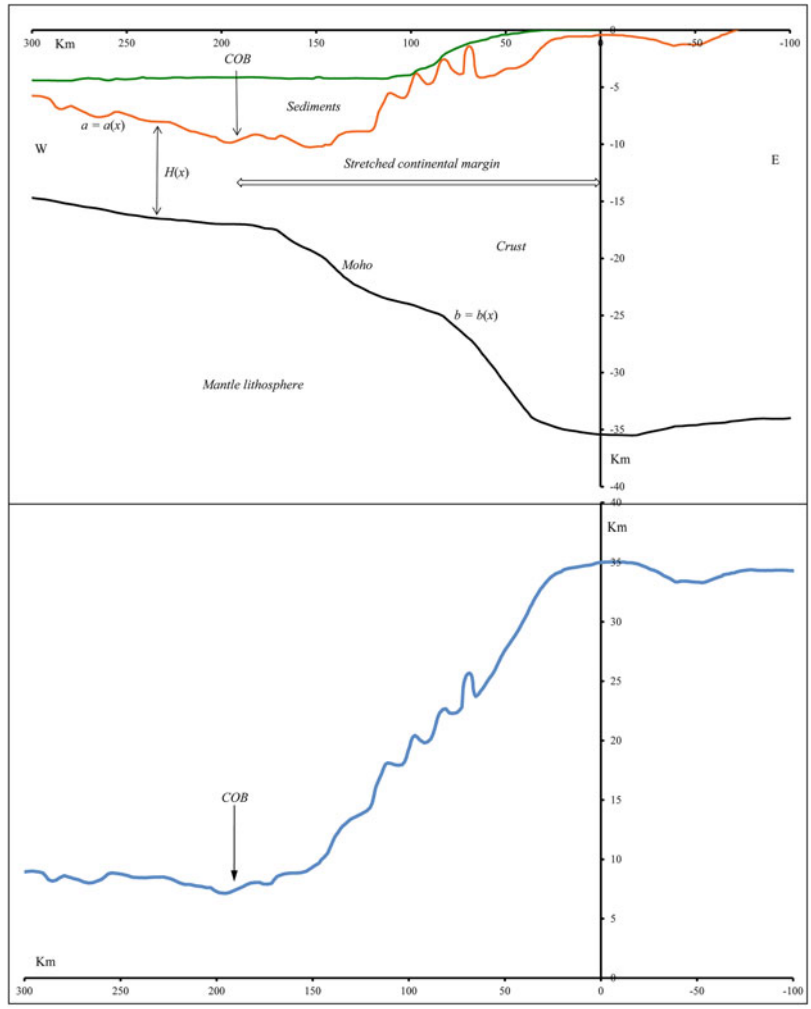


**Fig. 2.22** Seismic refraction profile SIS-04, offshore Morocco (Contrucci et al. 2004), projected onto the direction of Triassic-Jurassic rifting (*top*). The *green line* represents the bathymetric surface. The *bottom panel* shows a plot of the crustal thickness (excluding sediments), $H(x) = a(x) - b(x)$, along the margin. The stretched continental margin as width $L \cong 193$ km. If we restore the thickness to $H_0 = 35$ km, the width of the margin is reduced to $L_0 \cong 110$ km (pre-rift width). Therefore, the stretching factor β is given by: $\beta = L/L_0 \cong 1.75$

say $a = a(x)$ and $b = b(x)$, of seaward increasing offsets $x$ along the profile. The example illustrated in Fig. 2.22 shows the seismic profile SIS-04, located offshore Morocco (Contrucci et al. 2004), after projection onto the direction of Triassic-Jurassic rifting (Schettino and Turco 2009). If $L$ is the size of the stretched margin (for example determined by the COB) and $H_0$ is the normal unstretched crustal thickness, then the pre-rift restored size, $L_0$, and the stretching factor, β, will be given by (Fig. 2.22):

$$L_0 = \frac{1}{H_0}\int_0^L [a(x) - b(x)]\,dx \equiv \frac{1}{H_0}\int_0^L H(x)dx \tag{2.37}$$

$$\beta = L/L_0 = \frac{LH_0}{\int_0^L H(x)dx} \tag{2.38}$$

As soon as the stretching factor β has been estimated, there are three possibilities for taking into account thinning of passive margins during the syn-rift stage in pre-rift reconstructions. In a first method, the tectonic elements are defined through their present day stretched boundaries, but a pre-rift reconstruction will require an overlap of the stretched margins, as illustrated in Fig. 2.23. This method works well both in the case of passive margins of oceans and for failed

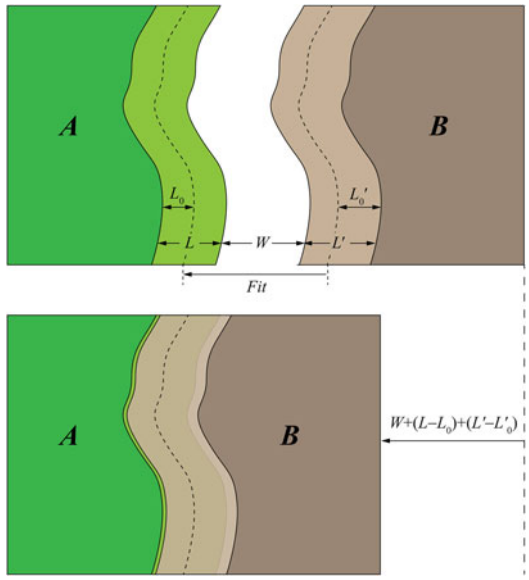


**Fig. 2.23** Overlap of the stretched continental margins in absence of palinspastic restoration. Let $W$ be the width of the oceanic domain. In a pre-rift reconstruction, plate $B$ is displaced by $W + (L–L_0) + (L'–L'_0)$ with respect to the reference plate $A$, because the unstretched margins (*dashed lines*) must be matched. Therefore, the stretched continental margins will overlap by a quantity $F = (L–L_0) + (L'–L'_0)$

rifts. The amount of overlap is locally defined by the quantity:

$$\begin{aligned} F &= (L - L_0) + \left(L' - L'_0\right) \\ &= L_0\,(\beta - 1) + L'_0\left(\beta' - 1\right) \end{aligned} \tag{2.39}$$

where the quantities $L'$, $L'_0$, and $\beta'$ refer to the conjugate plate. A second possibility requires a preliminary restoration of the tectonic elements to their unstretched shape through a process that geologists call *palinspastic restoration* (e.g., Schmid et al. 1996; Schmid and Kissling 2000; Schettino and Turco 2006). In this instance, the boundaries of conjugate tectonic elements will match in pre-rift reconstructions, but a reconstruction at the time of rift-drift transition will show a gap. Finally, a third approach could be releasing the constraint of rigid tectonic elements and allow stretching (or shortening) of the crustal blocks along the directions of relative motion. A modern computer program for making plate reconstructions should allow usage of this method, which is particularly attractive in the case of small-scale reconstructions of collisional settings and represents a link between the classic approach of rigid plate kinematics, mostly suitable for describing the evolution of oceanic basins, and structural geology. In this approach, the amount of deformation (i.e. *strain*) of the tectonic elements should be specified directly in the kinematic model, and the shape of any crustal block included in the compilation of tectonic elements would be defined by the present day stretched or shortened margins, so that it would not be necessary anymore to perform manually a palinspastic restoration. In this instance, the procedure of restoration would be accomplished automatically by the software with the correct timing.

## 2.7 Plate Circuits and Rotation Models

Now we will consider the problem of representing the motion of a set of tectonic elements through the geological time. The kinematics of a set of tectonic plates can be described by generating a sequence of *plate reconstructions*, eventually combined into a computer animation. In this representation, the temporal range of the reconstructions is always subdivided into a series of *tectonic stages*, time intervals during which the relative motions can be described as rotations about fixed Euler axes at constant angular velocities. The existence of such time intervals, which may span several million years, is probably the most fundamental principle of plate kinematics. During a stage, it is possible to determine a set of plate pairs ($A$,$B$), sharing common boundaries, such that the motion of $B$ with respect to $A$, considered at rest in the present day position, can be represented as a rotation about a fixed Euler axis at constant angular velocity $\omega$. In this instance, the relative motion between any plate pair in the set occurs, within each stage, along flow lines that are small circle arcs about an Euler axis. The experimental evidence of this fundamental principle relies on the analysis of

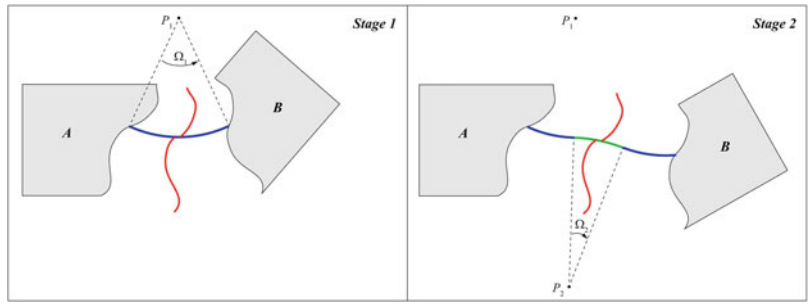


**Fig. 2.24** Geometry of fracture zones. In a reference frame fixed to $A$, plate $B$ rotates counterclockwise about pole $P_1$ by an angle $\Omega_1$ (stage 1). The resulting fracture zone has the shape of a small circle arc about $P_1$ (*blue line*). The subsequent clockwise rotation about pole $P_2$ during stage 2 separates the fracture zone in two arms and inserts a new small circle about $P_2$ in the central zone (*green line*)

marine magnetic anomalies and the observation that the trace of oceanic fracture zones can be invariably decomposed into chains of small circle arcs. However, we shall prove that it has a more general validity. Furthermore, this principle puts strong constraints on the equilibrium of the driving forces of plate tectonics, thus representing a conceptual linkage between plate kinematics and geodynamics.

The sketch of Fig. 2.24 illustrates the process through which a fracture zone assumes the distinctive shape of a chain of small circles. On the basis of the fundamental principle stated above, if $(T_0,T_2,\ldots,T_n)$ are stage boundaries, $T_0 < T_1 < \ldots < T_n$, then there exist *n stage poles* $P_1,P_2,\ldots,P_n$ such that the relative displacement of a plate $B$ during the $k$−th stage can be represented by a finite rotation matrix $\boldsymbol{S}_{BA}(T_{k-1},T_k)$ about the axis $\boldsymbol{n}_k$ associated with the $k$−th Euler pole $P_k$ (Eq. 2.18). This rotation, which moves $B$ from the location at time $T_{k-1}$ to the position occupied at time $T_k$, is called a *stage rotation*. It can be represented either by matrix components (Eq. 2.18) or as a triplet $(\lambda_k,\phi_k,\Omega_k)$, where $(\lambda_k,\phi_k)$ are the geographic coordinates of a stage pole $P_k$ and $\Omega_k$ is the finite angle of rotation during that stage (Fig. 2.24). Clearly, if a set of forward transformations $\boldsymbol{S}_{BA}(T_{k-1},T_k)$ has been established, we can also move back through time and determine the relative position of $B$ at time $T_{k-1}$ given the position at time $T_k$. This operation simply requires application of the inverse transformation:

$$\boldsymbol{S}_{BA}\,(T_k, T_{k-1}) = \boldsymbol{S}_{BA}^{-1}\,(T_{k-1}, T_k) \qquad (2.40)$$

If $T_{k-1} \le T \le T_k$ is an intermediate time during the $k$−th stage, then the relative position of $B$ at time $T$ can be determined by taking as rotation angle the reduced angle $\Omega(T)$:

$$\Omega(T) = \frac{T - T_{k-1}}{T_k - T_{k-1}}\Omega_k \qquad (2.41)$$

Now let us consider the central point of a transform fault that belongs to a present day or extinct mid-ocean ridge. Let $\boldsymbol{r}_0$ be the position vector of this point. We are looking for an algorithm that simulates the geometry of the fracture zone passing through $\boldsymbol{r}_0$. The task should be accomplished calculating iteratively the location of this point, relative to each of the conjugate plates $A$ and $B$, at any time $T \in [T_0,T_n]$, where $T_0$ and $T_n$ are respectively the time of onset of sea floor spreading and the present day (or the time of extinction). In this algorithm, it is necessary to take into account that for any stage the point moves by half of the full stage angle $\Omega_k$ on each of the conjugate plates. Therefore, the point must be rotated using *reduced* backward stage pole matrices, $\boldsymbol{S}^*_{BA}(T_k, T_{k-1})$ and $\boldsymbol{S}^*_{AB}(T_k, T_{k-1})$, having the same stage pole locations of $\boldsymbol{S}_{BA}(T_k, T_{k-1})$ and $\boldsymbol{S}_{AB}(T_k, T_{k-1})$, respectively, but halved stage angles. If $T_{k-1} \le T \le T_k$, then the location of $\boldsymbol{r}_0$ at time $T$ on plate $A$, $\boldsymbol{r}_A(T)$, will be given by:

$$\begin{aligned}\boldsymbol{r}_A(T) = {} & \boldsymbol{S}^*_{BA}\,(T_k, T)\ldots\boldsymbol{S}^*_{BA}\,(T_{n-1}, T_{n-2}) \\ & \times \boldsymbol{S}^*_{BA}\,(T_n, T_{n-1})\,\boldsymbol{r}_0\end{aligned} \qquad (2.42)$$

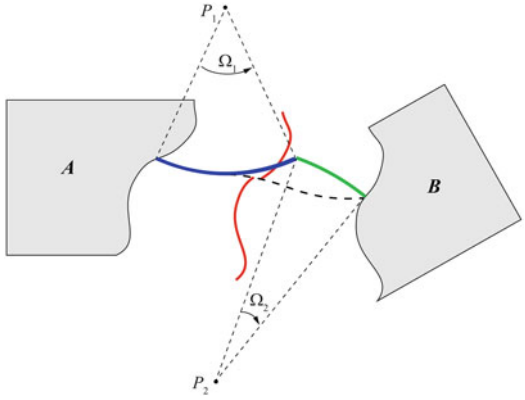


**Fig. 2.25** Construction of flow lines. The sequence of stage rotations is the same of Fig. 2.24, and the *dashed line* shows the corresponding fracture zone

A similar formula allows to calculate the location of $\boldsymbol{r}_0$ at time $T$ on plate $B$, $\boldsymbol{r}_B(T)$. This algorithm can be used to test the compatibility of existing kinematic models with real fracture zones trend. In fact, the chain of rotations included in Eq. (2.42) implies that even small errors on the single stage rotations are enhanced after few matrix multiplications. The algorithm, which should reproduce the geometry of any fracture zone, was applied for the first time by Shaw (1987) in a study on the South Atlantic plate motions. More recently, Schettino and Turco (2009) used this method to give further evidence that an independent Moroccan plate existed in the central Atlantic during the Oligocene and early Miocene. Equation 2.42 allows to predict the geometry of fracture zones given a plate motions model, that is, given a sequence of stage rotations. These lines must not be confused with the *flow lines* of relative motions, which display the path of a representative point on a plate $B$ relative to a reference plate $A$. Figure 2.25 illustrates the process of constructions of flow lines and the difference with fracture zones. Although flow lines can be traced for both oceanic basins and zones of convergence, the latter tectonic context historically represents the principal field of application of this kind of kinematic representation (Dewey et al. 1989; Schettino and Turco 2011). Generally, the algorithm for generating flow lines is simple in the case of oceanic basins and follows the approach used for the modelling of fracture zones (Eq. 2.42). The method is illustrated in Fig. 2.25. In this example, a point that is currently placed along the COB of one of the two plates, say $B$, is moved backward through time to the locations occupied at any time $T \in [T_0,T_n]$ with respect to the conjugate reference plate $A$.

In this instance, however, the stage rotations are performed using the full stage angles $\Omega_k$ and not, as we saw in the case of fracture zones, the halved angles. If $\boldsymbol{r}_0$ is the position vector of a starting location along the continental margin of $B$, then the location at time $T$, $T_{k-1} \leq T \leq T_k$, is a vector $\boldsymbol{r}(T)$ given by:

$$\boldsymbol{r}(T) = \boldsymbol{S}_{BA}(T_k, T) \ldots \boldsymbol{S}_{BA}(T_{n-1}, T_{n-2}) \times \boldsymbol{S}_{BA}(T_n, T_{n-1})\, \boldsymbol{r}_0 \tag{2.43}$$

This method can be used for some, but *not* for *all*, pairs of oceanic plates. Furthermore, it is not generally applicable to the case of convergent settings. The reason is that stage rotations exist for some plate pairs sharing a common boundary, but not for *any* pair of plates, not even when they share a boundary. This theorem can be easily proved considering the simple case of a three-plates system. Let us consider an *RRR* triple junction like that of Fig. 2.17. If the relative motion of $B$ with respect to $A$ is described by a stage rotation, then by definition the Euler pole $P_{BA}$ is at rest in the reference frame of $A$. Similarly, if the motion of $C$ with respect to $A$ can be described by a stage rotation, then the location of the stage pole $P_{CA}$ is also at rest in the reference frame of $A$. However, $P_{BA}$ will not be at rest with respect to $C$, just like $P_{CA}$ will not be at rest with respect to $B$. Therefore, the Euler vector $\boldsymbol{\omega}_{BC} = \boldsymbol{\omega}_{BA} + \boldsymbol{\omega}_{AC}$ cannot be an invariant neither in the frame of $B$ nor in that of $C$. This implies that a stage pole does not exist for the plate pair ($B$,$C$), even though both $B$ and $C$ move by stage rotations with respect to $A$. For this reason, we shall use the term "conjugate plates" only in the case of plates sharing a common boundary (not necessarily a spreading ridge) and whose relative motion can be described by a sequence of stage rotations. When the divergent relative motion between two

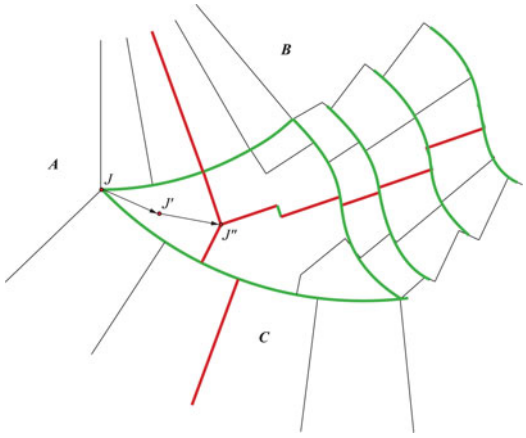


**Fig. 2.26** Fracture zones pattern and triple junction migration path for a system of three divergent plates. Plates *B* and *C* move about fixed Euler axes at constant rate with respect to *A*. The relative motion between *B* and *C* cannot be represented by a stage rotation

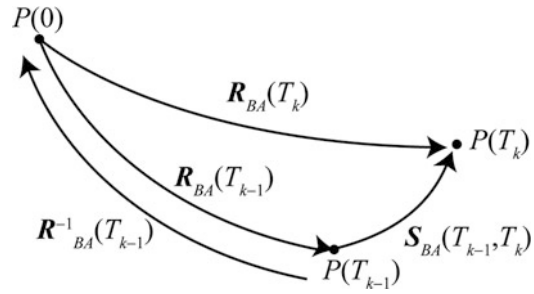


**Fig. 2.27** Relationship between stage rotations and finite reconstructions. To move a point *P* from the location at time $T_{k-1}$ to that at time $T_k$, it is possible to go first to the present day through an inverse finite reconstruction, then to time $T_k$ through a direct finite transformation

plates does not occur about a fixed rotation axis, the fracture zones assume the complicate shape shown in Fig. 2.26 between *B* and *C*.

Let us consider now the problem of determining stage rotations for a pair of conjugate plates *A* and *B*. In the case of oceanic basins, a subdivision of the opening history in tectonic stages is performed on the basis of the geometry of fracture zones and an analysis of marine magnetic anomalies. This procedure will be explained in detail in Chap. 5. It allows to determine both the stage boundaries ($T_0$,$T_2$,...,$T_n$) and the relative position of *B* with respect to *A* (considered at rest in the present day position) at each time $T_k$ ($k = 1,2,\ldots,n$). Regarding the relative position at time $T_0$, it can determined through a fitting algorithm applied to the conjugate COBs, as we shall see in the next section. All these relative positions are specified through *finite reconstruction* matrices $\boldsymbol{R}_{BA}(T_k)$, whose expression is given by (2.18). The existence of these transformations is ensured by Euler's theorem (see Sect. 2.2). Generally, the components of the versor $\boldsymbol{n}(T_k)$, associated with the rotation axis at time $T_k$, are expressed in terms of geographic coordinates ($\lambda(T_k)$,$\phi(T_k)$) of a *finite reconstruction pole* $P_k$. In this instance, the triplet ($\lambda(T_k)$,$\phi(T_k)$,$\Omega(T_k)$), $\Omega(T_k)$ being the rotation angle, specifies all the necessary parameters to perform the transformation of a tectonic element from the present day location to the position at time $T_k$ relative to the conjugate plate. Once the finite reconstruction matrices associated with each stage boundary have been determined, it is easy to calculate the corresponding stage rotations by the following formula, whose graphical proof is shown in Fig. 2.27:

$$\boldsymbol{S}_{BA}(T_{k-1},T_k) = \boldsymbol{R}_{BA}(T_k)\,\boldsymbol{R}^{-1}_{AB}(T_{k-1}); \quad k = 1,2\ldots,n \tag{2.44}$$

When considering finite reconstructions, it is always necessary to keep in mind that they do not represent real plate motions, but the combined result of many instantaneous or stage rotations. Therefore, the small circle arcs associated with a finite reconstruction pole are never expressions of existing geological structures, contrarily to the case of stage and instantaneous Euler poles. This is a key point for the correct interpretation of kinematic data, which has been discussed in depth in a seminal paper by John Dewey (1975).

Now we are ready to consider the process of construction of a *rotation model*, which represents the primary data structure that is used in plate tectonic modelling to store the relevant kinematic information. In fact, this file contains the information that is needed to reconstruct both the plate motions and the tectonic history of a region during a selected time interval. Rotation models are tables, generally stored in ASCII

files, used by dedicated algorithms during the process of construction of some hierarchical data structures (or *trees* in the sense of Computer Science, see Appendix 2) that describe the relative positions of a set of tectonic plates at any given time. A *rotation tree* can be considered as a data structure that specifies the multilevel tectonic hierarchy of a plate system at an assigned time $T$ (Ross and Scotese 1988). It is often referred to as a *plate circuit*, although this term is also used when relative velocities are specified rather than relative positions, usually in studies on current plate motions. The nodes of these data structures are tectonic elements, while an edge between any pair of nodes indicates that their relative motion can be described by a sequence of stage rotations. Therefore, given a stage $S$, the edges of a plate circuit $C$ for time $T \in S$ define a set of *conjugate plate boundaries* in a system of interacting tectonic elements during the stage $S$, not the whole set of active plate boundaries, although all the existing plates at time $T$ are represented in $C$. Thus, if $e$ and $p$ are respectively the size (that is, the number of edges) and the order (number of plates) of $C$, then by (2.34) it always results: $e < 3(p-2)$. It is also important to note that the topology of plate circuits is not constant through time, but changes as a consequence of major plate boundary reorganizations. In general, the definition of a plate circuit topology for each tectonic stage is based on the geological or geophysical evidence and the identification of a set of conjugate boundaries, such that the resulting graph is a connected tree (that is, for any two nodes $u$ and $v$ there exists a unique path from $u$ to $v$). The topology is specified implicitly during the compilation of a rotation model, while the duty of the reconstruction algorithms is to build a rotation tree for any assigned reconstruction time $T$.

In the example of Fig. 2.28, we assume that the relative motion between the plate pairs $(A,C)$, $(B,C)$, $(C,D)$, and $(D,E)$ is represented by rotations at constant angular velocity during a time interval $S \equiv [T',T'']$. Therefore, $S$ is assumed to be a tectonic stage. This assumption most likely relies on the geometry of fracture zones in the oceanic area and on geological field

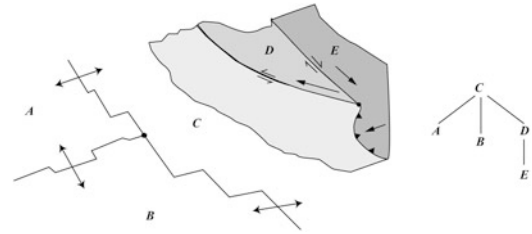


**Fig. 2.28** Sketch map illustrating the construction of plate circuits. *Left*: A system of five plates. Finite rotations of $A$ with respect to $C$, $B$ to $C$, $D$ to $C$, and $E$ to $D$ are known. *Right*: The corresponding plate circuit

evidence regarding the tectonic activity along the transcurrent faults that separate $D$ from $C$ and $E$. In this instance, four finite reconstruction matrices must be defined for the conjugate boundaries, which allow to determine four independent stage rotations, $\boldsymbol{S}_{AC}(T',T'')$, $\boldsymbol{S}_{BC}(T',T'')$, $\boldsymbol{S}_{DC}(T',T'')$, and $\boldsymbol{S}_{ED}(T',T'')$ through Eq. (2.44). If $\boldsymbol{R}_{AC}(T)$, $\boldsymbol{R}_{BC}(T)$, $\boldsymbol{R}_{DC}(T)$, and $\boldsymbol{R}_{ED}(T)$ are the finite reconstruction matrices at any time $T \in [T',T'']$, then any other relative position at time $T$ can be calculated by combining these basic rotations.

For example, it is possible to determine the relative position of $A$ with respect to $B$ and that of $E$ with respect to $C$ at time $T$:

$$\begin{aligned}\boldsymbol{R}_{AB}(T) &= \boldsymbol{R}_{CB}(T)\boldsymbol{R}_{AC}(T);\ \boldsymbol{R}_{EC}(T) \\ &= \boldsymbol{R}_{DC}(T)\boldsymbol{R}_{ED}(T)\end{aligned}$$

In general, the tree structures associated with plate circuits are arranged so that the greater is the degree of a node in a plate circuit $C$, that is, the number of edges incident with the node, the higher will be its level in the hierarchical structure. Therefore, the neighborhoods of nodes in $C$ will increase in size when we move toward higher levels in the data structure.

Plate circuits are built by reconstruction algorithms starting from a rotation model. This table specifies, for any stage boundary, the finite reconstruction pole and rotation angle of each identified pair of conjugate plates. A sample fragment of these data structures is shown in Fig. 2.29. In these tables, the tectonic elements

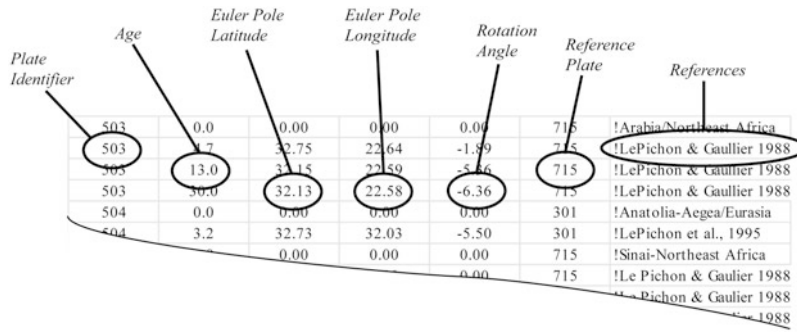


**Fig. 2.29** A fragment of rotation model

are coded through plate identifiers. In order to determine which of the two plates in a conjugate pair must be considered as the reference plate, we shall conform to the principle that high-degree nodes always appear at higher levels in the hierarchical structure. Regarding the definition of the stage boundaries, it is necessary to distinguish between the large first-order plates, in a context of global tectonics, and the case of small tectonic elements associated with intra-plate deformation or collisional settings. A key observation is that the changes of relative motion between large plates during the Mesozoic and the Cenozoic, hence presumably also during earlier time intervals, seem to have occurred synchronously on a global scale, thereby the major stage boundaries coincide. As an example, the classic plate motions model of Müller et al. (1997) is based on 15 synchronous stages from the early Jurassic to the present. This implies that the motions of the major tectonic plates cannot be determined *exclusively* by processes occurring in the mantle, including the subduction of slabs, and independently from each other. Therefore, at any time Earth's tectonic plates must be considered as a system of interacting bodies. Conversely, stage boundaries associated with changes of stage poles between small plates and other tectonic elements must be established on a geological basis and are not necessarily synchronous with major events of reorganization of the plate boundaries. In the next section, we shall discuss some important details of the procedures followed in plate kinematics for the construction of plate motions models.

## 2.8 Plate Tectonic Reconstructions

Usually plate motions models include a reconstruction of the initial configuration, preceding the development of plate boundaries. Figure 2.30 illustrates an example of fit of Pangaea, the large supercontinent that existed before the opening of the Atlantic ocean.

In the previous sections, we have learnt that there are two kinds of initial fits: pre-rift fits, which show the configuration of the continental masses preceding the development of plate boundaries, and post-rift fits, which match the stretched continental margins and show the configuration at the onset of sea floor spreading. In both cases, the match between the conjugate COBs is performed through a geometrical fitting procedure. The algorithm used by Bullard et al. (1965) in their reconstructions of Pangaea was the first rigorous method for fitting continental margins. Here we shall discuss an improved version of this algorithm, which was proposed by Schettino and Turco (2009). Let us assume that the COBs to be fitted are represented by two series of unit vectors, respectively $(\boldsymbol{p}_1,\boldsymbol{p}_2,\ldots,\boldsymbol{p}_N)$ and $(\boldsymbol{q}_1,\boldsymbol{q}_2,\ldots,\boldsymbol{q}_M)$, which have been preliminarily rotated to a geographic reference frame where a test Euler pole $\boldsymbol{e}$, with coordinates $(\lambda_e,\phi_e)$, has been moved to the North Pole (Fig. 2.31). A transformation of the standard geographic coordinates to this new reference frame is obtained by rotating each position vector $\boldsymbol{p}_i$ and $\boldsymbol{q}_j$ about an Equatorial pole placed at $(0°,\phi_e+90°)$ by

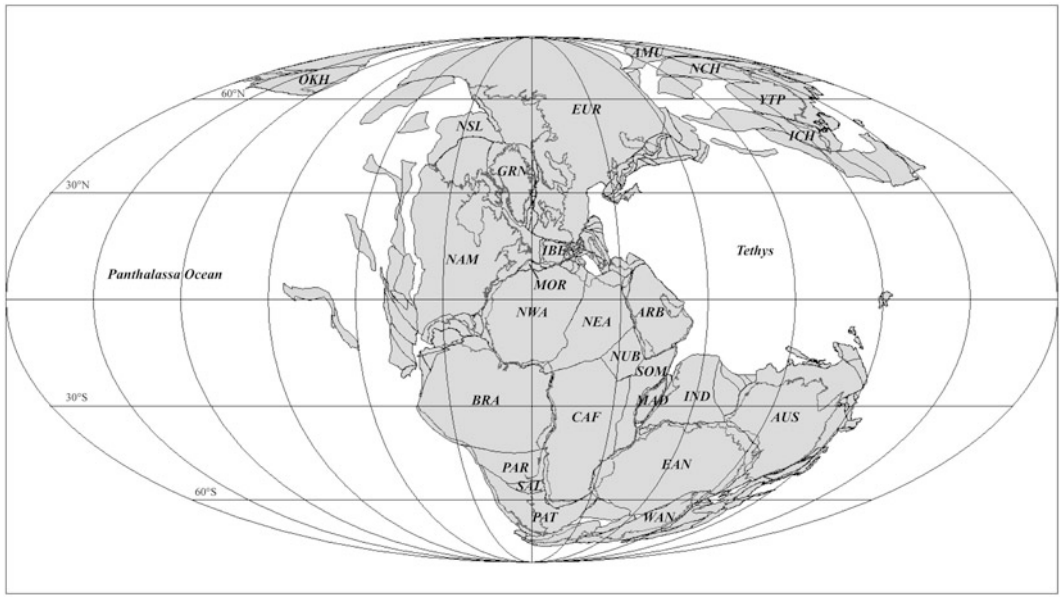


**Fig. 2.30** A pre-rift fit of Pangaea, based on Schettino and Scotese (2005) and Schettino and Turco (2009). The present day coastlines are shown for reference. The major tectonic elements in this reconstruction are: central Africa (*CAF*), northwest Africa (*NWA*), northeast Africa (*NEA*), Nubia (*NUB*), Somalia (*SOM*), Madagascar (*MAD*), Morocco (*MOR*), Arabia (*ARB*), India (*IND*), E. Antarctica (*EAN*), Australia (*AUS*), W. Antarctica (*WAN*), Brazilian Craton (*BRA*), Paraná (*PAR*), Salado Block (*SAL*), Patagonia (*PAT*), N. America (*NAM*), Greenland (*GRN*), North Slope (*NSL*), Okhotsk (*OKH*), Eurasia (*EUR*), Iberia (*IBE*), Amurian Plate (*AMU*), N. China (*NCH*), Yang Tze Platform (*YTP*), and Indochina (*ICH*)

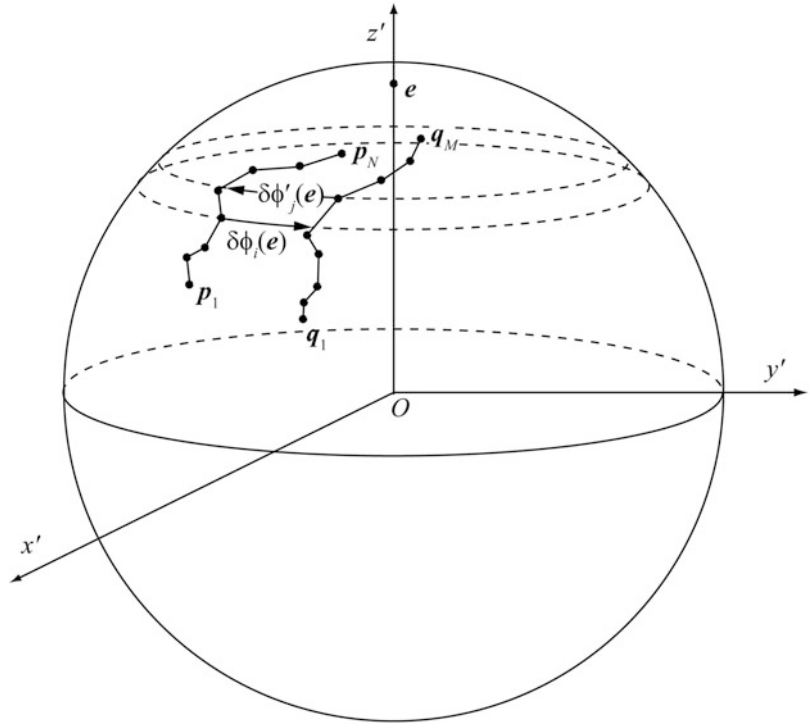


**Fig. 2.31** Geometrical fit of conjugate COBs. In a reference frame ($x'$,$y'$,$z'$) where a test Euler pole, $\boldsymbol{e}$, has been moved to the North Pole, the fitting procedure consists to find the best rotation about the North Pole, by an angle $\Omega$ that minimizes the squared sum of longitude misfits $\delta\phi_i$ ($i \leq N$) and $\delta\phi'_j$ ($j \leq M$)

an angle $-\theta_e = -(\pi/2 - \lambda_e)$. For each point $\boldsymbol{p}_i$ on the first line, which can be carried onto the second line at position $\boldsymbol{p}_i'$ by rotation about the North Pole, let $\delta\phi_i(\boldsymbol{e})$ be the longitude difference between the two locations. Similarly, for each point $\boldsymbol{q}_j$ on the second line, which can be carried back onto the first one at position $\boldsymbol{q}_j'$ by rotation about the North Pole, let $\delta\phi_j'(\boldsymbol{e})$ be the longitude difference. In general, only $n \leq N$ points of the first line can be projected onto the second line, and only $m \leq M$ points of the second line can be projected back onto the first line. If we rotate the western line by an angle $\Omega$ about the North Pole, then misfit between a rotated vertex and its projection along the eastern line is given by $\delta\phi_i(\boldsymbol{e}) - \phi_0$. Similarly, if we rotate the eastern line by angle $-\Omega$ about the North Pole, we obtain individual misfits $\delta\phi'_j(\boldsymbol{e}) - \Omega$. The total mean-square misfit will be given by:

$$\chi^2(\boldsymbol{e}) = \frac{N}{n^2}\sum_{i=1}^{n}(\delta\phi_i(\boldsymbol{e}) - \Omega)^2 + \frac{M}{m^2}\sum_{j=1}^{m}\left(\delta\phi'_j(\boldsymbol{e}) - \Omega\right)^2 \quad (2.45)$$

This formula shows some differences with respect to the one used by Bullard et al. (1965). In fact, the original formula of these authors assumed that the same number of points was projected between the two lines. This assumption is adequate only when the two COBs may match perfectly, that is, when each line can be fit against the whole conjugate line and not against a subset of the input data. For example, we could have missing information from one of the two conjugate COBs. In this instance, we must search for a best fit of one line against a *subset* of the second line, not necessarily a whole geometrical fit. Eq. (2.45) takes into account of the possibility that one the two lines is not complete. In these conditions, the best fit Euler pole searching algorithm also tries to maximize the percentage of matched segments from each line, that is, the number of projected points, because we could find wrong Euler poles that furnish very good fits of small segments of the two lines. This problem is solved in Eq. (2.45) by multiplying the squared misfit of each line respectively by $N/n$ and $M/m$. This expression reaches a minimum when the rotation angle $\Omega = \Omega(\boldsymbol{e})$ is given by:

$$\Omega(\boldsymbol{e}) = \frac{\frac{N}{n^2}\sum_{i=1}^{n}\delta\phi_i(\boldsymbol{e}) + \frac{M}{m^2}\sum_{j=1}^{m}\delta\phi'_j(\boldsymbol{e})}{\frac{N}{n} + \frac{M}{m}} \quad (2.46)$$

The fitting procedure is a searching algorithm of the Euler pole $\boldsymbol{e}$ which minimizes the misfit $\chi^2$ in expression (2.45). The search is generally based on trial Euler poles that are chosen over a coarse grid of locations (for example, a $1 \times 1°$ global grid). For each trial pole $\boldsymbol{e}$, the angle $\Omega$ that minimizes $\chi^2$ is determined through Eq. (2.46). A first approximate location of the Euler pole is obtained by selecting the trial pole that gives the minimum value of $\Omega$ over the global grid. Now a new scan is performed over a neighbor of this point using a reduced grid spacing, for example 0.1°, so that a new more precise location of the Euler pole and a new angle of rotation are determined. The algorithm stops when the desired resolution is reached.

Now let us consider the procedure for reconstructing the position of a tectonic element at time $T$ in the geologic past, starting from a corresponding plate circuit $C(T)$. This reconstruction algorithm has the following simple structure:

**Algorithm 2.2 (Reconstruction Algorithm)**
Input: a node $n \in C(T)$;
Output: A total reconstruction matrix $\boldsymbol{R}_n(T)$;
{

1. $\boldsymbol{R}_n(T) \leftarrow \boldsymbol{I}$; $c \leftarrow n$;
2. $p \leftarrow Parent(c)$;
3. $p = 0 \Rightarrow$ jump #7;
4. $\boldsymbol{R}_n(T) \leftarrow \boldsymbol{R}_{cp}(T)\boldsymbol{R}_n(T)$;
5. $c \leftarrow p$;
6. Jump #2;
7. $\boldsymbol{R}_n(T) \leftarrow \boldsymbol{R}_c(T)\boldsymbol{R}_n(T)$;

}

A *total reconstruction matrix*, $\boldsymbol{R}_n(T)$, is a matrix that moves a tectonic element $n$ from its present day location, in the geographic reference

frame, to the position that this block had at time $T$ *in a paleotectonic reference frame*. An important example of this class of frames is represented by the paleomagnetic frames mentioned in Sect. 2.3, but one could wish to refer the reconstructions to a set of hot spots (e.g., Müller et al. 1993) or even use a present day continent, for example N. America or Eurasia, as a reference frame for plate reconstructions. The existence of total reconstruction matrices is again a consequence of Euler's theorem. The corresponding Euler pole is called a *total reconstruction pole*. At step #1 of Algorithm 2.1, the total reconstruction matrix is initialized by the identity matrix $\boldsymbol{I}$, and the current node, $c$, is set to be the starting node. At step #2, a variable $p$ is assigned the parent of the current node in the tree structure. At the next step, if the current node $c$ coincides with the root of the tree, so that $p = 0$, then the iteration stops and the final reconstruction matrix is updated by adding the transformation of the root node with respect to the paleotectonic reference frame, $\boldsymbol{R}_c$. At step #4, the current rotation matrix is updated by adding the relative rotation of the current node with respect to its parent. Then, at the next step, we move upwards to the next higher level by assigning the current node its parent and the sequence is restarted. On exit, this algorithm furnishes the total reconstruction matrix of $n$ at time $T$ in the variable $\boldsymbol{R}_n(T)$.

As an example, the application of this algorithm to the circuit of Fig. 2.28 would give the following total reconstruction matrices:

$$\begin{cases} \boldsymbol{R}_A(T) = \boldsymbol{R}_C(T)\boldsymbol{R}_{AC}(T) \\ \boldsymbol{R}_B(T) = \boldsymbol{R}_C(T)\boldsymbol{R}_{BC}(T) \\ \boldsymbol{R}_D(T) = \boldsymbol{R}_C(T)\boldsymbol{R}_{DC}(T) \\ \boldsymbol{R}_E(T) = \boldsymbol{R}_C(T)\boldsymbol{R}_{DC}(T)\boldsymbol{R}_{ED}(T) \end{cases}$$

To calculate the set of finite reconstruction matrices $\boldsymbol{R}_{ij}(T)$ associated with a plate circuit at a given intermediate time $T$, algorithm 2.2 uses the components of these transformation matrices at stage boundaries. If $T_{k-1} \leq T \leq T_k$, then the corresponding finite reconstruction of plate $i$ relative to plate $j$ is given by:

$$\boldsymbol{R}_{ij}(T) = \boldsymbol{S}_{ij}\,(T_{k-1}, T)\;\boldsymbol{R}_{ij}\,(T_{k-1}) \qquad (2.47)$$

where the rotation $\boldsymbol{S}_{ij}$ is calculated using the reduced angle (Eq. 2.41). Now we can address the problem of complementing the kinematic representation of a set of tectonic plates through velocity and acceleration fields. We know that the linear velocity $\boldsymbol{v}(\boldsymbol{r})$ at the location represented by a position vector $\boldsymbol{r}$ can be calculated easily starting from an Euler vector $\boldsymbol{\omega}$ (Eq. 2.17). Therefore, the problem of representing velocity fields can be reduced to the problem of determining the instantaneous axis of relative rotation between two plates sharing a boundary at time $T$, independently from the eventuality that these are conjugate plates or not. Furthermore, it is occasionally necessary to determine *absolute* velocity fields in the selected paleotectonic reference frame. Clearly, in the case of relative velocity fields between conjugate plates the calculation should be simplified by the fact that the relative motions are rotations about fixed axes at constant angular velocities. However, even in this eventuality it is necessary to take into account that the rotation axis of a stage pole is fixed with respect to a plate that is considered at rest in the present day geographic frame. Therefore, the axis must be rotated according to the total reconstruction matrix of this plate at time $T$ before it can be used for calculating velocity vectors. Let $\boldsymbol{n}_{ij}(0)$ be the unit vector of the rotation axis associated with a stage rotation $\boldsymbol{S}_{ij}(T_{k-1},T_k)$. If $T_{k-1} \leq T \leq T_k$, and $\boldsymbol{R}_j(T)$ is the total reconstruction matrix of the reference plate at time $T$, then the orientation of this axis at time $T$ will be given by:

$$\boldsymbol{n}_{ij}(T) = \boldsymbol{R}_j(T)\boldsymbol{n}_{ij}(0) \qquad (2.48)$$

At this point, to form a complete Euler vector we still need to assign an angular velocity $\omega$ at time $T$. This task can be easily accomplished, because during a stage the relative angular velocity between two plates is assumed to be approximately constant, thereby we can always determine this quantity starting from the stage angle $\Omega_k$ and the temporal boundaries $T_{k-1}$ and $T_k$. It results:

$$\omega = \frac{\Omega_k}{T_k - T_{k-1}} \qquad (2.49)$$

In the general case of two plates whose relative motion occurs about a continuously changing Euler pole, it is not possible to determine the instantaneous rotation axis and angular velocity starting from a stage rotation. Therefore, a more general, although complicate, approach to the problem becomes necessary. We know that all the plates are represented in a plate circuit at time $T$. For each node $i$, a finite reconstruction matrix $\boldsymbol{R}_{ij}(T)$ exists, which allows to calculate the position of the corresponding plate with respect to the parent plate $j$. We also know that the edges of a plate circuit attest the existence of specific kinematic relations between plate pairs, consisting in the fact that the relative motions are stage rotations, thereby they link pairs of *conjugate plates*. Therefore, for *any* plate $i$ not coinciding with the root of the tree, it is possible to determine a stage rotation matrix $\boldsymbol{S}_{ij}$ and the relative velocity field $\boldsymbol{v}_{ij}$ with respect to the parent plate $j$ in the hierarchical representation using the following simple expression, which combines Eq. (2.17) with Eqs. (2.48) and (2.49):

$$\boldsymbol{v}_{ij}(\boldsymbol{r},T) = \frac{\boldsymbol{R}_j(T)\boldsymbol{n}_{ij}(0)\Omega_k}{T_k - T_{k-1}} \tag{2.50}$$

for any $T_{k-1} \leq T \leq T_k$. In the case of the root continent, $r$, the corresponding finite reconstruction matrix coincides with a total reconstruction matrix, $\boldsymbol{R}_r(T)$, that represents the transformation of $r$ with respect to the paleotectonic reference frame. Therefore, if $(i,j,k,\ldots,r)$ is a path in the tree structure from node $i$ to the root, then we can always determine the *absolute velocity field* of a plate in the selected reference frame by composition of velocity vectors:

$$\boldsymbol{v}_i(\boldsymbol{r},T) = \boldsymbol{v}_{ij}(\boldsymbol{r},T) + \boldsymbol{v}_{jk}(\boldsymbol{r},T) + \cdots + \boldsymbol{v}_r(\boldsymbol{r},T) \tag{2.51}$$

where the absolute velocity field of the root node, $\boldsymbol{v}_r$, is determined calculating stage rotations with respect to the paleotectonic reference frame.

Now we are ready to solve the problem of determining relative velocity fields between non-conjugate plate pairs. In fact, if $i$ and $j$ are *any* two plates, it is always possible to calculate their relative velocity by subtracting their absolute velocities:

$$\boldsymbol{v}_{ij}(\boldsymbol{r},T) = \boldsymbol{v}_i(\boldsymbol{r},T) - \boldsymbol{v}_j(\boldsymbol{r},T) \tag{2.52}$$

Another important kinematic variable is the relative or absolute acceleration of a tectonic plate. Curiously, this kind of vector fields have been seldom considered in plate kinematics studies, in spite of their importance for the geodynamic assessment of the models. Probably this is a consequence of the fact that accelerations have been traditionally considered as point events that only occur at stage boundaries, consistently with the current description of the driving mechanism of plate tectonics. However, recent research has shown that phases of accelerated motion have existed in the geologic past, possibly associated with the action of mantle plumes (Cande and Stegman 2011). We shall consider in detail the geodynamics of accelerated states in Chap. 13. In order to obtain an acceleration field, it is necessary to consider two successive times, $T$ and $T'$, close enough, and calculate a velocity field for each of them. For example, Schettino and Scotese (2002) used a time interval of 1 Myr for determining the acceleration across stage boundaries in the Mediterranean region during the Mesozoic. The acceleration is calculated simply by dividing the velocity variation by the size of the time interval:

$$\boldsymbol{a}_{ij}(\boldsymbol{r},T) = \frac{\boldsymbol{v}_{ij}(\boldsymbol{r},T') - \boldsymbol{v}_{ij}(\boldsymbol{r},T)}{T' - T} \tag{2.53}$$

It is possible that in the previous discussion, about the velocity field between non-conjugate plate pairs, some readers wondered about the effective number of situations characterized by this kind of relative motion. We shall satisfy the curiosity of these readers by proving an interesting topological theorem, which will help to clarify some key features of plate tectonic configurations. We say that a plate boundary is a *conjugate boundary* if it separates a pair of conjugate plates. In this instance, any geological structure associated with strike-slip motion, for example a transform fault, will be aligned with

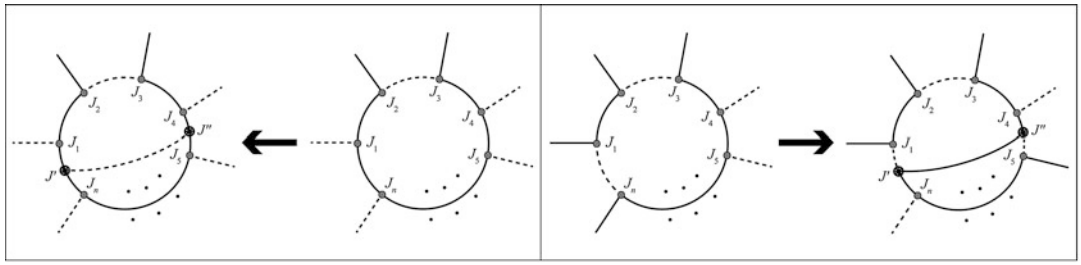

**Fig. 2.32** Nucleation of a new plate by splitting of an existing $n$-th order plate. Free plate boundaries are shown as *dashed lines*. *Left*: The new plate boundary splits two conjugate boundaries through the insertion of two new triple junctions, $J'$ and $J''$. In this case, the new boundary is a free boundary and there is no need for a global reorganization. *Right*: If one of the two boundaries that are cut is a free boundary, then a large scale reorganization, involving several conversions between free and conjugate boundaries, is necessary. In this instance, a new conjugate boundary separates the parent plate from the newly formed tectonic element

a small circle arc about a stage pole. When a boundary separates two plates whose relative motion occurs about a continuously changing Euler pole, we say that this is a *free boundary*. In this case, strike-slip faults, in particular transform faults, and fracture zones have a quite complicate pattern, as illustrated in Fig. 2.26. If $C$ is a plate circuit containing $p$ nodes, then its size (i.e., the number of edges) is given by $e = p-1$. The following theorem proves that this number does *not* coincide with the total number of conjugate pairs in a plate tectonic configuration, that is, with the total number of conjugate boundaries, but is always lower.

**Topological Theorem (for Plate Tectonic Configurations)**
*If $G(j,b)$ is a global plate configuration, then the number of free and conjugate boundaries are given, respectively, by:*

$$f = \frac{1}{3}b = e - 1 = p - 2 \tag{2.54}$$

$$c = \frac{2}{3}b = j = 2f \tag{2.55}$$

*Proof* In this proof, we always assume that in *normal conditions* a system of tectonic plates tries to maximize the number of conjugate boundaries during any episode of reorganization, because this is clearly a minimum energy configuration. In a three-plates system, it results by (2.34) that $b = 3$ and $j = 2$. We have already proved that in this configuration only two of the three boundaries can be conjugate boundaries, thereby we would have $f = 1$ and $c = 2$, in agreement with Eqs. (2.54) and (2.55). Now let us assume that the theorem holds for a system with $p$ plates. We want to prove that in this case it also holds if one of these plates splits, thus adding a new tectonic element to the system.

Figure 2.32 shows two possible mechanisms for generating a new additional tectonic plate from an existing one. Clearly, in order to create a new boundary that splits an existing plate, two of its boundaries must be broken by insertion of triple junctions. If the edges that are split are conjugate boundaries, two extra conjugate boundaries and one additional free boundary are created and there is no need to change the tectonic style of the remaining plate boundaries. In this instance, $f$ increases by one, while $c$ increases by two, thereby Eqs. (2.54) and (2.55) remain valid and the theorem is proved. The new plate boundary separating the two parts of the original plate is always a free boundary when this kind of plate nucleation occurs. A much more complicated situation follows if at least one of the two boundaries that are split is a free boundary. In this instance, the proof relies on the fact that for any pair of triple junctions in $G$, there exist at least three *alternate paths* that link the two nodes. An alternate path is a path formed by an alternate sequence of conjugate and free edges.

The example of Fig. 2.33 shows the tree structure that can be formed with the set of all alternate

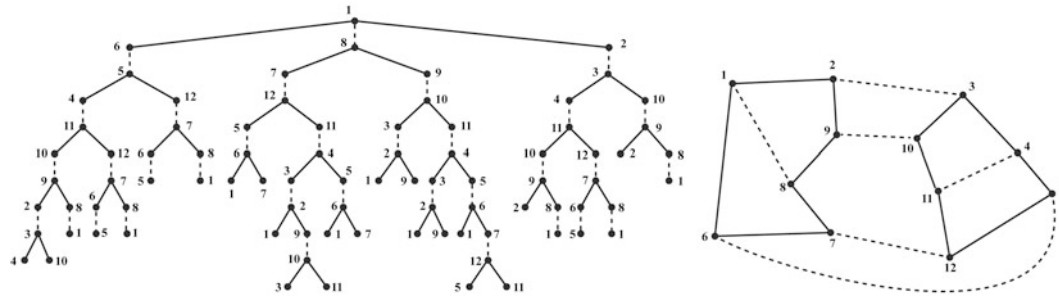

**Fig. 2.33** An example of global plate configuration, and the corresponding tree of alternate paths starting from node $J_1$. *Dashed* and *solid lines* are respectively free and conjugate plate boundaries

paths starting from a node. The tree is built setting the root node as the start node, $s$, and generating all the possible alternate paths originating in $s$ by a modified depth-first search or breadth-first search algorithm (see Appendix 2). For example, for the graph of Fig. 2.33 we could start from node $J_1$, then reach nodes $J_2$, $J_6$, and $J_8$. From node $J_2$, we must proceed to node $J_3$, while from $J_8$ we can proceed either to node $J_7$, or node $J_9$, etc. When one of the edges that are split in the process of nucleation of a new tectonic plate is a free boundary, the new intermediate boundary separating the original plate cannot be a free boundary. More precisely, it *could* be a free boundary, but this would not be the minimum energy solution. In fact, Fig. 2.32 shows that after insertion of the new triple junctions $J'$ and $J''$, only one of the two arms of a free boundary needs to be converted to a conjugate boundary after splitting (the boundary between $J'$ and $J_n$ in the example of Fig. 2.32), whereas any other solution would imply a local reorganization involving more conversions. However, even in this case the conversion of part of the former free boundary induces a series of concatenate transitions from free to conjugate boundaries and vice versa that may propagate outside the perimeter of the splitting plate, determining a total rearrangement of the plate configuration. For each boundary conversion, another boundary incident with the same triple junction must be subject to the inverse of that transformation. At the same time, a stage boundary is created, which could either close an existing stage or start a new one after a time interval of complex relative motion. The simplest way to terminate the sequence of boundary conversions and establish a new equilibrium is to reach the opposite triple junction, $J''$, along the shortest alternate path. This path will include an even number of edges when only one of the splitting boundaries is a free boundary, whereas an odd number of edges are converted when two free boundaries are split. The examples of Fig. 2.34 illustrate these two possibilities.

It should be noted that the new boundary linking $J'$ and $J''$, and the alternate path linking these nodes form a closed loop in $G$, whose outgoing edges are unaffected by the boundary conversions. In the case of an even number of converted edges, for each conjugate boundary that is transformed into a free boundary there is a free boundary that is converted into a conjugate boundary. Therefore, after the creation of a new free boundary and two new conjugate boundaries the total number of edges does not change. This implies that also in this case $f$ and $c$ increase respectively by one and by two units, thereby Eqs. (2.54) and (2.55) remain valid and the theorem is proved. When the number of converted boundaries is odd, after the creation of two new free boundaries (see Fig. 2.34) and one additional conjugate boundary the sequence of conversions allows an extra conversion of the last free boundary into a conjugate edge, thereby during the conversions $f$ decreases by one and $c$ increases by one. Therefore, also in this case $f$ and $c$ increase respectively by one and by two units, so that Eqs. (2.54) and (2.55) conserve their validity after the formation of the new plate. This proves the topological theorem. ■

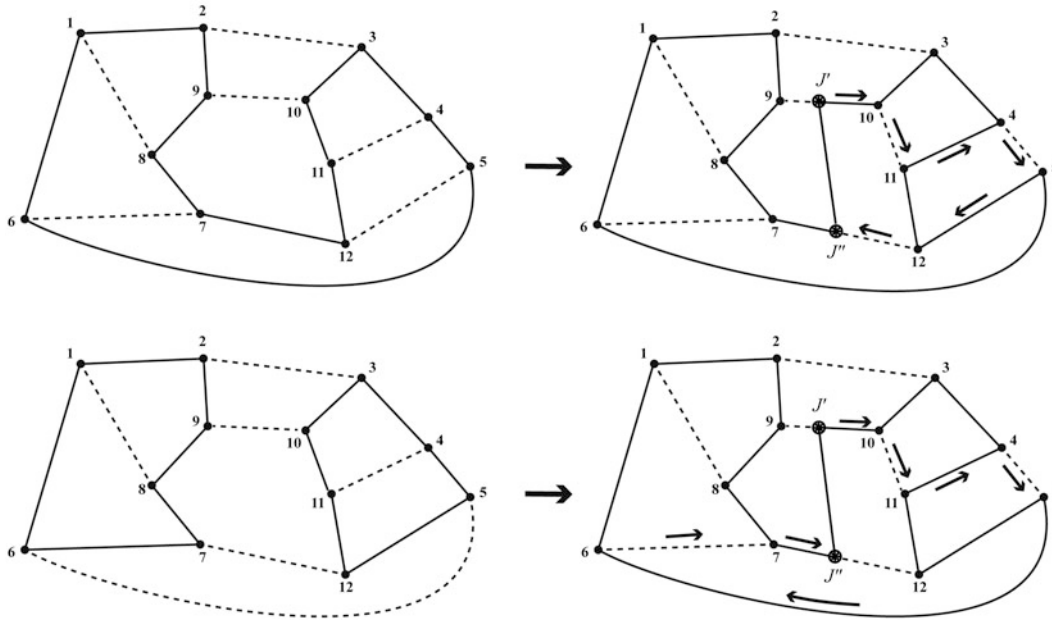


**Fig. 2.34** Alternate paths of converted boundaries during the splitting of a tectonic plate. *Top*: The new edge links a free boundary to a conjugate boundary. *Bottom*: Two free boundaries are split

In Sect. 2.7 we have described a method of construction of flow lines of relative motion, which can be used only when the two plates form a conjugate pair. Furthermore, we have mentioned that it is not generally applicable to the case of convergent boundaries. Now we want to describe a technique to produce flow lines in the general case of two plates separated by a free boundary for at least some time intervals. The method is based on the general technique for determining relative velocity fields discussed above. Let $\boldsymbol{r}_0$ be the present day position vector of a point belonging to a plate $B$. We want to generate a path on the globe, formed by the relative positions of this point with respect to another plate $A$ at any time $T$ in the geologic past. The task is easily accomplished calculating the relative velocity field $\boldsymbol{v}_{BA}(T)$ for a sequence of closed times $T'$, $T' + \delta T$, $T' + 2\delta T, \ldots$ in an interval $[T', T'']$. In fact, starting from the position at the initial time, which is $\boldsymbol{r}(T') = \boldsymbol{R}_{BA}(T')\boldsymbol{r}_0$, we can calculate iteratively the position at any successive time by the following formula:

$$\boldsymbol{r}\,(T + \delta T) = \boldsymbol{r}(T) + \boldsymbol{v}_{BA}(T)\delta T \qquad (2.56)$$

The kinematic methods described so far can be applied equally well to the reconstruction of the tectonic evolution of oceanic basins and to continental tectonics. In the former case, the finite reconstruction matrices associated with the rotation model are determined on the basis of an analysis of fracture zones and the pattern of marine magnetic anomalies, as it will be explained in Chap. 5. In the case of reconstructions that involve deformation of continental crust in the geologic past, for example during rifting or collisions, or when the finite rotations must describe relative motions between continental blocks, these techniques are inapplicable. In this context, the determination of the reconstruction parameters (latitude and longitude of the Euler poles and rotation angles) mostly relies on geologic data that lack of information on measurement uncertainty, thereby it is not generally possible to determine confidence ellipses for the resulting reconstruction parameters. Nevertheless, it is possible to generate semi-quantitative reconstructions that correctly predict the style and timing of tectonic deformation, thus giving a theoretical framework to the geological observation at regional or local scale.

The asymmetric deformation of a tectonic element of continental crust during its motion can be described by modifying the format of the tables associated with rotation models (Fig. 2.29). Such a modification should consist into the introduction of an additional field, which would allow to establish the amount of shortening or extension, with respect to the present day shape, that a block experienced during its motion. This method cannot be used to describe a symmetric extension between two plates during a rifting phase, because the additional attribute refers to a single tectonic element which will be rotated with respect to a parent plate, not to a plate pair. For example, the method can be used in the modelling of back arc basins, or in the description of complex systems, such as the assemblage of microplates, slivers, and orogenic structures that characterizes the Alpine-Himalayan belt. In general, the additional field would describe the deformation of a continental block during a stage rotation through a stretching (or shortening) factor. For example, a value of 0.9 at 10 Ma would mean that in a reconstruction at 10 Ma we must shorten the tectonic element by 10 % with respect to the present size, in the direction determined by the stage matrix between 10 Ma and the present. Similarly, if the deformation parameter is 0.8 at 20 Ma, this value implies two different phases of extension, the first one between 20 and 10 Ma and a second one between 10 Ma and the present. Of course, these two phases of deformation could develop along different directions, determined by diverse stage poles, so that in general the present day shape of a tectonic element would result from the superposition of several tectonic events. An example illustrating the combination of rotations and phases of extension is shown in Fig. 2.35.

Describing the kinematics of deformable bodies requires special techniques and an additional computational effort for generating plate reconstructions of the tectonic evolution of a region. For example, it is not generally possible to determine the initial shape and location of a tectonic element through a single finite rotation, accompanied by deformation of the block, because usually the present day geometry results from the superposition of different phases of extension

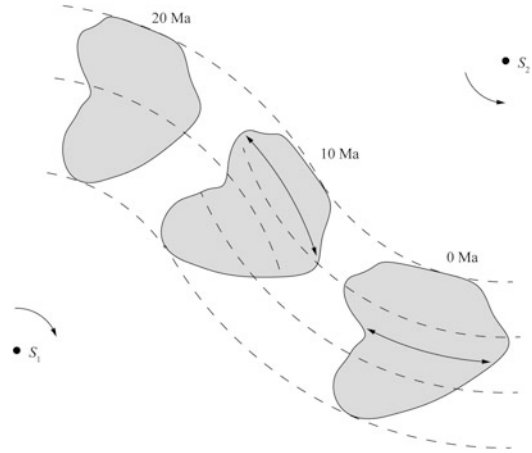


**Fig. 2.35** Deformation of a continental block during its motion. In this example, a tectonic element rotates clockwise about the stage pole $S_1$ between 20 and 10 Ma, and counterclockwise about $S_2$ between 10 Ma and the present. During the first stage, it is stretched in the same directions of the flow lines about $S_1$. Then, a second phase of deformation is superimposed on the first one, and the block is stretched again, this time in the direction of the flow lines about $S_2$

or shortening, which develop along distinct axes of deformation. Now we are going to describe, in a simplified form, the procedure of stretching or shortening of a tectonic element along an assigned direction, which cannot be defined as a trivial algorithm.

The procedure of block deformation starts with its rotation to a reference frame where the stage pole coincides with the North Pole (Fig. 2.36). Then, the points having minimum and maximum latitudes, in the set of $N$ vertices associated with the spherical polygon representation, are determined. Let $\boldsymbol{q}_s$ and $\boldsymbol{q}_n$ be respectively these two points (Fig. 2.36), and assume that the sequence of vertices $(\boldsymbol{q}_1, \boldsymbol{q}_2, \ldots, \boldsymbol{q}_N)$ is a clockwise sequence. The points $\boldsymbol{q}_s$ and $\boldsymbol{q}_n$ can be used to divide the perimeter of the tectonic element in two halves: an eastern half that includes vertices from $\boldsymbol{q}_s$ to $\boldsymbol{q}_n$, and a western sequence, which includes vertices from $\boldsymbol{q}_n$ to $\boldsymbol{q}_s$. For each point in the western sequence, $\boldsymbol{q}_i$, let $\delta\phi_i$ be the longitudinal distance from the western boundary. If $\beta$ is the deformation factor, then $\boldsymbol{q}_i$ is moved along its parallel to a new location, $\boldsymbol{q}'_i$, in such a way that $\delta\phi'_i = \beta\delta\phi_i$. Finally, the resulting

polygon is moved back to the original reference frame before applying the rigid transformation listed in the rotation model.

Another problem that often must be solved, in the context of continental tectonics, is associated with the impossibility to determine a priori, independently from the specific kinematic history, a list of finite reconstruction poles to be included in a rotation model. The reason is that the typical geological data are generally represented by partially incoherent geologic structures (faults, fold axes, etc.), which result from the superposition of two or more phases of deformation, as illustrated in Fig. 2.37. Even assuming that it is possible to separate the original data in coherent subsets, and to identify the timing of the deformation phases through a precise dating of the geologic structures, the oldest tectonic structures cannot be used to determine finite reconstruction parameters, because it is likely that their strike has been affected by the more recent phases of deformation. In these conditions, the typical approach is to reconstruct the tectonic history of a region starting from the most recent phase of deformation and going back through time. If we can identify the most recent set of geologic structures, for example between some time $T_k$ and the present (Fig. 2.37), then it is possible to determine the parameters of a stage transformation $\boldsymbol{S}(0,T_k)$, which clearly coincides with the finite reconstruction matrix at time $T_k$: $\boldsymbol{S}(0,T_k) = \boldsymbol{R}(T_k)$. At this point, all the structures that are older than $T_k$, and that have been affected by the most recent phase of deformation, are rotated using the matrix $\boldsymbol{R}(T_k)$, in order to remove the "overprint" of this phase. After this operation, these structures become coherent with other data that had not been affected by the recent deformation. The resulting data set can be used, at the next step, to determine a second stage pole, $\boldsymbol{S}(T_k,T_{k-1})$, which in turn allows to calculate the finite reconstruction matrix at time $T_{k-1}: \boldsymbol{R}(T_{k-1}) = \boldsymbol{S}(T_k, T_{k-1})\boldsymbol{R}(T_k)$, and

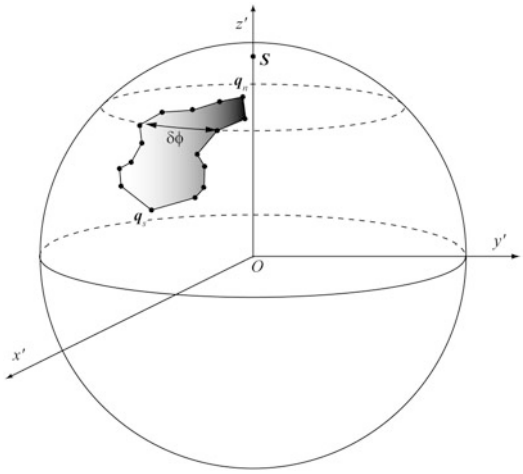


**Fig. 2.36** Stretching and shortening continental blocks by a factor β. In a reference frame $(x',y',z')$ where the stage pole, $\boldsymbol{S}$, has been moved to the North Pole, the northernmost and southernmost vertices, $\boldsymbol{q}_n$ and $\boldsymbol{q}_s$, of a plate polygon are used to divide the block perimeter in two halves. Then, each point along the eastern half is moved along its parallel of latitude to stretch or shorten by factor β the corresponding *small circle* arc δϕ that separates it from the western boundary

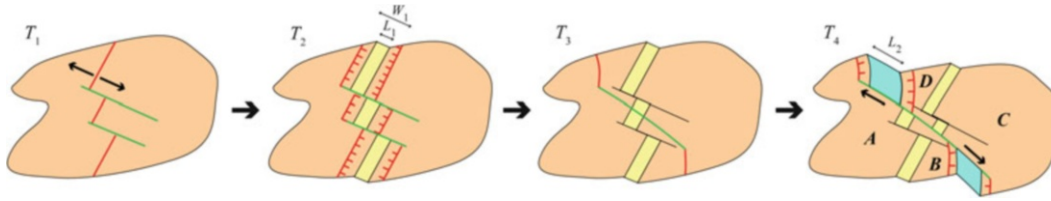


**Fig. 2.37** Superposition of two phases of deformation of a tectonic element. During phase 1, between $T_1$ and $T_2$, a rift forms with extension axes having direction WNW−ESE. Note that the resulting offset $L$ between the two separating blocks is always less than the width $W$ of the stretched zone. This phase is followed by a second episode of extension between $T_3$ and $T_4$, having NW−SE direction, which modifies the strike of some of the original transfer zones and rift axes. At the end of this phase the original block has been divided in four distinct tectonic elements ($A$, $B$, $C$, and $D$). To determine a finite reconstruction pole and angle of rotation for phase 1, it is necessary to remove the effects of the second phase of deformation, by reconstructing the shape of the tectonic element at time $T_3$

**Table 2.2** The NUVEL-1A velocity model

| Plate | $\omega_x$ | $\omega_y$ | $\omega_z$ | $\omega$ | $\lambda_e$ | $\phi_e$ |
|---|---|---|---|---|---|---|
| Africa | 0.002401 | −0.007939 | 0.013891 | 0.9270 | 59.160 | −73.174 |
| Antarctica | 0.000689 | −0.006541 | 0.013676 | 0.8695 | 64.315 | −83.984 |
| Arabia | 0.008195 | −0.005361 | 0.016730 | 1.1107 | 59.658 | −33.193 |
| Australia | 0.009349 | 0.000284 | 0.016253 | 1.0744 | 60.080 | +1.742 |
| Caribbean | 0.001332 | −0.008225 | 0.011550 | 0.8160 | 54.195 | −80.802 |
| Cocos | −0.008915 | −0.026445 | 0.020895 | 1.9975 | 36.823 | −108.629 |
| Eurasia | 0.000529 | −0.007235 | 0.013123 | 0.8591 | 61.066 | −85.819 |
| India | 0.008181 | −0.004800 | 0.016760 | 1.1034 | 60.494 | −30.403 |
| North America | 0.001768 | −0.008439 | 0.009817 | 0.7486 | 48.709 | −78.167 |
| Nazca | −0.000022 | −0.013417 | 0.019579 | 1.3599 | 55.578 | −90.096 |
| South America | 0.000472 | −0.006355 | 0.009100 | 0.6365 | 54.999 | −85.752 |

$\omega = (\omega_x{}^2 + \omega_y{}^2 + \omega_z{}^2)^{1/2}$ is the angular velocity in deg/Myr;
$\omega_x$, $\omega_y$, and $\omega_z$ are expressed in rad/Myr;
$\lambda_e$ and $\phi_e$ are, respectively, the latitude and longitude of the Euler pole with respect to the Pacific

so on. Thus, in general, the finite reconstruction poles associated with the kinematics of a set of continental plates can be calculated only *after* the stage transformations have been determined by concatenation of stage matrices.

## 2.9 Current Plate Motions

We are going to conclude this chapter, dedicated to plate kinematics, with a description of the techniques used for the determination of the modern plate motions. The first models of current plate kinematics were based on a combination of heterogeneous data, represented by seismic slip vectors, averaged spreading rates, and transform fault azimuths (Chase 1978; Minster and Jordan 1978; DeMets et al. 1990). Each of these models specified a set of $n-1$ Euler vectors, $\boldsymbol{\omega}_i$, $n$ being the number of modern plates, relative to a reference plate, for example the Pacific plate. The models were obtained through least squares procedures that minimized the quantity:

$$\chi^2 = \sum_{i=1}^{n-1}\sum_{j=1}^{n_i}\sum_{k=1}^{N_{ij}} \left\{ \frac{\left[\boldsymbol{v}(\boldsymbol{r}_k) - (\boldsymbol{\omega}_i - \boldsymbol{\omega}_j)\times \boldsymbol{r}_k\right]\cdot \boldsymbol{n}_k}{\sigma_k} \right\}^2 + \sum_{i=1}^{n-1}\sum_{j=1}^{m_i}\sum_{k=1}^{M_{ij}} \frac{1}{\sigma_k^2}\left[\boldsymbol{s}(\boldsymbol{r}_k) - \frac{(\boldsymbol{\omega}_i - \boldsymbol{\omega}_j)\times \boldsymbol{r}_k}{\left|(\boldsymbol{\omega}_i - \boldsymbol{\omega}_j)\times \boldsymbol{r}_k\right|}\right]^2 \tag{2.57}$$

This formula allows to calculate the squared sum of misfits between predicted and observed spreading rates and azimuths of relative velocities. Each plate is assumed to have $n_i$ boundaries that are spreading ridges, and for each of these boundaries, there are $N_{ij}$ spreading rate data at locations represented by position vectors $\boldsymbol{r}_k$. Let $\boldsymbol{\omega}_i - \boldsymbol{\omega}_j$ be the predicted relative angular velocity of the $i-$th plate with respect to an adjacent plate separated by a spreading ridge. By (2.17), the predicted linear velocity between the two plates at a location $\boldsymbol{r}_k$ is given by: $(\boldsymbol{\omega}_i - \boldsymbol{\omega}_j)\times \boldsymbol{r}_k$. If $\boldsymbol{n}_k$ and $\boldsymbol{v}(\boldsymbol{r}_k)$ are respectively a versor normal to the ridge axis and the observed average spreading velocity at $\boldsymbol{r}_k$, then the weighted misfit between observed and predicted spreading rates is given by the scalar difference between the projections of $\boldsymbol{v}(\boldsymbol{r}_k)$ and $(\boldsymbol{\omega}_i - \boldsymbol{\omega}_j)\times \boldsymbol{r}_k$ onto the axis of $\boldsymbol{n}_k$, divided by the standard error $\sigma_k$ attributed to $v(\boldsymbol{r}_k)$. Similarly, it is assumed that the $i-$th plate has $m_i$ generic boundaries, each having $M_{ij}$ directional observations. Let $\boldsymbol{s}(\boldsymbol{r}_k)$ be a unit versor representing one of these observations. The predicted direction is clearly given by the versor of the theoretical linear velocity $(\boldsymbol{\omega}_i - \boldsymbol{\omega}_j)\times \boldsymbol{r}_k$. Therefore, the weighted misfits of azimuth data can be defined as the magnitudes of the vector differences between predicted and observed direction versors, divided by the standard error $\sigma_k$.

Table 2.2 lists the Euler vectors of NUVEL-1A (DeMets et al. 1994), one of the most widely

accepted kinematic models for the modern plates, which represents a refinement of a model published in 1990, known as NUVEL-1 (Northwestern University VELocity model ver. 1, DeMets et al. 1990). In this model, the average spreading rates used in the least squares fitting procedure are determined through the analysis of marine magnetic anomalies spanning the last ∼3.2 Myrs. The model includes 12 large plates, and the components of the Euler vectors are expressed in a reference frame fixed to the Pacific plate. The difference between the two versions is in the geomagnetic polarity time scales used to analyse the marine magnetic anomalies during the determination of the spreading rates, so that the angular velocities of NUVEL-1A are 95.62 % of the corresponding velocities listed in NUVEL-1.

One of the main problems of the classic models is represented by the very different time intervals associated with the input data. The spreading rates along the world's mid-ocean ridges, which are estimated through the analysis of marine magnetic anomalies, represent averages over the last ∼3.2 Myrs. These averages strongly depend from the choice of a geomagnetic polarity time scale. Conversely, earthquake slip vectors average directions of relative motions over much shorter time intervals (decades to centuries). Another problem is represented by the relatively small number of plates that are considered in these models, which limits their capability to represent the internal deformation of some continents. Therefore, there is not much surprise in seeing that inconsistencies often emerge when the linear velocities predicted on the basis of the Euler vectors are compared to velocities estimated from Global Positioning System (GPS) techniques and other geodetic methods. In fact, the latter data are consistent averages performed over a few decades, which are not necessarily representative of the long-term geological processes. Finally, the most serious issue of NUVEL-1A and its predecessors is probably the failure to satisfy the closure rule (Eq. 2.35) along some three-plate circuits. In particular, NUVEL-1A does not satisfy Eq. 2.36 at the Galapagos triple junction (Pacific-Cocos-Nazca circuit) and at the Bouvet triple junction (Africa-South America-Antarctic circuit) at the desired level of confidence.

A major improvement to NUVEL-1A, which tries to overcome the difficulties mentioned above, has been proposed in recent times by DeMets et al. (2010). The new model, which has been called MORVEL (Mid-Ocean Ridge VELocity), extends the data set to the 25 plates shown in Fig. 2.38. With respect to the system of 23 plates shown in Fig. 2.16, this model decomposes the eastern part of Africa in two sub-plates (Lwandle and Somalia), separates two sub-plates (Capricorn, and Macquarie) from Australia, introduces the Yang-Tze plate in eastern Asia and Sur in the South Atlantic, but incorporates the Anatolian block in Eurasia, Easter in Nazca, and the Okhotsk plate in N. America. Using Eq. 2.34, we see that this model includes 46 triple junctions and 69 plate boundaries, 23 of which must be free boundaries. Differently from its predecessors, MORVEL is based on few earthquake slip directions. In this model, about 75 % of the input data are sea floor spreading rates and strikes of transform faults. The very limited usage of earthquake slip vectors (∼2 % of the total data set) has minimized the possibility of biased estimates of relative velocity directions along the world's subduction zones, which are usually caused by forearc deformation (e.g., Jarrard 1986; McCaffrey 1992). Finally, it has been avoided a mix between long-term geological data and geodetic velocities in the estimation of Euler vectors, the usage of GPS data having been limited to the determination of the motion of six small plates, for which no other data were available. The 24 Euler vectors of MORVEL, relative to the Pacific plate, are listed in Table 2.3, while the resulting linear velocity fields between adjacent plates are shown in Fig. 2.38.

The kinematic models described so far furnish the Euler vectors of the major modern tectonic plates relative to the Pacific. The components of these vectors are expressed in the geographic reference frame (where London, Eurasia, has a fixed longitude). By vector summation, we can calculate the Euler vector of relative motion between any pair of plates, assess closure conditions

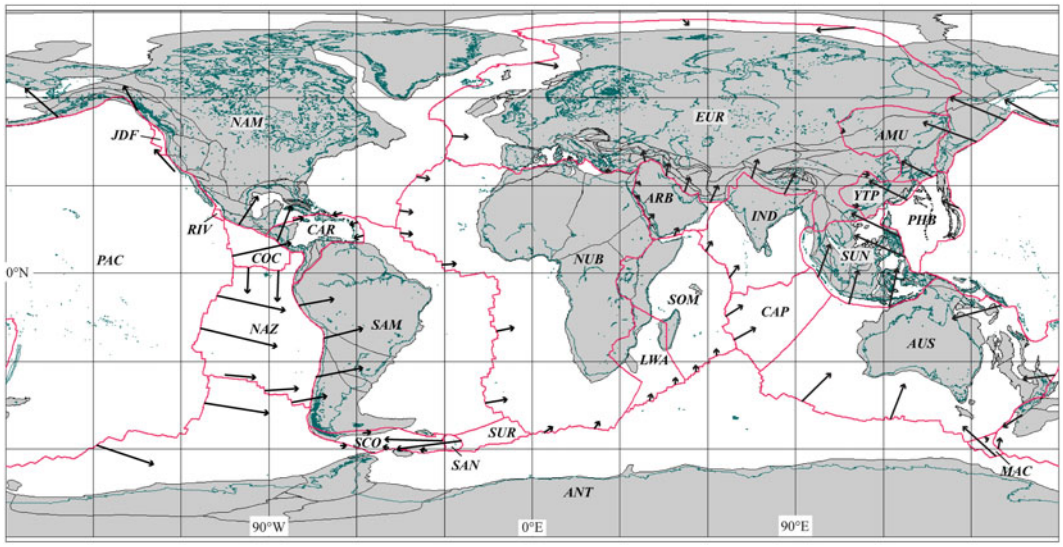


**Fig. 2.38** The plate velocity model MORVEL (DeMets et al. 2010). The *length of the arrows* indicates 20 times the relative displacement of a plate with respect to an adjacent plate. Plate labels are listed in Table 2.3

**Table 2.3** The MORVEL velocity model

| Plate | Sym | $\lambda_e$ | $\phi_e$ | $\omega$ | $\omega_x$ | $\omega_y$ | $\omega_z$ |
|---|---|---|---|---|---|---|---|
| Amurian | AMU | 65.9 | −82.7 | 0.929 | 0.000841 | −0.006567 | 0.014801 |
| Antarctica | ANT | 65.9 | −78.5 | 0.887 | 0.001260 | −0.006194 | 0.014132 |
| Arabia | ARB | 60.0 | −33.2 | 1.159 | 0.008463 | −0.005538 | 0.017518 |
| Australia | AUS | 60.1 | 6.3 | 1.079 | 0.009331 | 0.001030 | 0.016325 |
| Caribbean | CAR | 55.8 | −77.5 | 0.905 | 0.001922 | −0.008668 | 0.013064 |
| Cocos | COC | 42.2 | −112.8 | 1.676 | −0.008397 | −0.019977 | 0.019649 |
| Capricorn | CAP | 62.3 | −10.1 | 1.139 | 0.009098 | −0.001621 | 0.017601 |
| Eurasia | EUR | 61.3 | −78.9 | 0.856 | 0.001381 | −0.007040 | 0.013105 |
| India | IND | 61.4 | −31.2 | 1.141 | 0.008154 | −0.004938 | 0.017484 |
| Juan de Fuca | JDF | −0.6 | 37.8 | 0.625 | 0.008619 | 0.006685 | −0.000114 |
| Lwandle | LWA | 60.0 | −66.9 | 0.932 | 0.003191 | −0.007481 | 0.014087 |
| Macquarie | MAC | 59.2 | −8.0 | 1.686 | 0.014921 | −0.002097 | 0.025276 |
| North America | NAM | 48.9 | −71.7 | 0.750 | 0.002702 | −0.008170 | 0.009864 |
| Nubia | NUB | 58.7 | −66.6 | 0.935 | 0.003367 | −0.007781 | 0.013944 |
| Nazca | NAZ | 55.9 | −87.8 | 1.311 | 0.000492 | −0.012819 | 0.018947 |
| Philippine | PHB | −4.6 | −41.9 | 0.890 | 0.011524 | −0.010340 | −0.001246 |
| Rivera | RIV | 25.7 | −104.8 | 4.966 | −0.019950 | −0.075508 | 0.037587 |
| South America | SAM | 56.0 | −77.0 | 0.653 | 0.001434 | −0.006210 | 0.009449 |
| Scotia | SCO | 57.8 | −78.0 | 0.755 | 0.001460 | −0.006868 | 0.011150 |
| Somalia | SOM | 59.3 | −73.5 | 0.980 | 0.002480 | −0.008373 | 0.014707 |
| Sur | SUR | 55.7 | −75.8 | 0.636 | 0.001534 | −0.006064 | 0.009170 |
| Sundaland | SUN | 59.8 | −78.0 | 0.973 | 0.001776 | −0.008356 | 0.014677 |
| South Sandwich | SAN | −3.8 | −42.4 | 1.444 | 0.018570 | −0.016957 | −0.001670 |
| Yang Tze Platform | YTP | 65.5 | −82.4 | 0.968 | 0.000927 | −0.006945 | 0.015374 |

across plate circuits, test triple junction velocity triangles, etc. What we cannot do with these models, is to represent the *absolute* velocities of the tectonic plates with respect to a reference frame fixed to the deep mantle, for example fixed to the top of the transition zone as in Fig. 2.9. However, this is a necessary step if we want to consider the kinematics of tectonic plates in relation to the asthenospheric flows, and give a complete geodynamic formulation of plate tectonics. Such approach represents one the fundamental tasks of this book, thereby now we shall illustrate an approximate method to determine the Euler vectors in a reference frame fixed to the deep mantle.

The method was proposed 40 years ago by Solomon and Sleep (1974) and applies equally well to the modern plates and to a paleotectonic context (Solomon et al. 1977). These authors started from the assumption that the total torque $\boldsymbol{N}$ exerted on the lithosphere (Eq. 2.3) is zero, and that the asthenosphere is dragged passively by the overlying lithosphere. The first assumption is compatible with the fact that, apart from the case of space geodesy studies, we always represent plate motions through the *geological time*, not the physical time, even when we study the present day plate motions. When we consider physical processes that occur at the time scale of the last 2–3 Myrs, it is always necessary to neglect any motion related to the Earth's rotation, including variations in eccentricity of the orbit, axial tilt, and precession. In Chap. 6, we shall discuss the evidence that the total angular momentum $\boldsymbol{L}$ (Eq. 2.5) of the lithosphere is constant over time intervals of several Myrs, which implies that in equilibrium conditions $\boldsymbol{N} = \boldsymbol{0}$ at the time scale of the geological processes. We shall prove that also the second assumption is correct in conditions of geodynamic equilibrium, but *not* during episodes of plate acceleration, such as the northward acceleration of India during the Cretaceous to Eocene time interval (Cande and Stegman 2011).

The method of Solomon and Sleep is based on a balance of the torques exerted on the whole lithosphere. The torques applied on individual plates are associated with the viscous resistive drag force that the asthenosphere exerts on the base of the overlying lithosphere, and with plate boundary forces, such as the gravitational forces exerted by slabs. However, it is not necessary to include symmetric features such as mid-ocean ridges in the torque balance, because in this instance the corresponding torques cancel out. Therefore, the two fundamental torques that must be included in the torque balance equation are those associated with drag forces and those arising from downward pull forces exerted by slabs. Let us assume that the passive drag applied at the base of the lithosphere follows a simple viscous law, so that it depends linearly from the velocity of the lithosphere relative to the base of the fluid asthenosphere. It is also reasonable to assume that the slab pull force exerted along an active margin does not depend from the plate velocity. Let $\boldsymbol{\omega}_i$ be the Euler vector of $i$−th plate relative to the top transition zone, and $\boldsymbol{v}_i(\boldsymbol{r}) = \boldsymbol{\omega}_i \times \boldsymbol{r}$ the corresponding linear velocity field at each point $\boldsymbol{r}$ along its surface. The simplest law describing the resistive drag force per unit area (or *traction*) at the base of the lithosphere, $\boldsymbol{T}_i = \boldsymbol{T}_i(\boldsymbol{r})$, is the following one:

$$\boldsymbol{T}_i(\boldsymbol{r}) = -D_i \boldsymbol{v}_i(\boldsymbol{r}) = -D_i \boldsymbol{\omega}_i \times \boldsymbol{r} \tag{2.58}$$

In this expression $D_i$ is a drag coefficient which may depend from position. To obtain the total torque exerted on the $i$−th plate we must integrate the local torque per unit area, $\boldsymbol{r} \times \boldsymbol{T}_i(\boldsymbol{r})$, over the surface $S_i$ of the plate:

$$\boldsymbol{N_i} = -\int_{S_i} [D_i \boldsymbol{r} \times (\boldsymbol{\omega}_i \times \boldsymbol{r})] dS \tag{2.59}$$

From this expression, it is easy to calculate the total torque exerted on the lithosphere by the underlying asthenosphere:

$$\boldsymbol{N} = \sum_i \boldsymbol{N}_i = -\sum_i D_i \int_{S_i} [\boldsymbol{r} \times (\boldsymbol{\omega}_i \times \boldsymbol{r})] dS \tag{2.60}$$

where for simplicity we have assumed that $D_i$ is constant along the surface of a plate. If we expand

the vector triple product in (2.60), this expression can be rewritten as follows:

$$\boldsymbol{N} = -\sum_i D_i \int_{S_i} (\boldsymbol{r}\cdot\boldsymbol{r})\,\boldsymbol{\omega}_i\, dS + \sum_i D_i \int_{S_i} (\boldsymbol{r}\cdot\boldsymbol{\omega}_i)\boldsymbol{r}\, dS_i \tag{2.61}$$

If we assume that the Earth's radius is normalized to unity, then $\boldsymbol{r}\cdot\boldsymbol{r} = 1$, so that:

$$\boldsymbol{N} = -\sum_i D_i S_\iota \boldsymbol{\omega}_i + \sum_i D_i \int_{S_i} (\boldsymbol{r}\cdot\boldsymbol{\omega}_i)\boldsymbol{r}\, dS_i \tag{2.62}$$

Expression (2.62) can be further simplified introducing a new tensor quantity, which is strictly related to the inertial tensor of a tectonic plate (Eq. 2.23). Using the index notation (see Appendix 1), the components of this quantity are given by:

$$Q^i_{jk} \equiv \int_{S_i} \left(\delta_{jk} - x_j x_k\right) dS = A_i \delta_{jk} - \int_{S_i} x_j x_k\, dS;\ j,k = 1,2,3 \tag{2.63}$$

where $A_i$ is the area of the $i$–th plate. Using this new tensor quantity, which depends only from the plate geometry, Expression (2.62) can be rewritten as follows:

$$\boldsymbol{N} = -\sum_i D_i \boldsymbol{Q}^i \boldsymbol{\omega}_i \tag{2.64}$$

If this were the only torque exerted on the lithosphere, the torque balance equation would be written: $\boldsymbol{N} = \boldsymbol{0}$, that is:

$$\sum_i D_i \boldsymbol{Q}^i \boldsymbol{\omega}_i = \boldsymbol{0} \tag{2.65}$$

Let $\boldsymbol{\omega}_r$ be the Euler vector of a reference plate, for example the Pacific plate, with respect to the top transition zone. Knowing the Euler vector of any other plate with respect to the reference plate, $\boldsymbol{\omega}_{ir}$, it is possible to determine its absolute Euler vector, $\boldsymbol{\omega}_i$, by adding the absolute angular velocity of the reference plate: $\boldsymbol{\omega}_i = \boldsymbol{\omega}_{ir} + \boldsymbol{\omega}_r$. Therefore, Eq. (2.65) can be viewed as a linear system of three equations with respect to the three unknown components of $\boldsymbol{\omega}_r$:

$$\left(\sum_i D_i \boldsymbol{Q}^i\right)\boldsymbol{\omega}_r = -\sum_i D_i \boldsymbol{Q}^i \boldsymbol{\omega}_{ir} \tag{2.66}$$

The total $\boldsymbol{Q}$ tensor for the whole lithosphere can be obtained simply by summation of the tensors $\boldsymbol{Q}^i$ associated with each plate. It results:

$$\boldsymbol{Q} = \sum_i \boldsymbol{Q}^i = \frac{8\pi}{3}\boldsymbol{I} \tag{2.67}$$

where $\boldsymbol{I}$ is the identity matrix. Further simplification of Eq. (2.66) follows if we assume that the drag coefficients $D_i$ coincide for all plates: $D_i = D$. In this instance, using (2.67) we obtain an immediate solution for $\boldsymbol{\omega}_r$ in terms of the relative Euler vectors of a velocity model:

$$\boldsymbol{\omega}_r = -\frac{3}{8\pi}\sum_i \boldsymbol{Q}^i \boldsymbol{\omega}_{ir} \tag{2.68}$$

This solution corresponds to a condition of *no-net-rotation* (NRR) for the whole lithosphere ($\boldsymbol{L} = \boldsymbol{0}$). In fact, for $D_i = D$ Eq. (2.65) can be rewritten as follows:

$$\sum_i \boldsymbol{Q}^i \boldsymbol{\omega}_i \equiv \boldsymbol{Q}\boldsymbol{\Omega} = \frac{8\pi}{3}\boldsymbol{\Omega} = \boldsymbol{0} \Rightarrow \boldsymbol{\Omega} = \boldsymbol{0} \tag{2.69}$$

where $\boldsymbol{\Omega}$ can be considered as the net rotation of the whole lithosphere. It should be noted that the solution (2.68) only holds in the unlikely event that the unique torques exerted on the lithosphere come from asthenospheric drag, *and* that the drag coefficient $D$ can be considered constant over the entire lithosphere. Of course, none of these two strong conditions is likely to be verified. Slab pull forces are essential components of the global torque balance, and the drag coefficient along the irregular continental LAB cannot be

equal to the drag coefficient of the oceanic areas. Notwithstanding these issues, the NNR condition (2.68) has been widely used to build "absolute" plate motions models (e.g., Argus and Gordon 1991), and represents the basis for the definition of a geocentric reference frame. This is the International Terrestrial Reference Frame (ITRF), which is particularly important for the representation of kinematic data obtained from geodetic techniques, but it is also linked to an inertial frame tied to stellar objects, the Celestial Reference Frame. This NNR reference frame is periodically updated by the International Earth Rotation and Reference Systems Service (IERS). It is realized through the acquisition of time series of mean station positions at weekly or daily sampling from a global network of observation sites equipped with various space geodesy systems: very long baseline interferometry (VLBI), satellite laser ranging (SLR), Global Positioning System (GPS), and Doppler Orbitography Radiopositioning Integrated by Satellite (DORIS) (Altamimi et al. 2002). Then, an assignment of precise coordinates and linear velocities at reference epochs is made. These data are used, in conjunction with Eq. (2.17), to estimate statistically the angular velocities of each plate having an observation site. Finally, a best fit alignment with the current plates velocity model NNR-NUVEL-1A is performed, in order to satisfy the condition (2.68) (Altamimi et al. 2003).

We can determine the components of the tensors $\boldsymbol{Q}^i$ using a computational method proposed by Schettino (1999b). Table 2.4 lists the six independent components of these tensors for the set of MORVEL plates shown in Fig. 2.38. This data set can be used to determine the Euler vector of the reference plate through Eq. (2.68). The instantaneous Euler pole of the Pacific plate, determined on the basis of the relative Euler vectors of Table 2.3 and the $Q$ tensor components of Table 2.4, is located at 63.5°S, 114.4°E, and its angular velocity is $\omega = 0.65°$/Myr. The NNR version of MORVEL is listed in Table 2.5, while the corresponding velocity fields are shown in Fig. 2.39.

An estimation of the errors associated with the computation of the tensors $\boldsymbol{Q}^i$ can be performed as follows. First, it is possible to show that the area of each plate, $A_i$, can be calculated decomposing the corresponding spherical polygon into a set of spherical triangles, then using the well-known Girard's formula for calculating the area of each triangle (Schettino 1999b).

From (2.63), we see that these quantities are related to the diagonal components of $\boldsymbol{Q}^i$ by the following expression:

$$Tr\left(\boldsymbol{Q}^i\right) = \sum_j \int_{S_i} \left(1 - x_j^2\right) dS = 2A_i \quad (2.70)$$

Therefore, an estimate of the errors associated with the diagonal components of $\boldsymbol{Q}^i$, which are listed in the last column of Table 2.4, can be obtained by evaluating the expression:

$$\varepsilon_i = \frac{Tr\left(\boldsymbol{Q}^i\right) - 2A_i}{2A_i} \quad (2.71)$$

It is important to note that the velocity fields of the NNR version of MORVEL do not really represent velocities relative to the deep mantle. In fact, the equations associated with the NNR condition (2.68) do not consider the contribution of slab pull forces to the total torque balance, and are based upon the implausible assumption that the drag coefficient is uniform across the Earth's LAB. However, the method described above can be considered as a good starting point for the study of the absolute plate motions. For example, we can improve the model introducing in the torque balance equation the torques associated with the pull exerted by subducting slabs.

Slab pull is a downward-directed force that a sinking slab exerts on the unsubducted lithosphere along a trench line (Forsyth and Uyeda 1975). If $\mathbf{T}_i$ is the small circle representative of a trench line, then this force is everywhere normal to $\mathbf{T}_i$. Therefore, if $d\boldsymbol{l}$ is an infinitesimal vector element tangent to $\mathbf{T}_i$, then the torque exerted on the unsubducted lithosphere is given by:

$$\boldsymbol{N}_i = C_i \int_{\mathbf{T}_i} \boldsymbol{r} \times (d\boldsymbol{l} \times \boldsymbol{r}) \quad (2.72)$$

**Table 2.4** $Q$ tensors and areas of the 25 MORVEL plates

| Plate | A | $Q_{11}$ | $Q_{22}$ | $Q_{33}$ | $Q_{12}$ | $Q_{13}$ | $Q_{23}$ | Diag. Err. |
|---|---|---|---|---|---|---|---|---|
| AMU | 0.130659 | 0.108248 | 0.089481 | 0.063589 | 0.028732 | 0.036320 | −0.051295 | 0.0000 % |
| ANT | 1.434290 | 1.328262 | 1.176115 | 0.364247 | −0.050791 | 0.052812 | 0.080667 | 0.0015 % |
| ARB | 0.120824 | 0.074248 | 0.066810 | 0.100589 | −0.048782 | −0.029553 | −0.031041 | −0.0004 % |
| AUS | 0.935403 | 0.602384 | 0.568115 | 0.700304 | 0.230373 | −0.218401 | 0.241845 | −0.0002 % |
| CAR | 0.103729 | 0.094940 | 0.014300 | 0.098213 | 0.024762 | −0.006107 | 0.020566 | −0.0024 % |
| COC | 0.072230 | 0.071072 | 0.003020 | 0.070372 | −0.005543 | 0.001064 | 0.010141 | 0.0028 % |
| CAP | 0.203647 | 0.196537 | 0.022175 | 0.188580 | −0.021636 | 0.007182 | 0.045603 | −0.0005 % |
| EUR | 1.218422 | 1.017712 | 0.913393 | 0.505738 | −0.041466 | −0.222433 | −0.315605 | 0.0000 % |
| IND | 0.30636 | 0.286350 | 0.042306 | 0.284051 | −0.057048 | −0.013096 | −0.060493 | −0.0021 % |
| JDF | 0.006315 | 0.005162 | 0.004356 | 0.003111 | −0.001501 | 0.001916 | 0.002491 | −0.0079 % |
| LWA | 0.117115 | 0.063149 | 0.081116 | 0.089959 | −0.043343 | 0.036053 | 0.029664 | −0.0026 % |
| MAC | 0.007890 | 0.006131 | 0.007510 | 0.002139 | 0.000812 | −0.003172 | 0.001465 | 0.0000 % |
| NAM | 1.440479 | 1.282025 | 1.008008 | 0.590974 | 0.079145 | 0.026680 | 0.378356 | 0.0017 % |
| NUB | 1.440653 | 0.372568 | 1.301217 | 1.207515 | −0.051346 | −0.005428 | 0.044223 | −0.0002 % |
| NAZ | 0.403564 | 0.391445 | 0.070630 | 0.345043 | −0.014536 | −0.003992 | −0.115869 | −0.0012 % |
| PAC | 2.681816 | 1.204054 | 2.045135 | 2.114430 | −0.400314 | 0.062295 | −0.057354 | −0.0002 % |
| PHB | 0.144484 | 0.081761 | 0.078620 | 0.128588 | 0.062670 | 0.029123 | −0.029347 | 0.0003 % |
| RIV | 0.002486 | 0.002289 | 0.000489 | 0.002193 | −0.000625 | 0.000239 | 0.000763 | −0.0201 % |
| SAM | 1.023883 | 0.624948 | 0.586878 | 0.835938 | 0.344415 | 0.181243 | −0.174029 | −0.0001 % |
| SCO | 0.042001 | 0.036816 | 0.034549 | 0.012637 | 0.005706 | 0.012013 | −0.014486 | 0.0000 % |
| SOM | 0.354795 | 0.221032 | 0.153739 | 0.334814 | −0.154901 | 0.024755 | 0.035861 | −0.0007 % |
| SUR | 0.027055 | 0.018681 | 0.026496 | 0.008933 | 0.001954 | 0.012245 | −0.002957 | 0.0000 % |
| SUN | 0.281465 | 0.232911 | 0.054798 | 0.275220 | 0.093052 | 0.004760 | −0.016178 | −0.0002 % |
| SAN | 0.004543 | 0.003525 | 0.004269 | 0.001292 | 0.000527 | 0.001817 | −0.000940 | 0.0000 % |
| YTP | 0.062249 | 0.051303 | 0.024035 | 0.049159 | 0.019688 | 0.011653 | −0.022080 | −0.0008 % |
| *Earth* | 12.566357 | 8.377553 | 8.377560 | 8.377628 | 0.000004 | −0.000012 | −0.000029 | 0.0001 % |
| *Av.%.error* | −0.0001 % | −0.0003 % | −0.0002 % | 0.0006 % | 0.0000 % | 0.0000 % | 0.0000 % | |

Units are in steradians

where $C_i$ is a constant that is assumed to be independent from the subduction velocity, and the line integral is calculated following a counterclockwise path.

If we expand the triple vector product in (2.72), we obtain the following simple expression for the torque:

$$\boldsymbol{N}_i = C_i \int_{\mathbf{T}_i} d\boldsymbol{l} = C_i \left( \boldsymbol{r}_f - \boldsymbol{r}_i \right) \tag{2.73}$$

In this expression, $\boldsymbol{r}_i$ and $\boldsymbol{r}_f$ are, respectively, the position vectors of the start and end points of the trench line $\mathbf{T}_i$. Therefore, we see that the torque exerted on a subducting plate by the attached slab only depends from the width of the subduction zone, not by its curvature. If we introduce the torques (2.73) in the total torque balance equation, we obtain a more realistic equation, which potentially can be solved to determine the absolute Euler vector of the reference plate:

$$\left( \sum_i D_i \boldsymbol{Q}^i \right) \boldsymbol{\omega}_r = \sum_j C_j \left( \boldsymbol{r}_f^j - \boldsymbol{r}_i^j \right) - \sum_i D_i \boldsymbol{Q}^i \boldsymbol{\omega}_{ir} \tag{2.74}$$

This is a system of three equations in the unknown components of $\boldsymbol{\omega}_r$, which can be solved if the drag coefficients $D_i$ and the constants $C_j$ are known. In this instance, the lithosphere always has a non-zero angular momentum, even when $D_i$=$D$ for all plates.

**Table 2.5** The NNR−MORVEL velocity model

| Plate | $\lambda_e$ | $\phi_e$ | $\omega$ | $\omega_1$ | $\omega_2$ | $\omega_3$ |
|---|---|---|---|---|---|---|
| AMU | 63.4 | 237.5 | 0.298 | −0.001248 | −0.001962 | 0.004645 |
| ANT | 65.7 | 242.4 | 0.250 | −0.000829 | −0.001589 | 0.003976 |
| ARB | 48.8 | 351.7 | 0.561 | 0.006374 | −0.000933 | 0.007363 |
| AUS | 33.9 | 37.9 | 0.634 | 0.007241 | 0.005636 | 0.006170 |
| CAR | 35.6 | 267.6 | 0.286 | −0.000168 | −0.004062 | 0.002908 |
| COC | 27.0 | 235.7 | 1.197 | −0.010487 | −0.015371 | 0.009493 |
| CAP | 44.3 | 23.1 | 0.610 | 0.007008 | 0.002985 | 0.007445 |
| EUR | 49.3 | 253.8 | 0.223 | −0.000708 | −0.002435 | 0.002949 |
| IND | 50.4 | 356.9 | 0.545 | 0.006064 | −0.000333 | 0.007329 |
| JDF | −38.2 | 60.0 | 0.951 | 0.006529 | 0.011291 | −0.010270 |
| LWA | 51.9 | 291.0 | 0.286 | 0.001101 | −0.002876 | 0.003932 |
| MAC | 49.2 | 371.1 | 1.145 | 0.012831 | 0.002508 | 0.015120 |
| NAM | −4.6 | 279.7 | 0.208 | 0.000612 | −0.003564 | −0.000292 |
| NUB | 47.9 | 291.9 | 0.293 | 0.001277 | −0.003175 | 0.003788 |
| NAZ | 46.4 | 259.0 | 0.695 | −0.001597 | −0.008213 | 0.008791 |
| PAC | −63.5 | 114.4 | 0.650 | −0.002090 | 0.004605 | −0.010156 |
| PHB | −45.9 | 328.7 | 0.909 | 0.009435 | −0.005735 | −0.011401 |
| RIV | 20.3 | 252.7 | 4.535 | −0.022040 | −0.070903 | 0.027431 |
| SAM | −22.2 | 247.8 | 0.107 | −0.000656 | −0.001604 | −0.000707 |
| SCO | 23.0 | 254.5 | 0.146 | −0.000630 | −0.002263 | 0.000995 |
| SOM | 50.2 | 275.9 | 0.339 | 0.000391 | −0.003767 | 0.004551 |
| SUR | −32.3 | 249.2 | 0.106 | −0.000555 | −0.001459 | −0.000986 |
| SUN | 50.2 | 265.2 | 0.337 | −0.000313 | −0.003750 | 0.004522 |
| SAN | −29.9 | 323.2 | 1.361 | 0.016481 | −0.012351 | −0.011826 |
| YTP | 63.4 | 243.6 | 0.334 | −0.001163 | −0.002339 | 0.005218 |

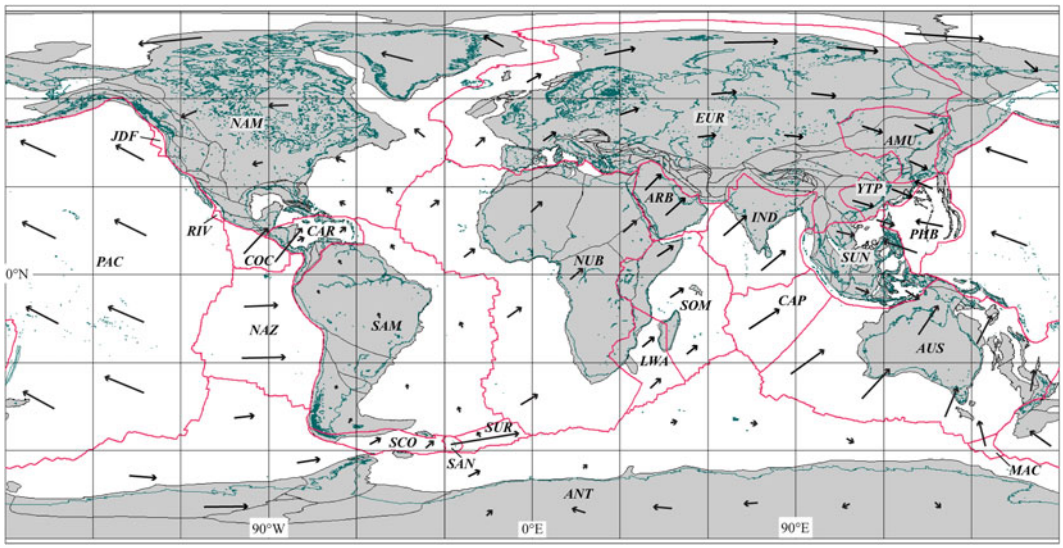


**Fig. 2.39** The "absolute" plate velocity model NNR−MORVEL (DeMets et al. 2010). The *length of the arrows* indicates 20 times the relative displacement of a plate with respect to an adjacent plate

## Problems

1. An Eulerian reference frame is a geocentric reference frame obtained rotating an Euler pole to the North pole. Determine the equation of transformation from geographic to Eulerian latitude;
2. The number of edges in a circuit with $p$ plates is always $e = p-1$. Explain why;
3. Show that the relation $e = p-1$ is compatible with (2.34), $e$ and $p$ being the number of edges and the number of plates in a circuit;
4. Given the three-plates system formed by the Pacific, North American, and Juan de Fuca plates, determine the relative velocity vector of Juan de Fuca with respect to N. America at (46.5°N, 125.8°W) using the data in Table 2.5;
5. Assuming that the spreading asymmetry is zero along the Juan de Fuca Ridge, how long time is required for a point at (46.9°N, 129.4°W) along the ridge to enter the Cascadia Trench and what is the predicted location of ridge subduction?
6. Subduction of the Capricorn plate beneath Sundaland along the Sumatra Trench is highly oblique. Strike-slip motion along the Sumatran Fault, which is parallel to the trench in the forearc region, determines partitioning of such oblique subduction into a trench-normal component and a trench-parallel component. Determine the slip rate and the sense of shear along the Sumatran Fault at (2.5°S, 101.5°E);
7. The Periadriatic Line in northern Italy and Croatia is a wide E–W and NW–SE structure that accommodated strike-slip motion between Africa and Europe in the geologic past (see figure). What would be the style of this fault at (46.4°N, 11°E) and (42.8°N, 17.8°E) if it were a present day plate boundary?

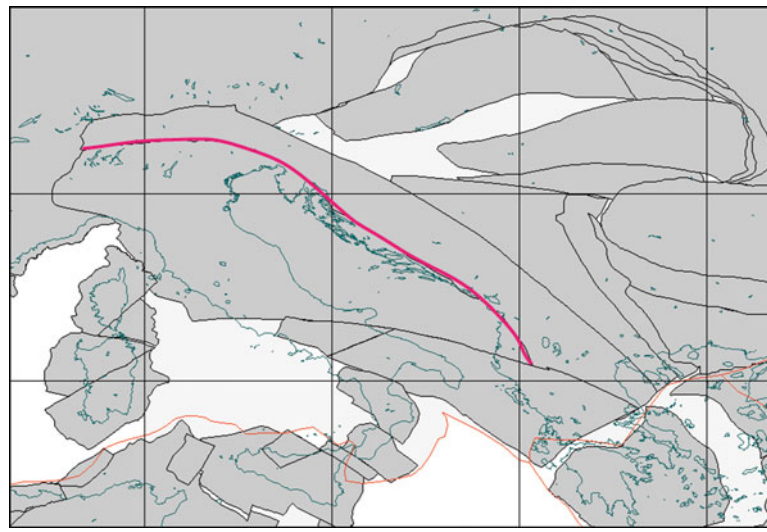

8. Anatolia is a small microplate between Arabia and Europe in the eastern Mediterranean, whose N and SE boundaries are transcurrent faults (see figure). Starting from the relative velocity of Arabia with respect to Europe, calculate the westward escape velocity of this microplate along its strike-slip boundaries;

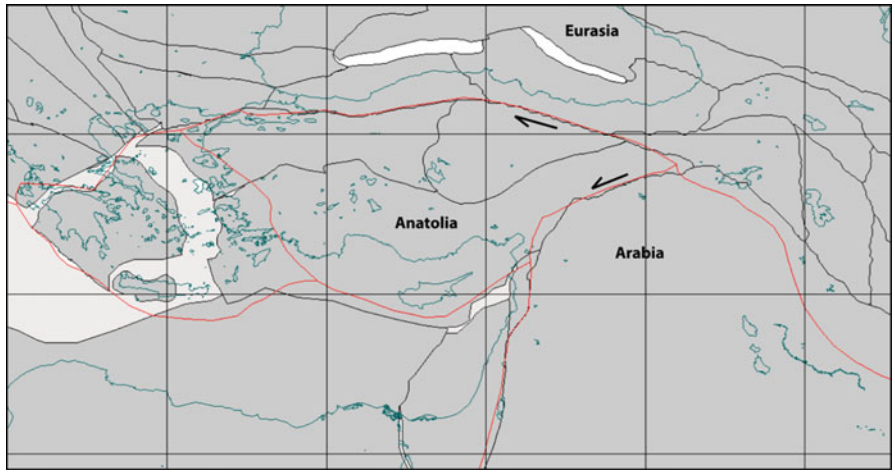


9. Determine the evolution of the Pacific-N. America-J. de Fuca triple junction in the Pacific reference frame, and describe the geological setting around the region where the corresponding plate boundaries meet;
10. Determine the time interval of stability of the triple junction between Nazca, Antarctica, and S. America, and the subsequent migration path;

## References

Altamimi Z, Sillard P, Boucher C (2002) ITRF2000: a new release of the international terrestrial reference frame for earth science applications. J Geophys Res 107(B10):2214. doi:10.1029/2001JB000561

Altamimi Z, Sillard P, Boucher C (2003) The impact of a no-net-rotation condition on ITRF2000. Geophys Res Lett 30(2):1064. doi:10.1029/2002GL016279

Anderson-Fontana S, Engeln JF, Lundgren P, Larson RL, Stein S (1986) Tectonics and evolution of the Juan Fernandez microplate at the Pacific-Nazca-Antarctic triple junction. J Geophys Res 91(B2):2005–2018. doi:10.1029/JB091iB02p02005

Argus DF, Gordon RG (1991) No-net-rotation model of current plate velocities incorporating plate motion model NUVEL-1. Geophys Res Lett 18(11):2039–2042

Beck ME Jr (1986) Model for late Mesozoic-early Tertiary tectonics of coastal California and western Mexico and speculations on the origin of the San Andreas Fault. Tectonics 5(1):49–64. doi:10.1029/TC005i001p00049

Besse J, Courtillot V (1988) Paleogeographic maps of the continents bordering the Indian Ocean since the early Jurassic. J Geophys Res 93(B10):11,791–11,808

Bird P (2003) An updated digital model of plate boundaries. Geochem Geophys Geosyst 4(3):1027. doi:10.1029/2001GC000252

Briais A, Patriat P, Tapponnier P (1993) Updated interpretation of magnetic anomalies and seafloor spreading stages in the South China Sea: implications for the Tertiary tectonics of Southeast Asia. J Geophys Res 98(B4):6299–6328

Brun J-P (1999) Narrow rifts versus wide rifts: inferences for the mechanics of rifting from laboratory experiments. Philos Trans R Soc Lond 357:695–712

Buck WR (1991) Modes of continental lithospheric extension. J Geophys Res 96(B12):20161–20178. doi:10.1029/91JB01485

Bullard EC, Everett JE, Smith AG (1965) The fit of the continents around the Atlantic: a symposium on continental drift. Philos Trans R Soc Lond A 258(1088):41–51

Butler RWH, Spencer S, Griffiths HM (1997) Transcurrent fault activity on the Dead Sea Transform in Lebanon and its implications for plate tectonics and seismic hazard. J Geol Soc 154:757–760. doi:10.1144/gsjgs.154.5.0757

Campbell WH (2003) Introduction to geomagnetic fields, 2nd edn. Cambridge University Press, Cambridge, UK, 337 pp

Cande SC, Stegman DR (2011) Indian and African plate motions driven by the push force of the Réunion plume head. Nature 475:47–52. doi:10.1038/nature10174

Chase CG (1978) Plate kinematics: the Americas, East Africa, and the rest of the world. Earth Planet Sci Lett 37:355–368

Coffin MF, Rabinowitz PD (1987) Reconstruction of Madagascar and Africa: evidence from the Davie Fracture Zone and Western Somali Basin. J Geophys Res 92(B9):9385–9406. doi:10.1029/JB092iB09p09385

Contrucci I, Klingelhöfer F, Perrot J, Bartolome R, Gutscher MA, Sahabi M, Malod J, Rehault J-P (2004) The crustal structure of the NW-Moroccan continental

margin from wide-angle and reflection seismic data. Geophys J Int 159:117–128
Corti G, Bonini M, Conticelli S, Innocenti F, Manetti P, Sokoutis D (2003) Analogue modelling of continental extension: a review focused on the relations between the patterns of deformation and the presence of magma. Earth Sci Rev 63:169–247. doi:10.1016/S0012-8252(03)00035-7
Cox A, Hart RB (1986) Plate tectonics: how it works. Blackwell Scientific Publications, Palo Alto, 392 pp
Dalziel IWD (1981) Back-arc extension in the southern Andes: a review and critical reappraisal. Philos Trans R Soc Lond A 300(1454):319–335
DeMets C, Gordon RG, Argus DF, Stein S (1990) Current plate motions. Geophys J Int 101:425–478
DeMets C, Gordon RG, Argus DF, Stein S (1994) Effect of recent revisions to the geomagnetic reversal timescale. Geophys Res Lett 21:2191–2194
DeMets C, Gordon RG, Argus DF (2010) Geologically current plate motions. Geophys J Int 181:1–80. doi:10.1111/j.1365-246X.2009.04491.x
Dewey JF (1975) Finite plate implications: some implications for the evolution of rock masses at plate margins. Am J Sci 275-A:260–284
Dewey JF, Helman ML, Turco E, Hutton DHW, Knott SD (1989) Kinematics of the Western Mediterranean. In: Coward MP, Dietrich D, Park RG (eds) Alpine tectonics. Geol Soc Spec Publ 45, London, pp 265–283
Fairhead JD (1988) Mesozoic plate tectonic reconstructions of the central South Atlantic Ocean: the role of the West and Central African rift system. Tectonophysics 155(1–4):181–191. doi:10.1016/0040-1951(88)90265-X
Forsyth D, Uyeda S (1975) On the relative importance of the driving forces of plate motion. Geophys J Int 43(1):163–200. doi:10.1111/j.1365-246X.1975.tb00631.x
Fournier M, Patriat P, Leroy S (2001) Reappraisal of the Arabia−India−Somalia triple junction kinematics. Earth Planet Sci Lett 189:103–114
Frank FC (1968) Curvature of island arcs. Nature 220:363
Frisch W, Meschede M, Blakey R (2011) Plate tectonics. Springer, Berlin, 212 pp
Gaina C, Müller DR, Royer J-Y, Stock J, Hardebeck J, Symonds P (1998) The tectonic history of the Tasman Sea: a puzzle with 13 pieces. J Geophys Res 103(B6):12413–12433. doi:10.1029/98JB00386
Gaina C, Gernigon L, Ball P (2009) Palaeocene–recent plate boundaries in the NE Atlantic and the formation of the Jan Mayen microcontinent. J Geol Soc Lond 166:601–616. doi:10.1144/0016-76492008-112
Garfunkel Z (1981) Internal structure of the Dead Sea leaky transform (rift) in relation to plate kinematics. Tectonophysics 80(1–4):81–108. doi:10.1016/0040-1951(81)90143-8
Gould R (1988) Graph theory. Benjamin, Menlo Park, 332 pp
Hamilton WB (1987) Crustal extension in the basin and Range Province, southwestern United States. In: Coward MP, Dewey JF, Hancock PL (eds) Continental extensional tectonics, GSA Spec. Publ., 28 pp 155–176
Hamilton WB (2002) The closed upper–mantle circulation of plate tectonics. In: Stein S, Freymueller JT (eds) Plate boundary zones, vol 30, Geodynamics series. AGU, Washington, DC, pp 359–410. doi:10.1029/GD030p0359
Hey RN (1977) A new class of pseudofaults and their bearing on plate tectonics: a propagating rift model. Earth Planet Sci Lett 37:321–325
Hey RN, Menard HW, Atwater TM, Caress DW (1988) Changes in direction of seafloor spreading revisited. J Geophys Res 93(B4):2803–2811
Jarrard RD (1986) Relations among subduction parameters. Rev Geophys 24:217–284
Jestin F, Huchon P, Gaulier JM (1994) The Somalia plate and the East African rift system: present-day kinematics. Geophys J Int 116(3):637–654. doi:10.1111/j.1365-246X.1994.tb03286.x
Jung W-Y, Vogt PR (1997) A gravity and magnetic anomaly study of the extinct Aegir Ridge, Norwegian Sea. J Geophys Res 102(B3):5065–5089
Kleinrock MC, Phipps Morgan J (1988) Triple junction reorganization. J Geophys Res 93(B4):2981–2996. doi:10.1029/JB093iB04p02981
Korhonen JV et al (2007) Magnetic anomaly map of the world (and associated DVD), Scale: 1:50,000,000, 1st edn. Commission for the Geological Map of the World, Paris
Kreemer C, Holt WE, Haines AJ (2003) An integrated global model of present-day plate motions and plate boundary deformation. Geophys J Int 154:8–34
Laville E, Piqué A (1991) La Distension crustale atlantique et atlasique au Maroc au debut du Mesozoique; le rejeu des structures hercyniennes. Bull Soc Géol Fr 162(6):1161–1171
Lebrun J-F, Lamarche G, Collot J-Y (2003) Subduction initiation at a strike-slip plate boundary: the Cenozoic Pacific-Australian plate boundary, south of New Zealand. J Geophys Res 108:2453. doi:10.1029/2002JB002041
Lonsdale P (1988) Structural pattern of the Galapagos microplate and evolution of the Galapagos triple junctions. J Geophys Res 93(B11):13551–13574. doi:10.1029/JB093iB11p13551
McCaffrey R (1992) Oblique plate convergence, slip vectors, and forearc deformation. J Geophys Res 97:8905–8915
McKenzie D (1976) The East Anatolian Fault: a major structure in Eastern Turkey. Earth Planet Sci Lett 29(1):189–193. doi:10.1016/0012-821X(76)90038-8
McKenzie D (1978) Some remarks on the development of sedimentary basins. Earth Planet Sci Lett 40(1):25–32. doi:10.1016/0012-821X(78)90071-7
McKenzie D, Morgan WJ (1969) Evolution of triple junctions. Nature 224:125–133
Menard HW, Atwater TM (1968) Changes in direction of sea floor spreading. Nature 219:463–467

Minster JB, Jordan TH (1978) Present-day plate motions. J Geophys Res 83:5331–5354

Müller RD, Royer J-Y, Lawver LA (1993) Revised plate motions relative to the hotspots from combined Atlantic and Indian Ocean hotspot tracks. Geology 21:275–278

Müller RD, Roest WR, Royer J-Y, Gahagan LM, Sclater JG (1997) Digital isochrons of the world's ocean floor. J Geophys Res 102(B2):3211–3214

Patriat P, Courtillot V (1984) On the stability of triple junctions and its relation to episodicity in spreading. Tectonics 3(3):317–332. doi:10.1029/TC003i003p00317

Pindell JL, Cande SC, Pitman WC III, Rowley DB, Dewey JF, Labrecque J, Haxby W (1988) A plate-kinematic framework for models of Caribbean evolution. Tectonophysics 155:121–138

Ramos VA, Cristallini EO, Pérez DJ (2002) The Pampean flat-slab of the Central Andes. J S Am Earth Sci 15(1):59–78. doi:10.1016/S0895-9811(02)00006-8

Roest WR, Srivastava SP (1989) Sea-floor spreading in the Labrador Sea: a new reconstruction. Geology 17: 1000–1003

Ross MI, Scotese CR (1988) A hierarchical tectonic model of the Gulf of Mexico and Caribbean region. Tectonophysics 155(1–4):139–168

Rowley DB, Lottes AL (1988) Plate-kinematic reconstructions of the North Atlantic and Arctic: late Jurassic to present. Tectonophysics 155(1–4):73–120

Sandwell DT, Smith WHF (1997) Marine gravity anomaly from Geosat and ERS 1 satellite altimetry. J Geophys Res 102:10039–10054

Schettino A (1998) Computer aided paleogeographic reconstructions. Comput Geosci 24(3):259–267

Schettino A (1999a) Polygon intersections in spherical topology: application to plate tectonics. Comput Geosci 25(1):61–69

Schettino A (1999b) Computational methods for calculating geometric parameters of tectonic plates. Comput Geosci 25(8):897–907

Schettino A, Scotese CR (2002) Global kinematic constraints to the tectonic history of the Mediterranean region and surrounding areas during the Jurassic and Cretaceous. In: Rosenbaum G, Lister GS (eds) Reconstruction of the evolution of the Alpine-Himalayan orogen. J Virtual Explor 7:147–166

Schettino A, Scotese CR (2005) Apparent polar wander paths for the major continents (200 Ma – present day): a paleomagnetic reference frame for global plate tectonic reconstructions. Geophys J Int 163(2):727–759

Schettino A, Tassi L (2012) Trench curvature and deformation of the subducting lithosphere. Geophys J Int 188(1):18–34. doi:10.1111/j.1365-246X.2011.05262.x

Schettino A, Turco E (2006) Plate kinematics of the Western Mediterranean region during the Oligocene and early Miocene. Geophys J Int 166(3): 1398–1423

Schettino A, Turco E (2009) Breakup of Pangaea and plate kinematics of the central Atlantic and Atlas regions. Geophys J Int 110:1078–1097

Schettino A, Turco E (2011) Tectonic history of the western Tethys since the late Triassic. GSA Bull 123(1/2):89–105. doi:10.1130/B30064.1

Schlich R (1974) Sea floor spreading history and deep sea drilling results in the Madagascar and Mascarene Basins, Western Indian Ocean. In: Simpson ESW, Schlich R, et al. (eds) Initial reports of the deep sea drilling project, 25, US Govt. Printing Office, Washington, pp 663–678

Schmid SM, Kissling E (2000) The arc of the western Alps in the light of geophysical data on deep crustal structure. Tectonics 19(1):62–85

Schmid SM, Pfiffner OA, Froitzheim N, Schönborn G, Kissling E (1996) Geophysical-geological transect and tectonic evolution of the Swiss-Italian Alps. Tectonics 15(5):1036–1064

Sengör AMC (1979) The North Anatolian transform fault: its age, offset and tectonic significance. J Geol Soc 136:269–282. doi:10.1144/gsjgs.136.3.0269

Shaw PR (1987) Investigations of relative plate motions in the South Atlantic using SEASAT altimeter data. J Geophys Res 92(B9): 9363–9375

Smythe DK (1989) Rockall Trough-Cretaceous or late Palaeozoic? Scott J Geol 25(1):5–43

Solomon SC, Sleep NH (1974) Some simple physical models for absolute plate motions. J Geophys Res 79(17):2557–2567. doi:10.1029/JB079i017p02557

Solomon SC, Sleep NH, Jurdy DM (1977) Mechanical models for absolute plate motions in the early Tertiary. J Geophys Res 82(2):203–212. doi:10.1029/JB082i002p00203

Treves B (1984) Orogenic belts as accretionary prisms: the example of the northern Apennines. Ofioliti 9: 577–618

Vigny C, Socquet A, Rangin C, Chamot-Rooke N, Pubellier M, Bouin M-N, Bertrand G, Becker M (2003) Present-day crustal deformation around Sagaing fault, Myanmar. J Geophys Res 108:2533. doi:10.1029/2002JB001999,B11

Wernicke B (1985) Uniform-sense normal simple shear of the continental lithosphere. Can J Earth Sci 22: 108–125

Whittaker JM, Müller RD, Roest WR, Wessel P, Smith WHF (2008) How supercontinents and superoceans affect seafloor roughness. Nature 456:938–941. doi:10.1038/nature07573

http://www.springer.com/978-3-319-09134-1

Quantitative Plate Tectonics
Physics of the Earth - Plate Kinematics – Geodynamics
Schettino, A.
2015, XIV, 403 p. 284 illus., 119 illus. in color. With online files/update., Hardcover
ISBN: 978-3-319-09134-1